CRANFIELD UNIVERSITY

FRANCESC FÀBREGAS FLAVIÀ

# NUMERICAL PREDICTIONS OF THE HYDRODYNAMIC DRAG OF THE PLAT-O TIDAL ENERGY CONVERTER AND COMPARISON WITH MEASUREMENTS IN A WATER CHANNEL

SCHOOL OF ENGINEERING
Renewable Energy Engineering

MSc THESIS
Academic year: 2012 - 2013

Supervisor: Dr. Florent Trarieux
August 2013

CRANFIELD UNIVERSITY

SCHOOL OF ENGINEERING
Renewable Energy Engineering

MSc THESIS

Academic Year 2012 - 2013

FRANCESC FÀBREGAS FLAVIÀ

# Numerical predictions of the hydrodynamic drag of the PLAT-O tidal energy converter and comparison with measurements in a water channel

Supervisor: Dr. Florent Trarieux
August 2013

This thesis is submitted in partial fulfilment of the requirements for the degree of Master of Science

# ABSTRACT

Tidal energy industry is currently involved in a strong growth phase and it is expected to play an important role as far as meeting the renewable energy targets is concerned.

The product development strategy adopted by tidal energy companies is nowadays broadly based on a gradual increase of the prototypes scaling factor. Thus, the prediction of important engineering quantities such as drag at intermediate stages becomes of vital importance for developers.

The diversity and complexity of the geometries adopted by second-generation tidal energy converters preclude the use of already existing drag scaling methods conceived for specific applications such as ship design. In this context, numerical simulations are regarded as a suitable alternative.

This study addresses the use of Computational Fluid Dynamics (CFD) to determine the drag of the unique tidal energy converter developed by *Sustainable Marine Energy (SME)* called PLAT-O.

Several preliminary simulations were performed on the isolated PLAT-O components. The results were compared with previous CFD studies devoted to similar form bodies and good agreement was found.

Following this stage, the drag predictions on the whole PLAT-O device were undertaken and compared to existing experimental data. Significant differences between them were observed.

This work has demonstrated that a RANS flow solver is not an efficient tool to predict the resistance of a small-scale PLAT-O device. In addition, this study has predicted that CFD will be suitable to assess the design of larger-scale prototypes.

Keywords:

CFD, Star CCM+, RANS, Standard k-ε, SST k-ω, Towing Tank Testing

# ACKNOWLEDGEMENTS

I would like to specially thank Sustainable Marine Energy (SME), particularly Jason Hayman, for providing the invaluable opportunity to be involved in the design of their unique tidal energy converter PLAT-O concept, as well as for the great amount of knowledge transferred which has turned this work into a very enriching experience.

I gratefully acknowledge my academic supervisor Dr. Florent Trarieux for proposing the challenging and interesting topic of the thesis and for his confidence in me to tackle it. In addition, I thank him for his guidance and support during the whole project.

I would like to thank Dr. Joao Amaral Teixeira and Dr. Andrew Shires for devoting part of their hectic time to orientate my work and to solve some doubts arisen from the use of Computational Fluid Dynamics software.

Special thanks to Maxime Dumont for his valuable help on CAD design and for providing all the geometries required to perform this study. Moreover, I thank him for his useful recommendations on important aspects of the thesis.

I would like to thank Fabrizio Fiore and Romain Fabre for their clarifications about the available experimental data and for their interest in the outcomes of this work.

I gratefully acknowledge Daniel Kosiński for providing very useful advice and literature related to several aspects of Computational Fluid Dynamics.

I would like to thank Simon Varghese for his help with the use of graph digitizer software.

Thanks to Star CCM+ technical support for providing immediate resolution to my questions.

Last but not least I would like to express the biggest gratitude to all my friends and family who have provided support at any time.

# TABLE OF CONTENTS

# LIST OF FIGURES

## LIST OF TABLES

# LIST OF EQUATIONS

# LIST OF ABBREVIATIONS

| | |
|---|---|
| SME | Sustainable Marine Energy |
| RANS | Reynolds-Averaged Navier-Stokes |
| LES | Large Eddy Simulation |
| DNS | Direct Numerical Simulation |
| DES | Detached Eddy Simulation |
| Ifremer | French Research Institute for Exploitation of the Sea |
| ITTC | International Towing Tank Conference |
| CFD | Computational Fluid Dynamics |
| SMC | Second Moment Closure |
| RSTM | Reynolds Stress Transport Model |
| TI | Turbulence Intensity |
| SIMPLE | Semi-Implicit Method for Pressure Linked Equations |
| SIMPLER | SIMPLE Revised |
| SIMPLEC | SIMPLE Consistent |
| PISO | Pressure Implicit with Splitting of Operators |
| S-A | Spalart and Allmaras turbulence model |
| SST | Shear Stress Transport |
| AUV | Autonomous Underwater Vehicle |
| CAD | Computer-aided design |
| PLAT-O | Platform Ocean |
| DNV-RP | Det Norske Veritas – Recommended Practices |
| 2D/3D | Two-dimensional/Three-dimensional |
| VIV | Vortex Induced Vibrations |
| N | Newton |
| K | Von Kármán constant |
| B | Wall roughness constant |
| $\nu$ | Kinematic viscosity |
| $\delta$ | Wall boundary layer thickness |
| $V$ | Largest eddies velocity scale |
| $L$ | Largest eddies length scale |
| $C_D$ | Total drag coefficient |
| $C_F$ | Skin friction drag coefficient |

| | |
|---|---|
| $\tau$ | Shear stress |
| $\tau_w$ | Wall shear stress |
| $\mu$ | Viscosity of the fluid |
| $\mu_T$ | Eddy or turbulent viscosity |
| $u$ | Velocity in the principal direction of the flow |
| $u_\tau$ | Wall friction velocity |
| $y$ | Distance from the wall |
| $y+$ | Non-dimensional form of y |
| $y^*$ | Alternative y+ definition |
| $u+$ | Non-dimensional form of u |
| $u'$ | Fluctuating velocity |
| $\bar{u}$ | Mean velocity |
| $F$ | Force |
| $f$ | Frequency |
| $\rho$ | Density of the fluid |
| $S$ | Reference area |
| $g$ | Gravity acceleration |
| $p$ | Pressure |
| $Re$ | Reynolds number |
| $t$ | Time |
| $T$ | Temperature |
| $k$ | Turbulent kinetic energy |
| $\varepsilon$ | Rate of transfer of k |
| $\omega$ | Frequency of the largest eddies |
| $\hat{u}$ | Internal energy of the fluid |
| $U$ | Free-stream velocity |
| $\emptyset$ | Viscous-dissipation function |
| $St$ | Strouhal number |
| $C_p$ | Pressure coefficient |

# 1 INTRODUCTION

Wind is nowadays a mature renewable energy technology. Many years of experience have led to a unification of the design configurations until the well-known and broadly used three bladed horizontal axis wind turbine. Contrarily, tidal energy converters have adopted multiple configurations so far and no specific trend toward a standardized design has yet been appreciated.

In comparison with wind streams, tidal currents present some important advantages such as having a higher energy density and being more easily predictable and, therefore, reliable. Moreover, tidal energy is expected to play an important role as far as meeting the renewable energy targets is concerned. In spite of these facts, the technology potential has not been fully developed yet. Many different companies have proposed their own tidal energy converter concepts and are involved in the process of proving their effectiveness.

The product development strategy of tidal energy industry is nowadays broadly based on a gradual increase of the prototypes scaling factor. In its early life, development strategies were mainly focused on pilot demonstration with high associated costs at early stages. Based on years of experience, device testing at small scale has been proven to be a better and more useful method to understand the key features of performance and identify early design mistakes at low cost and with minimum loss of time.

In the framework of such a strategy, the accurate prediction of key physical design parameters such as drag at intermediate stages in the scaling up process becomes of special importance. It enables to reduce the level of uncertainty with respect to the loads acting on the structure and facilitates the development of larger scale prototypes.

The available methods to predict the drag of bodies subjected to marine environment have been developed for very specific applications such as ship design and they cannot be applied to the different complex geometry configurations adopted by tidal energy converters. Hence, numerical CFD simulations calibrated with experimental data are regarded as a suitable alternative.

This study arises from the necessity of *Sustainable Marine Energy LTD* to obtain a reliable method of calculating the drag of a 1:5 scale PLAT-O prototype which is expected to be deployed at sea in September 2013. The main aim is to analyse whether CFD is suitable to calculate the total resistance of the unique tidal energy converter designed by SME. Moreover, an additional expected outcome is the improvement of the existing knowledge about important features of the flow around the several components of the 1:12 scale prototype already built.

In order to achieve the purposes mentioned above, the study has been developed in the following manner.

In the first work stage, a thorough review of the CFD theory and recommended practices has been performed. In addition, previous CFD studies on bodies similar to the different PLAT-O components have been analysed. Specifically, the focus has been on AUV's (Autonomous Underwater Vehicles) and circular cylinders.

In the second stage, CFD simulations on both the PLAT-O 1:12 scale prototype pontoons and circular cylinders have been undertaken. The calculations have been compared to the results of the studies analysed in the previous stage. Moreover, experimental drag data has been obtained from towing tank tests on one of the PLAT-O prototype pontoons at the Cranfield University Ocean Systems Test Laboratory. The knowledge acquired from this stage has been valuable to tackle the last step of the project.

In the final stage, the drag of the PLAT-O 1:12 scale prototype has been obtained from CFD simulations and the results have been compared with existing experimental data from previous testing campaigns.

The general structure of the thesis reflects the workflow explained above.

# 2 LITERATURE REVIEW

## 2.1 Drag

Drag can be defined as “the component of any fluid-dynamic force, the direction of which coincides with that of the undisturbed flow” (Hoerner, 1965, p.7). With respect to terminology, *drag* has been traditionally used in aviation whereas *resistance* has been employed in marine engineering. In the present study both terms will be used indistinctly.

The total resistance force acting on a body immersed in a fluid can be separated into different contributions. Some of them, such as shock waves or ocean waves resistance, are specific of particular engineering applications. Contrarily, both the pressure and friction drag are present in all kind of flows.

Because of the viscosity of the fluid, a velocity gradient known as boundary layer is formed between the surface of the body and the outer flow. It generates shear stresses which, once integrated over the whole wetted area, constitute the friction drag. The mathematical expression of the shear stresses for a Newtonian fluid is:

$$\tau = \mu \cdot \frac{\partial u}{\partial y} \qquad \textbf{(2-1)}$$

*where* $\mu$ *is the dynamic viscosity of the fluid,* $u$ *is the velocity in the principal direction of the flow, y the cross-stream co-ordinate and* $\tau$ *is the viscous stress.*

In comparison with laminar boundary layers, the turbulent are characterized by having higher velocity gradients. Therefore, from equation (2-1) it can be derived that they will generate higher shear stresses.

The flow is not generally capable of remaining attached to an arbitrary body shape through its whole length. Instead, it separates at some point and generates a region of low pressures called wake. “The difference between the high pressure in the front stagnation point region and the low pressure in the rear separated region causes a large drag contribution called pressure drag” (White, 2003, p. 478).

Usually the drag forces are expressed as a non-dimensional coefficient:

$$C_D = \frac{F}{\frac{1}{2} \cdot \rho \cdot S \cdot v^2} \tag{2-2}$$

*where $F$ is the total drag force, $\rho$ the density of the fluid, $S$ the reference area and $v$ the free-stream velocity.*

Analytical expressions have been derived to model the boundary layer and allow calculating the friction resistance. They fail to represent the separated region of the flow and, therefore, other techniques such as experimental testing or CFD are used to obtain the drag of arbitrary shapes.

Notwithstanding, some empirical formulae are employed in early stages of design to estimate both the friction and the pressure resistance. They are based on flat plate experimental measurements and use form factors to model the effect of the body thickness. One of these methods called ITTC 57 has been explained in Appendix A.

## 2.2 CFD

This section of the literature review has been devoted to the underlying physics, equations and procedures involved in CFD analysis. The aim is to investigate relevant features that are hidden behind the user-friendly Star CCM+ CFD software interface**.**

### 2.2.1 CFD Governing Equations

The final aim of Computational Fluid Dynamics is to provide the values of different variables which characterize the studied flow. From them, valuable engineering quantities such as drag can be derived.

The numerical values of the flow variables such as velocities and pressures are obtained solving the system of governing equations composed by the continuity, the momentum and the energy equations. In the following sections their differential forms will be exposed.

#### 2.2.1.1 Continuity equation

The continuity equation expresses mathematically the conservation of mass. Thus, it is also known as *conservation of mass equation*. It is expressed as:

$$\frac{\partial \rho}{\partial t} + \frac{\partial}{\partial x}(\rho u) + \frac{\partial}{\partial y}(\rho v) + \frac{\partial}{\partial z}(\rho w) = 0 \qquad \textbf{(2-3)}$$

*where ρ, u, v and w are respectively density and velocities in x, y and z directions.*

For the particular case of incompressible flows, where *ρ* is constant, it takes the form:

$$\frac{\partial u}{\partial x} + \frac{\partial v}{\partial y} + \frac{\partial w}{\partial z} = 0 \qquad \textbf{(2-4)}$$

#### 2.2.1.2 Momentum equation

The linear momentum equation can be derived from a balance of momentum applied to a differential control volume and is expressed as:

$$\rho g_x - \frac{\partial p}{\partial x} + \frac{\partial \tau_{xx}}{\partial x} + \frac{\partial \tau_{yx}}{\partial y} + \frac{\partial \tau_{zx}}{\partial z} = \rho \left( \frac{\partial u}{\partial t} + u \frac{\partial u}{\partial x} + v \frac{\partial u}{\partial y} + w \frac{\partial u}{\partial z} \right) \qquad \textbf{(2-5)}$$

$$\rho g_y - \frac{\partial p}{\partial y} + \frac{\partial \tau_{xy}}{\partial x} + \frac{\partial \tau_{yy}}{\partial y} + \frac{\partial \tau_{zy}}{\partial z} = \rho \left( \frac{\partial v}{\partial t} + u \frac{\partial v}{\partial x} + v \frac{\partial v}{\partial y} + w \frac{\partial v}{\partial z} \right) \qquad \textbf{(2-6)}$$

$$\rho g_z - \frac{\partial p}{\partial z} + \frac{\partial \tau_{xz}}{\partial x} + \frac{\partial \tau_{yz}}{\partial y} + \frac{\partial \tau_{zz}}{\partial z} = \rho \left( \frac{\partial w}{\partial t} + u \frac{\partial w}{\partial x} + v \frac{\partial w}{\partial y} + w \frac{\partial w}{\partial z} \right) \qquad \textbf{(2-7)}$$

*where $\tau_{ij}$ are the components of the stress tensor, $g_i$ represents the gravity acceleration constant and $p$ the hydrostatic pressure. The rest of the variables are the same as for the continuity equation.*

The left hand side of the equations is composed of the force terms per unit volume, whereas the right hand side contains the acceleration separated into local and convective components.

The forces acting on a control volume can be separated into body forces and surface forces. The former are generated by external fields such as gravity or magnetism and the latter are due to stresses on sides of the control surface caused by hydrostatic pressure and viscous stresses from the velocity gradients in the flow. In this study the only body force considered will be gravity.

For the particular case of a Newtonian fluid, where the viscous stresses can be expressed as in equation (2-1), the equations above are named *Navier-Stokes equations*. For a constant density and viscosity fluid they adopt the form:

$$\rho g_x - \frac{\partial p}{\partial x} + \mu\left(\frac{\partial^2 u}{\partial x^2} + \frac{\partial^2 u}{\partial y^2} + \frac{\partial^2 u}{\partial z^2}\right) = \rho\frac{du}{dt} \tag{2-8}$$

$$\rho g_y - \frac{\partial p}{\partial y} + \mu\left(\frac{\partial^2 v}{\partial x^2} + \frac{\partial^2 v}{\partial y^2} + \frac{\partial^2 v}{\partial z^2}\right) = \rho\frac{dv}{dt} \tag{2-9}$$

$$\rho g_z - \frac{\partial p}{\partial z} + \mu\left(\frac{\partial^2 w}{\partial x^2} + \frac{\partial^2 w}{\partial y^2} + \frac{\partial^2 w}{\partial z^2}\right) = \rho\frac{dw}{dt} \tag{2-10}$$

*where $\mu$ represents the dynamic viscosity of the fluid. The rest of the variables are as stated above.*

#### 2.2.1.3 Energy equation

The differential energy equation is usually expressed in compact form as:

$$\rho\frac{d\hat{u}}{dt} + p(\nabla \cdot V) = \nabla \cdot (k\nabla T) + \emptyset \tag{2-11}$$

*where $\hat{u}$ is internal energy; $p$ the pressure; $V$ the velocity vector, $k$ the coefficient of thermal conductivity, $T$ the temperature and $\emptyset$ the viscous-dissipation function.*

The flows which will be treated in this study are not affected by thermal interactions and, therefore, the energy equation will not be used.

To summarize, the system of equations to be solved for the cases analysed in this study consists of the continuity (2-4) and momentum (2-8), (2-9), (2-10) equations. Therefore, it is composed of four equations and four unknowns, together with the appropriate boundary conditions. However, as will be seen in section 2.2.5, the number of unknowns will increase when dealing with turbulent flows.

### 2.2.2 Numerical methods

The system of equations mentioned in section 2.2.1 does not have an analytical solution for the majority of practical engineering problems and therefore needs to be solved numerically.

Firstly, it involves transforming the partial differential equations into discrete algebraic equations. They are evaluated at several points of the domain which is discretized by means of a mesh generation process (section 2.2.3). There exist different discretization procedures such as Finite Difference or Finite Element but the most widely used in CFD is the Finite Volume.

Secondly, the discretized equations need to be solved using numerical methods which can be either direct or iterative. The latter have been proved to have lower computational cost than the former for the majority of cases and are usually the default in commercial CFD codes. Star CCM+ incorporates both Jacobi and Gauss-Seidel iterative methods.

Two different strategies can be adopted when solving the governing equations. Either they can be solved sequentially (segregated flow) or simultaneously (coupled flow). The former is mainly used for incompressible flows whereas the latter is recommended for cases with high Mach numbers.

As can be derived from the system of equations mentioned in section 2.2.1, which is valid for incompressible flows, pressure is not explicitly expressed. This involves the use of special schemes. In the majority of finite volume commercial codes, such as Star CCM+, SIMPLE is the default algorithm. SIMPLER, SIMPLEC or PISO represent other alternatives which may be preferred for some specific applications.

The calculated solution at the nodes of the discretized domain using finite volume is interpolated at the faces of the cell by means of appropriate interpolating schemes such as *second-order upwind* or *central difference*. Both of them are available in Star CCM+.

### 2.2.3 Mesh generation

The generation of a good quality grid is of fundamental importance in CFD as it plays a decisive role in the success of convergence, in the computational time required to achieve the solution and in its accuracy.

The focus of this section is on the main characteristics that a good mesh should have and on the tools that Star CCM+ provides to generate it and to assess its quality.

#### 2.2.3.1 Mesh quality

Different CFD guidelines (ERCOFTAC, 2000; Tu et al., 2008) emphasize that the mesh should capture both flow features and geometry accurately. The former is usually achieved by allocating more nodes to the regions of the flow where there exist large variations of the variables. To increase efficiency, the number of cells in areas where there is little action is reduced. The latter is achieved by choosing the appropriate size of elements at the surface of the body.

Apart from its density, there are other factors which influence the quality of the mesh such as the distance from the near wall cells to the boundaries, the shape of the cells and the transition rates from low refined areas to highly refined areas. The near wall distance is of particular importance and will be addressed in detail in section 2.2.5.2.1.

With respect to the shape of the cells, ERCOFTAC (2000) and Tu et al. (2008) recommend avoiding cells with high levels of skewness, large aspect ratios and high warp angles[1]. Moreover, they recommend avoiding non-orthogonal cells near boundaries. Finally, they also recommend controlling the stretching of the mesh to avoid large size differences between contiguous cells.

Star CCM+ provides a tool called *mesh diagnostics* which generates statistics of mesh quality based on several parameters such as cell and boundary skewness

---

[1] The warp angle represents a way to measure how far is a quadrilateral element from being planar.

angles, face validity, cell quality and volume change. They are represented in Figure 2-1. Moreover, the software includes the possibility to remove from the grid cells which fall below a quality metric threshold fixed by the user.

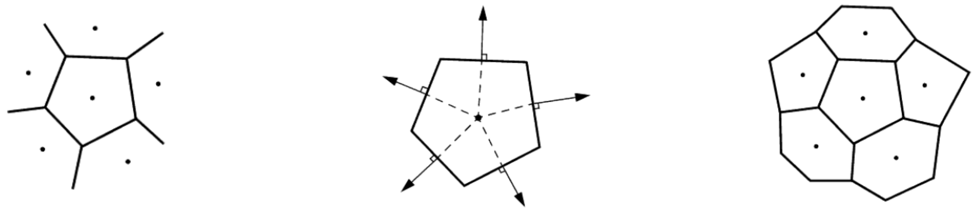

a) Good cell quality b) Good face validity c) Good volume change

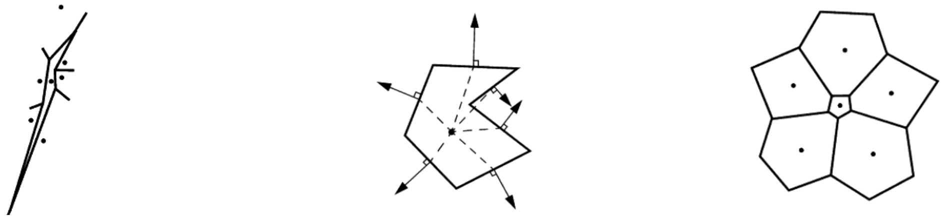

d) Bad cell quality e) Bad face validity f) Bad volume change

**Figure 2-1 – Mesh quality metrics. Source: Star CCM+ user-guide (2013)**

ERCOFTAC (2000) and Tu et al. (2008) also recommend using prismatic or hexahedral cells instead of tetrahedral elements in the boundary layer to avoid convergence problems. Star CCM+ includes the *prism layer* meshing module which enables clustering this type of grid cells near wall boundaries.

### 2.2.3.2 Star CCM+ volume mesh types

The generation of a surface mesh is usually the step previous to obtain a volume three-dimensional mesh in Star CCM+. The modules called *surface remesher* and *surface wrapper* are provided with the aim of improving the final surface mesh quality.

Star CCM+ user-guide (2013) suggests using *surface remesher* if a high level of accuracy in representing the geometry is required, as well as to improve the initial triangulation resolution of the imported surface. It only recommends using surface wrapper when the quality of the imported geometry is very poor.

With regard to the types of volume meshing models, Star CCM+ enables to choose among tetrahedral, polyhedral and trimmed hexahedral cells. It also provides other specific meshing strategies such as advancing layer mesh and thin mesh.

Star CCM+ user-guide (2013) suggests using tetrahedral and polyhedral meshers in complex mesh generation problems, whereas the trimmer mesher is recommended for both simple and complex cases.

In comparison with polyhedral or trimmer models, the tetrahedral is claimed to be the fastest and to use the lowest amount of memory for a given number of cells. However, the polyhedral mesher is deemed to be better space filler. Star CCM+ user-guide (2013) states that the trimmed layer mesher is robust, efficient and that it contains highly desirable mesh attributes. Figure 2-2 shows a comparison of the three methods explained above.

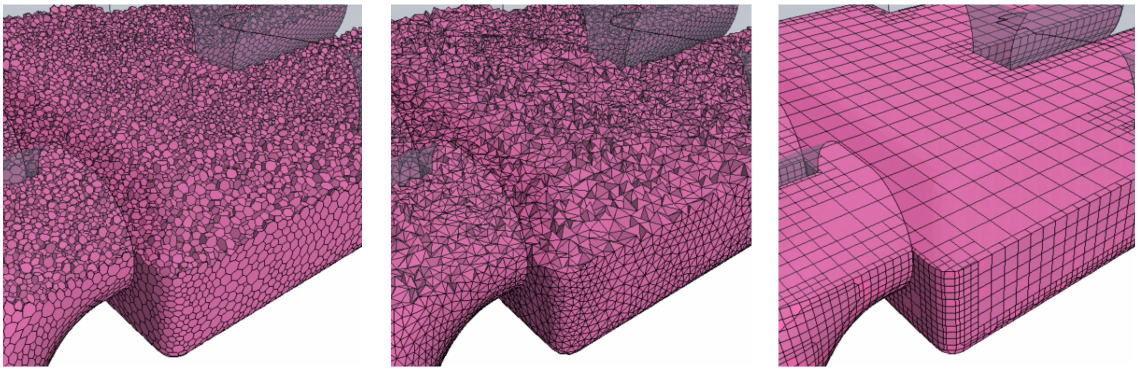

a) Polyhedral cells b) Tetrahedral cells c) Trimmed cells

**Figure 2-2 – Different mesher modules. Source: Star CCM+ user-guide (2013)**

### 2.2.4 Turbulence

The equations of continuity and momentum illustrated in section 2.2.1 are satisfied by both laminar and turbulent flows. The former are characterized by a steady well-organized motion which is encountered at low enough Reynolds numbers. The disturbances arising from the free-stream or induced by other factors such as surface roughness are dissipated by viscosity. Contrarily, the latter occur when the laminar motion becomes unstable because of an increase of the fluid’s inertia versus the viscous forces. In such case the motion becomes three dimensional and unsteady as the disturbances on the flow are not dissipated.

The different characteristics of the flows have an impact on the strategies adopted to solve the equations. The instantaneous fluctuating variables of a turbulent flow cannot be easily handled by mathematics and therefore usually some extra modelling of the variables is needed before being able to solve the system of equations. In contrast, for laminar flow, the equations of motion have “well-behaved steady solutions” (Wilcox, 2006, p. 3) and therefore they can be solved “going right to the attack” (White, 2007, p. 356) without previously having to apply any transformation.

The majority of flows in practical applications are turbulent. Therefore, it is valuable to get a deeper understanding of the phenomenon by analysing its main characteristics.

#### 2.2.4.1 Physical Characterization

Turbulence has been called “the major unsolved problem of classical physics” (Wilcox, 2006, p. 5) or even “the invention of the Devil on the seventh day of creation, when the Good Lord wasn’t looking” (Bradshaw, 1994, quoted in ERCOFTAC, 2000, p. 20). These expressions highlight the complexities involved within the physical phenomenon.

If some flow variables of interest such as velocity or pressure were monitored at a fixed point in a turbulent flow the result of the measurements would be similar to the time history of Figure 2-3.

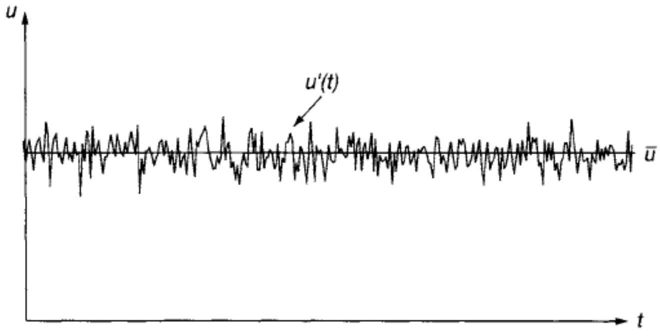

**Figure 2-3 – Turbulent velocity fluctuations. Source: Tu et al. (2008)**

It can be appreciated that some irregular fluctuations ($u'$) of high frequency are superimposed to the mean property of the flow ($\bar{u}$). Even if the magnitude of the perturbations does not exceed a certain percentage of the mean value, they cannot be omitted as they have an important effect on the fluid motion. For instance, from an engineering point of view, the mixing motion of the fluid which boosts the transfer of mass, momentum and energy between adjacent layers of the flow is of paramount importance.

Based on experiments, turbulence has been generally described using the term *eddying motion* which refers to the swirling and rotational three-dimensional structures observed called vortex or eddies. These flow structures travel superimposed on the main flow and their length and velocity scales span from the order of magnitude of the mean flow to very small values. Therefore, it is useful to deal with the energy contained in a turbulent flow in terms of a spectral distribution. It was introduced by Komolgorov in 1941 and is divided into three main regions as can be appreciated in Figure 2-4.

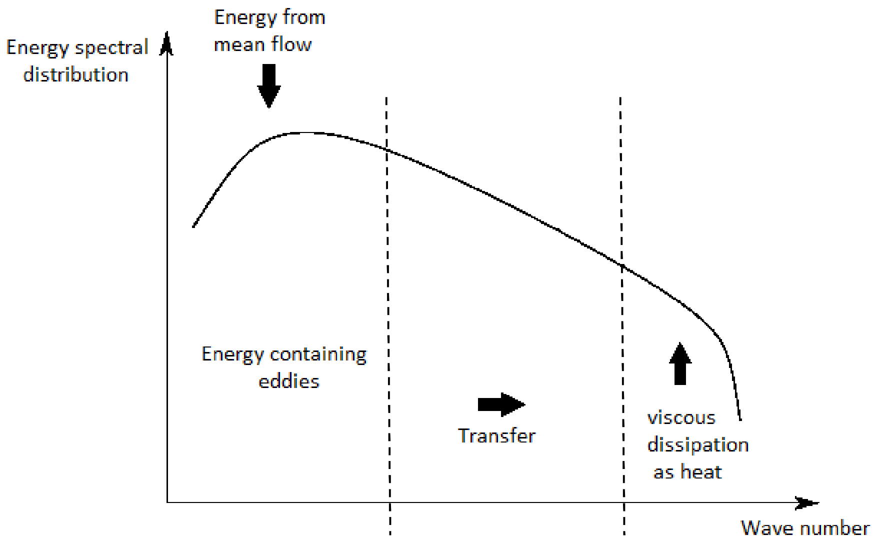

**Figure 2-4 – Energy spectrum of a turbulent flow**

From the spectrum it can be derived that the majority of turbulent energy is contained in the largest eddies. They transfer the energy to the smallest ones by a mechanism called vortex stretching. It is caused by the velocity gradients in the main flow which stretch the large eddies aligned with it by forcing one of its ends to move faster than the other. This produces instabilities that give birth to smaller eddies contained within the bigger one. At the same time, they give birth to new smaller whirls and similarly until the vortices are so small that viscosity becomes important and they are dissipated into heat. This process is called energy cascade.

The turbulent kinetic energy is expressed as:

$$k = \frac{1}{2} \cdot \left(\overline{u'^2} + \overline{v'^2} + \overline{w'^2}\right) \tag{2-12}$$

Assuming that the fluctuations $u', v', w'$ have similar values, the turbulence intensity ($TI$) is defined in percentage with respect to free-stream velocity *U* as:

$$TI = 100 \sqrt{\frac{2}{3} \frac{k}{U^2}} \tag{2-13}$$

The rate at which the larger eddies supply energy $\varepsilon$ is represented by:

$$\varepsilon = -\frac{dk}{dt} \tag{2-14}$$

If the equilibrium conditions are satisfied, $\varepsilon$ is equal to the rate at which turbulent energy is dissipated to smaller eddies. In some flow cases involving shock waves or separation, the rates of production and destruction of turbulent energy differ.

#### 2.2.4.2 Different approaches to turbulence

Because of the necessity to discretize the domain to solve the governing equations of the flow, if all the different turbulent scales were to be captured a very fine mesh would be required. This approach is called DNS (Direct numerical Simulation) and allows to directly solving the full time-dependent Navier-Stokes equations without previously applying any transformation to them.

DNS is used as a research tool in order to, for example, substitute experiments and calibrate turbulence models. Due to the vast amount of economic and time resources required to handle the solution computation in such a fine grid, the approach is not suitable for engineering applications with the current computing capacity of processors.

As has been mentioned in section 2.2.4.1, even if turbulence has a wide range of scales the majority of energy is contained within the largest eddies. In addition, they account for the majority of the transport of momentum, mass and energy. Therefore, another approach to tackle turbulent flows is to represent accurately the large eddies and to approximate the smaller ones. It is called LES (Large Eddy Simulation).

In spite of being less costly than DNS, LES is still too expensive for use as an engineering design tool. Therefore, it is used for research purposes to substitute DNS when either the Reynolds number or the complexity of the geometry are too high. Where applicable, DNS is preferred to LES because it gives more accurate results.

From an engineering point of view, even if we disposed of a very accurate description of the turbulent fluctuations it would probably turn into more useful information after being averaged and summarized as mean values.

This suggests that turbulence could be treated statistically in order to calculate its effect to the mean flow properties. This approach was first introduced by Reynolds in 1895 and is named RANS (Reynolds Averaged Navier-Stokes).

At this point it can be useful to graphically represent the philosophy of the three approaches to turbulence mentioned above: DNS, LES and RANS. Figure 2-5 shows four different signals. The first one represents what would be obtained if a DNS was performed, i.e., the exact history of turbulent fluctuations over time. The second signal is derived from the first one after having applied a partial filtering process by which the high frequency components (third signal) have been eliminated. This is what would be obtained with LES simulations. Eventually, the RANS approach consists of performing a complete filtering of the first original turbulent history and obtaining a mean value for the whole time history. It is represented as the red line.

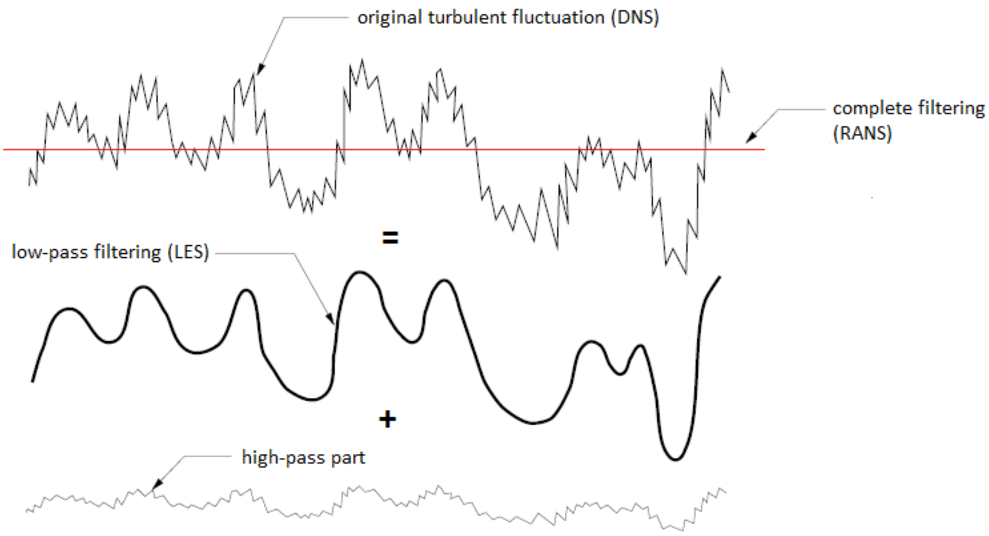

**Figure 2-5 - Schematic of the most common techniques to treat turbulence. Source: adapted from McDonough (2007).**

### 2.2.5 RANS

This approach to tackle turbulent fluctuations is the most widely used as a design tool in engineering applications and it will be employed in this study.

The time history of a turbulent variable $u(x,t)$, such as the one shown in Figure 2-3, is expressed as the sum of a mean value $\bar{u}(x)$ and a fluctuating part $u'(x,t)$:

$$u(x,t) = \bar{u}(x) + u'(x,t) \tag{2-15}$$

Where $\bar{u}(x)$ is expressed as:

$$\bar{u}(x) = \lim_{T\to\infty} \frac{1}{T} \int_{t}^{t+T} u(x,t)dt \tag{2-16}$$

It should be noted that the time average of $u'(x,t)$ is zero. Mathematically:

$$\bar{u}'(x,t) = \lim_{T\to\infty} \frac{1}{T} \int_{t}^{t+T} [u(x,t) - \bar{u}(x)]dt = \bar{u}(x) - \overline{\bar{u}(x)} = 0 \tag{2-17}$$

Even though there is no problem in mathematically defining an infinite time of integration $(T)$, in practice it has to adopt a finite value and therefore $\bar{u}(x)$ is defined:

$$\bar{u}(x) = \frac{1}{T}\int_{t}^{t+T} u(x,t)dt \tag{2-18}$$

The choice of T should be carefully done so that it is very long in comparison to the maximum period of the velocity fluctuations ($T_1$). Moreover, it should also be shorter than the period of the mean flow fluctuations without a turbulent origin such as vortex shedding in a circular cylinder ($T_2$). This is represented in Figure 2-6.

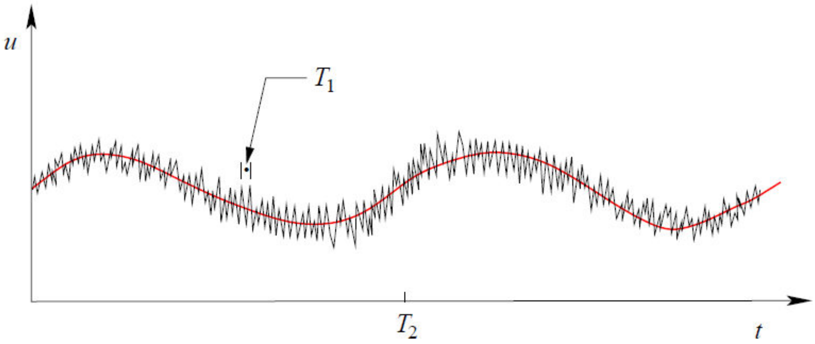

**Figure 2-6 - Time scales involved in RANS modelling. Source: adapted from McDonough (2007).**

After having split the flow variables (Equation (2-15)) they are substituted into the system of equations mentioned in section 2.2.1. For instance, the continuity equation would look like:

$$\frac{\partial(\bar{u}+u')}{\partial x} + \frac{\partial(\bar{v}+v')}{\partial y} + \frac{\partial(\bar{w}+w')}{\partial z} = 0 \tag{2-19}$$

The same procedure is applied to the N-S equations. Finally, a time average is performed to all the equations giving as a result:

$$\frac{\partial\bar{u}}{\partial x} + \frac{\partial\bar{v}}{\partial y} + \frac{\partial\bar{w}}{\partial z} = 0 \tag{2-20}$$

$$\begin{aligned}\rho\frac{d\bar{u}}{dt} = -\frac{\partial\bar{p}}{\partial x} + \rho g_x + \frac{\partial}{\partial x}\left(\mu\frac{\partial\bar{u}}{\partial x} - \rho\overline{u'^2}\right) + \frac{\partial}{\partial y}\left(\mu\frac{\partial\bar{u}}{\partial y} - \rho\overline{u'v'}\right) \\ + \frac{\partial}{\partial z}\left(\mu\frac{\partial\bar{u}}{\partial z} - \rho\overline{u'w'}\right)\end{aligned} \tag{2-21}$$

For the sake of simplicity, only the momentum equation in x direction (2-21) has been shown. A detailed derivation of the time-averaged equations can be found in McDonough (2007). It is not the scope of this study to go inside the details of the mathematical procedure. However, it is worth explaining the average of the product of two fluctuating properties as it will be useful to understand the terms of the final equations obtained.

Taking $u$ and $v$ as the fluctuating variables:

$$\overline{u \cdot v} = \overline{(\bar{u} + u')(\bar{v} + v')} = \overline{\bar{u} \cdot \bar{v}} + \overline{\bar{u} \cdot v'} + \overline{\bar{v} \cdot u'} + \overline{u' \cdot v'} = \overline{u} \cdot \overline{v} + \overline{u' \cdot v'} \qquad \textbf{(2-22)}$$

The terms $\overline{\bar{u} \cdot v'}$ and $\overline{\bar{v} \cdot u'}$ have zero mean because the mean of the fluctuating part is zero. However, the product of the two fluctuating variables does not necessarily have a zero mean.

Physically it can be illustrated by imagining a velocity gradient of a flow as represented in Figure 2-7:

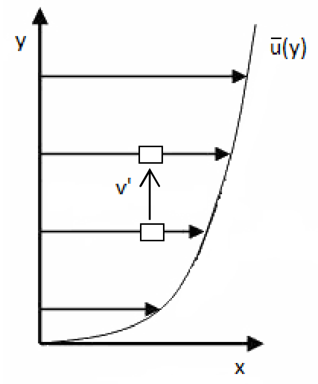

**Figure 2-7 – Transport of momentum due to turbulent velocity fluctuation. Source: adapted from Schlichting (1968)**

Because of the velocity fluctuations in y direction ($v'$) some particles of fluid will be travelling upward or downward. If we imagine a particle which moves upward ($v' > 0$), then it will move from a region where the horizontal velocity $\bar{u}$ is lower to a region where it is higher. Since the particle will tend to maintain the original $\bar{u}$ it will give rise to a negative fluctuating velocity $u'$ which will compensate the increase in $\bar{u}$. Because of that, the product $u' \cdot v'$ would not be zero and it is said to be correlated.

If the Reynolds-averaged equations are examined, no significant changes can be appreciated in the continuity equation (2-20) apart from the substitution of the initial variables by the average quantities.

With regard to the momentum equation (2-21), aside from this substitution new correlation terms in the form of $\overline{u_i'u_j'}$ appear. For instance, in x direction the terms are $-\rho\overline{u'^2}$, $-\rho\overline{u'v'}$, $-\rho\overline{u'w'}$. They are referred to as turbulent stresses as they have the dimensions of stress and are grouped together with the laminar stress terms. However, strictly they represent convective acceleration terms.

To conclude, the Reynolds-averaging process enables to transform the governing equations in a manner that “unsteady structures of small sizes are eliminated and expressed by their mean effect on the flow through the so-called Reynolds or turbulent stresses” (ERCOFTAC, 2000, p. 20). However, as a result of this transformation six new unknowns are generated. Hence, some techniques known as turbulence modelling are required to close the system of equations composed of the continuity and time-averaged Navier-Stokes equations.

### 2.2.5.1 Turbulence modelling

One of the simplest ways to tackle the closure problem posed by the Reynolds stresses consists of expressing them in terms of the averaged velocity gradients (strain rates) of the flow assuming that they are proportionally related by a scalar turbulent or eddy viscosity $\mu_T$. Mathematically:

$$-\rho\overline{u_i'}\,\overline{u_j'} = \mu_T\left(\frac{\partial\overline{u_i}}{\partial x_j}+\frac{\partial\overline{u_j}}{\partial x_i}\right) \tag{2-23}$$

*where the term $-\rho\overline{u_i'}\,\overline{u_j'}$ represents the Reynolds stress, $\mu_T$ the eddy viscosity, the term inside the parenthesis the strain rates and $\rho$ the density*

This approach is known as the Boussinesq approximation and is inspired in the viscous stresses of a Newtonian fluid in laminar motion (equation (2-1)).

It is important to note that the viscosity of the fluid $\mu$ is an intrinsic property of the flow whereas $\mu_T$ depends upon the state of turbulence and therefore needs to be calculated. From dimensional analysis, the term $\frac{\mu_T}{\rho}$ can be expressed proportionally in terms of $V$ and $L$ as:

$$\frac{\mu_T}{\rho} \propto V \cdot L \tag{2-24}$$

*where $V$ and $L$ are a velocity and a length scale respectively of the larger turbulent motions.*

At this point it is useful to summarize the reasoning that has been done so far. Firstly, the Reynolds-averaging process has generated six new unknowns (Reynolds or turbulent stresses) to the original system of equations. In order to close it, the Reynolds stresses have been related to the mean flow strain rates by means of the introduction of a new variable called turbulent viscosity. Therefore, the six unknowns have been reduced into one: $\mu_T$.

Eventually, $\mu_T$ has been expressed in terms of a velocity and length scale of the larger turbulent motions. Hence, the closure problem has now been reduced to the calculation of these two values. The different ways of computing them give rise to different turbulence models. As all of them are based on the Boussinesq approximation they are grouped under the label *linear eddy viscosity models*. The most widely used are represented in Table 2-1.

For cases involving strong separation or swirling of the flow, the Boussinesq approximation leads to spurious results. Thus, another approach has been proposed which consists of directly determining the turbulent stresses by solving six additional transport equations. These methods are called second moment closure models (SMC) or Reynolds stress transport models (RSTM).

Because of the higher computational requirements of SMC, another approach to handle flows with complex strain which cannot be accurately represented by the linear eddy viscosity models has been proposed. It is called non-linear eddy viscosity and, as derived from the name, relies also on the Boussinesq approximation but includes extra highest order terms which allow for a better calibration to experimental data.

| **Linear eddy viscosity models** |
|---|
| -Algebraic (or zero-equation) models<br>-One-equation models<br>-Spalart and Allmaras<br>-Two-equation models<br>-Standard k-ε, Realizable k-ε, RNG k-ε<br>-k-ω<br>-Menter model, SST k- ω |
| **Reynolds stress or second moment closure models** |
| **Non-linear eddy viscosity models** |

**Table 2-1 – Main turbulence models categories and examples. Source: adapted from ERCORTAC (2000).**

#### *2.2.5.1.1 Linear eddy viscosity models*

In this study the focus is on the linear eddy viscosity models, particularly two-equation models which are the most widely used for general engineering applications.

As has been mentioned in the section above, the aim is to compute the values of the velocity and length scales of the largest turbulent eddies to derive the value of the turbulent eddy viscosity.

One of the simplest ways to achieve this aim is to use algebraic equations which relate the length and velocity scales to the local properties of the flow. Because of that, this approach is referred to as *algebraic models*. ERCOFTAC (2000) do not recommend using them for general applications of RANS models.

In order to take into account the history of the flow to determine the turbulent viscosity, the one-equation models have been proposed as an improvement of the algebraic models. As the name suggests, an extra transport equation is solved and enables to determine the value of $k$ (turbulent kinetic energy per unit mass, defined in section 2.2.4.1) which is afterwards related to the velocity scale (Table 2-2). Contrarily, the length scale has to be determined algebraically from the local properties of the flow as in algebraic models.

One of the most popular one-equation models was proposed by Spalart and Allmaras (S-A). It is specially designed for aerodynamic applications for flow around aerofoils and has been successfully tested. However, “the model is not well-suited for more general flows, as it leads to serious errors even for simple shear flows” (ERCOFTAC, 2000, p. 32).

The two-equation models allow to compute both the velocity and length scales taking into account the flow history by solving two additional transport equations. One of them serves the same purpose as in the one equation models and is used to calculate the velocity scale from $k$. Contrarily, the other substitutes the algebraic expression for $L$ and enables to calculate it without having to rely only on local properties.

The most widely used variables to calculate the length scale are either the turbulent dissipation rate ε (described in section 2.2.4.1) or a frequency of the largest eddies ($\omega$). The former are referred to as k-ε models and the latter as k-ω models. Table 2-2 details the relationship between the dimensional scales and the variables ε and ω.

| | k-ε models | k- ω models |
|---|---|---|
| Velocity scale ($V$) | $V \; \alpha \; k^{\frac{1}{2}}$ | $V \; \alpha \; k^{\frac{1}{2}}$ |
| Length scale ($L$) | $L \; \alpha \; C_{\mu} \frac{k^{\frac{3}{2}}}{\epsilon}$ | $L \; \alpha \; \frac{k^{\frac{1}{2}}}{\omega}$ |

**Table 2-2 – Calculation of the dimensional scales by k-ε and k- ω**

#### 2.2.5.1.1.1 k-ε turbulence models

There exist a number of different turbulence models which are labelled as k-ε (Table 2-1). An accurate description of all of them goes beyond the scope of this study.

The focus will be on a typical commonly used turbulent model called *standard k-ε model*. It has been widely used and validated against many practical engineering flows and it is “a de-facto standard in industrial applications” (ERCOFTAC, 2000, p. 22).

Tu et al. (2008) suggest that it should be selected as a starting point for turbulence calculations when the knowledge of the flow is limited and no other turbulence models is expected to perform better. He also mentions that *standard k-ε* models very successfully confined flows where Reynolds stresses are important, as well as flows with thin shear layers and boundary layers.

Notwithstanding, Tu et al. (2008) highlight the model limitations when dealing with unconfined flows. It poorly predicts the swirling flows with rapid strain such as those found in highly curved boundary layers and diverging passages. Moreover, it also fails in accurately representing the flow separation caused by adverse pressure gradients. ERCOFTAC (2000, p.27) state that "the real flow is likely to be much closer to separation (or more separated) than the calculations suggest".

To improve the performance of the standard k-ε model new more sophisticated models such as realizable k-ε or RNG k-ε have been derived. They lead to more accurate solutions of the flow for some specific applications but they reduce the model's generality.

#### 2.2.5.1.1.2 k-ω turbulence models

In contrast with k-ε, "[k-ω] works exceptionally well particularly under strong adverse pressure gradients" and "[it] has been shown to perform splendidly close to walls in boundary layer flows" (Tu et al., 2008, p. 258). The model main shortcoming is its high sensitivity to free stream values of $\omega$. It means that wrong results will be obtained if the value is not correctly prescribed.

#### 2.2.5.1.1.3 Menter model

Menter (1994, quoted in Tu et al., 2008, p. 258) proposed a model which combines the strengths of both k-ε and k-ω models, i.e., it keeps the formulation of k-ω models close to the wall and gradually blends to k-ε away from it. Tu et al. (2008) state that this enables to take advantage of the good performance of k-ω close to walls and of the fact that k-ε is less sensitive to free-stream values.

#### 2.2.5.1.1.4 SST k-ω

The turbulent non-equilibrium conditions of the boundary layer found in flows involving shock waves or separation have been already mentioned in section 2.2.4.1. In such cases, the rates at which turbulence is generated and dissipated differ. This phenomenon cannot be accurately handled by the two-equation models described above and therefore new models such as Shear Stress Transport k-ω (SST k-ω) have been proposed.

SST k-ω is a variation of Menter model and ERCOFTAC (2000) state that it can improve considerably the prediction of flow separation under adverse pressure gradients. Notwithstanding, “SST should not be viewed as a universal cure” (Tu et al., 2008, p. 259) as, for example, the model’s capabilities in dealing with flow recovery after reattachment are reduced.

### 2.2.5.2 Extra modelling techniques

In the previous sections, turbulent flows have been addressed by providing a general characterization of the physics of turbulence and a description of the mathematical modelling approaches to it with the focus on two-equation models.

Laminar flows have not been examined in detail because of its higher simplicity which enables to tackle the governing equations of the flow in a straightforward manner.

Both types of flows have been treated separately but, in practical applications involving turbulent flow, regions of laminar motion are also present. This can be due to the fact that the flow transitions from laminar to turbulent state inside the boundary layer but mainly it is because of the importance of molecular viscosity in the boundary layer region close to the wall which suppresses the turbulent fluctuations in it.

Both facts involve using extra modelling techniques to account for the presence of laminar flow and make it compatible with the use of a turbulence model. They will be explained in the following sections.

#### *2.2.5.2.1 Near-wall modelling*

Experimental measurements have revealed that both laminar and turbulent stresses are not equally distributed inside a turbulent boundary layer. The former dominate near the wall whereas the latter become important far from it. Because of that, the boundary layer is usually divided into three different regions referred to as viscous wall layer, overlap layer and outer turbulent layer as shown in Figure 2-8. As the name suggests, the overlap layer bridges the viscous wall layer and the turbulent layer and within it both laminar and turbulent stresses are important.

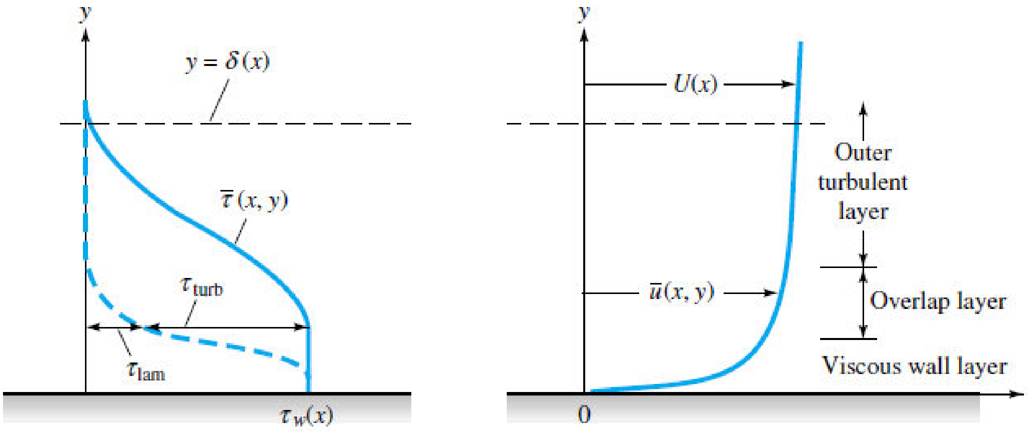

a) Typical shear distribution

b) Typical velocity distribution

**Figure 2-8 – Turbulent flow near a wall – Source: adapted from White (2007)**

With regard to the region of the boundary layer close to the wall, two non-dimensional parameters for velocity and distance are used to describe it. The former is defined as:

$$u^{+} = \frac{U}{\left(\frac{\tau_w}{\rho}\right)^{\frac{1}{2}}} \tag{2-25}$$

*where $U$ is the free stream velocity, $\tau_w$ is the wall shear stress and $\rho$ the density of the fluid.*

The latter is expressed as:

$$y^{+} = \frac{\left(\frac{\tau_w}{\rho}\right)^{\frac{1}{2}} \cdot y}{\nu} \qquad \textbf{(2-26)}$$

*where $\nu$ represents the cinematic viscosity of the fluid and $y$ is the distance from the wall.*

As can be appreciated, the term $\left(\frac{\tau_w}{\rho}\right)^{\frac{1}{2}}$ appears in both expressions. It is known as wall friction velocity (as it has dimensions of velocity) and is represented by $u_\tau$. Therefore, the equations (2-25) and (2-26) can be rewritten as:

$$u^{+} = \frac{U}{u_\tau} \qquad \textbf{(2-27)}$$

$$y^{+} = \frac{u_\tau \cdot y}{\nu} \qquad \textbf{(2-28)}$$

With respect to the outer turbulent layer, the distance from the wall is expressed in non-dimensional form in terms of the boundary layer thickness as $\frac{y}{\delta}$. The non-dimensional velocity is expressed as $\frac{U-\bar{u}}{u_\tau}$.

The existence of the three regions in the turbulent boundary layer mentioned above has enabled to derive a universal form to express its stream wise velocity valid for both internal and external flows. The combination of dimensional analysis and experimentation has led to the representation in Figure 2-9.

Tu et al. (2008) emphasise that the universal profile represented in Figure 2-9 has been obtained from experiments on “an attached two-dimensional Couette flow[2] configuration with the assumptions of small pressure gradients, local equilibrium of turbulence and a constant near-wall stress layer” (Tu et al., 2008, p. 261).

---

[2] Couette flow refers to the laminar flow of a viscous fluid formed between two parallel plates with relative motion.

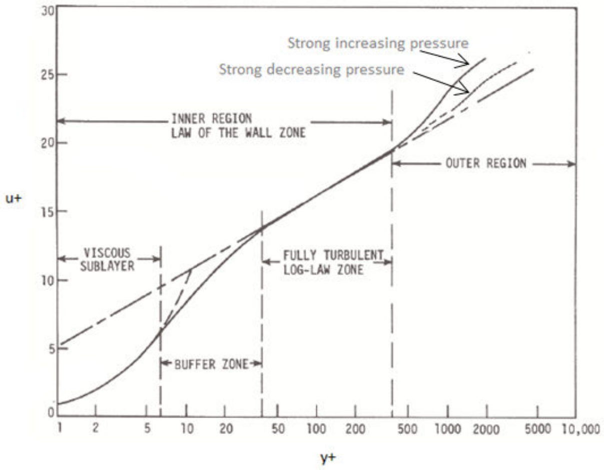

**Figure 2-9 – Experimental verification of turbulent wall flow. Source: adapted from White (2007)**

For the viscous wall layer, the variables $u^+$ and $y^+$ are related by the known law of the wall expressed as:

$$u^+ = F(y^+) \tag{2-29}$$

Specifically for $y^+$ values lower than 5, equation (2-29) takes the form:

$$u^+ = y^+ \tag{2-30}$$

With respect to the outer layer, equation (2-31) known as velocity-defect law relates the non-dimensional velocity and distance as:

$$\frac{U - \bar{u}}{u_\tau} = G\left(\frac{y}{\delta}\right) \tag{2-31}$$

Both the law of the wall (2-29) and the velocity defect law (2-31) blend in the overlap layer which spans approximately from $y^+$=30 to $y^+$=500. It is governed by the logarithmic overlap layer equation which is expressed as:

$$\frac{u}{u_\tau} = \frac{u}{K} ln \frac{y \cdot u_\tau}{\nu} + B \tag{2-32}$$

*where $K$ and $B$ are constants determined experimentally. $K$ is known as Von Kármán constant and $B$ the wall roughness constant.*

It is important to highlight that, contrarily to the outer-law profiles which are sensible to the external pressure gradients as appreciated in Figure 2-9, the wall law is unique. Thus, it can be used to characterize the viscous wall layer region without having to solve the equations presented in previous sections.

This near-wall modelling approach is known as wall-functions. It eliminates the difficulties arisen from the use of turbulence models which cannot be applied close to the wall such as the standard k-ε.

However, the use of wall functions to model the near wall region is not free from weaknesses and therefore another alternative approach is used. It consists of fully resolving the boundary layer, from the near wall to the outer layer, and can only be applied in conjunction with appropriate turbulent models such as SST k-ω which can deal with the boundary layer region close to the walls. Such turbulent models are referred to as low Reynolds number models.

In the following subsections, the focus will be on the practical consequences of applying either wall functions or low Reynolds models to the CFD simulation.

#### 2.2.5.2.1.1 Wall functions approach

The aim of using wall functions approach is to avoid explicitly solving the near-wall region inside the boundary layer. The flow solution is calculated outside this complex region and the results are bridged to the wall by means of the wall functions. Therefore, care must be taken so that the points of the mesh close to the wall do not fall inside the viscous layer.

In order to satisfy this, many best practice guidelines (ERCOFTAC, 2000; Tu et al., 2008) suggest that the points of the mesh adjacent to the wall should have values of y+ slightly above 20 or 30. STAR-CCM+ user-guide (2013) states that values of y+ up to 200-300 are also tolerated.

Although the range of lower limit values for y+ seems to be very wide, it becomes more constrained when the requirement for a correct boundary layer resolution is added. Even though the use of wall functions eliminates the need to solve the complex near wall region, it does not free the user to correctly solve the turbulent part of the boundary layer. An accurate resolution is deemed to be achieved if at least 8-10 points are placed inside the boundary layer (Tu et al., 2008; ERCOFTAC, 2000). Figure 2-10 (b) shows a schematic of a mesh for the use of wall functions.

ERCOFTAC (2000) consider the cases in which the boundary layer Reynolds number is below $10^5$ as difficult ones in terms of satisfying both good resolution and valid y+ value for the wall adjacent mesh point. For such cases they suggest using y+ values slightly above 20.

From the definition of y+ (equation (2-28)) it can be deduced that its value depends on the flow solution which obviously is not known prior to calculations. Thus, the generation of a mesh with appropriate y+ values by a trial an error procedure can be difficult and time consuming.

To facilitate the process, ERCOFTAC (2000) suggests using previously computed similar cases as guideline. For cases where this information is not available, STAR CCM+ user-guide (2013) provides another approach explained in Appendix B.

Because of the dependence of y+ on the wall shear stress, satisfying the requirements of y+ higher than 20 or 30 may be difficult in some situations such as flow separation. For such case $\tau_w$ becomes zero and so does y+ irrespective of the value of y.

To overcome the problem, ERCOFTAC (2000) states that many commercial codes use an equivalent definition for y+ based on turbulent kinetic energy expressed as:

$$y^* = \frac{y \cdot \rho \cdot (C^{-1} \cdot k)^{\frac{1}{2}}}{\mu} \qquad \textbf{(2-33)}$$

*where C is a constant.*

Both Tu et al. (2008) and ERCOFTAC (2000) underline the necessity to be aware of the fact that the wall functions relationships have been derived from a specific type of Couette flow as explained in section 2.2.5.2.1. “Applying the wall functions outside this application range will lead to significant inaccuracies” (Tu et al., 2008, p. 261). Therefore, care should be taken to check the validity of the functions to the problem that is being solved.

#### 2.2.5.2.1.2 Low Reynolds number model approach

For cases where the characteristics of the flow cannot be modelled with wall functions without leading to important errors, the low Reynolds number model approach is used. As it consists of fully solving the boundary layer, care must be taken so that the nodes of the mesh adjacent to the wall fall inside the viscous sub-layer. Tu et al. (2008) and ERCOFTAC (2000) suggest that the values of y+ should be close to unity. However higher values of y+ such as 4 or 5 are also accepted as long as the nodes near the wall fall inside the viscous sub-layer.

Similarly to the wall functions, it is important to ensure that a good resolution of the boundary layer is achieved. ERCOFTAC (2000) suggests having from 30 to 60 grid nodal points inside the boundary layer. From this it can be deduced that the size of the mesh will be bigger than the equivalent mesh for the use of wall functions. Because of that, “the cost of the solution is around an order of magnitude greater than when wall functions are used” (Tu et al., 2008, p. 262).

Figure 2-10 (a) shows a schematic of a mesh for the use of low Reynolds number models.

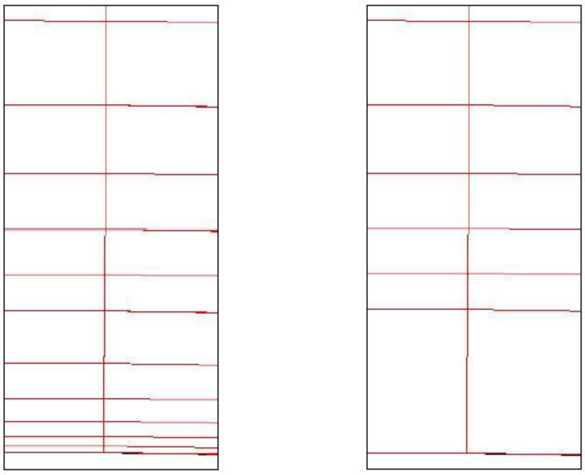

a) Full grid b) Grid for use with a wall function

**Figure 2-10 – Different near-wall modelling mesh strategies**

#### *2.2.5.2.2 Transition*

Transition is an important physical phenomenon for engineering applications. It influences important quantities such as skin friction, which may be increased leading to higher values of drag force acting on a body.

Different transition models have been proposed to be combined with CFD codes and their use is influenced by the application, level of accuracy and computational resources available.

Pasquale et al. (2009) undertook a review of the transition models most widely used analysing their strengths and weaknesses. They stated that the low Reynolds number turbulence models have the capability to predict transition although their ability to do it is questionable. That is mainly because “at best, low Reynolds number models can only be expected to simulate bypass transition[3]” (Pasquale et al., 2009, p. 3).

Despite being a complex phenomenon, Pasquale et al. (2009) state that RANS methods and relatively simple models are able to capture the most significant effects of transition with sufficient engineering accuracy. This is mainly because “in many applications, transition is constrained to a narrow area of the flow due to geometric features, pressure gradients and/or flow separation” (Pasquale et al., 2009, p. 9).

As has been explained in section 2.2.5.2.1, wall functions are derived from a fully turbulent boundary layer and, therefore, their use precludes any transition prediction capability.

For flows where the onset point of transition is known a priori, a strategy used to improve the performance of wall functions is to supress the turbulence in the laminar region. In Star CCM+ this approach can be implemented with the *turbulence suppression model* and, although it is referred to as transitional model, it does not have predictive capability.

---

[3] Bypass transition in the boundary layer is caused by large disturbances outside it, typically levels of free stream turbulence above 1%. Other types of transition are natural and separation induced transition.

Star CCM+ also incorporates a more sophisticated transitional model called Gama ReTheta which is only applicable in conjunction with SST k-ω and improves the predictive capability of this low Reynolds number model.

### 2.2.6 Errors

During the process of obtaining a flow solution using CFD, many uncertainties and errors stemming from different sources arise. Generally, they are classified into discretization errors, round-off errors, convergence errors, physical-modelling errors and human errors (Tu et al., 2008). Because of that, the solution obtained should not be approved unless a quantitative assessment of these errors has been performed by means of verification and validation procedures.

The former generally involves performing mesh and time step sensitivity studies to estimate the discretization error, as well as a thorough checking of input parameters and boundary conditions.

The latter consists of comparing the computed results with experimental data to determine to which extent the computed solution represents the real physics of the problem. None of the turbulence models explained in section 2.2.5.1.1 is capable of representing any kind of flow. Therefore, it is of fundamental importance to check which of them is in closer agreement with experiments.

ERCOFTAC (2000) suggest that, for complex flows, the problem can be broken into more simple representative individual flows which should be validated with existing experimental data. This is precisely the strategy which has been followed in the present study.

## 2.3 PONTOONS

The shape of PLAT-O prototype pontoons is very similar to the hull form of an AUV (Autonomous Underwater Vehicle) or a torpedo as can be appreciated in Figure 2-11. For both the former and the latter, the calculation of the total drag is of fundamental importance as it determines their powering requirements. Thus, it is not surprising that several studies (Alvarez et al., 2009; Phillips et al.,

2007) have been conducted to assess the capabilities of different numerical tools in predicting their resistance.

The aim of this section is to highlight relevant features of CFD simulations performed on the devices mentioned above, with particular emphasis on important validation considerations.

a) PLAT-O pontoon b) Autosub AUV c) Torpedo

**Figure 2-11 – Pontoon similar geometries. Source: (b) AUVAC; (c) Sanci (2006)**

### 2.3.1 Geometry

The differences between the idealized CAD geometry and the real manufactured body used for experimental testing may introduce uncertainties to the validation of results. These differences may not only be caused by manufacturing issues such as the smoothness of the surface finish but also they may originate from the experimental set up. For instance, the use of jubilee clips to link two bodies is of common practice in towing tank tests.

In his study of the drag on submersible vehicles, Allmendinger et al. (1990) refer to the first source of difference and mention that additional resistance coefficients from 0.0004 to 0.0009 can be added to the form and viscous drag terms to account for the finish quality when ITTC 57 curve is used to estimate the drag.

Stevenson et al. (2009) addressed the effect of AUV ancillary systems and manufacturing imperfections using CFD and concluded that they have a significant contribution to the drag. However, they pointed out that the effect is higher for a bulbous hull shape than for a torpedo form. The former is used to maintain laminar flow in the majority of the body length and any small disturbance can trigger transition in the boundary layer therefore leading to an increased resistance.

### 2.3.2 Domain boundaries

The flow characteristics around an AUV in a towing tank are different from those found when the device is operating in open water because of the constraints imposed by the tank walls and the free surface effects. The latter were addressed by Hoerner (1965) who determined that below depths of five body diameters the wave resistance can be considered negligible.

With respect to the tank walls, they impose a blockage effect on the flow which may result in an increased resistance in comparison with open water tests. The towing tank limited dimensions can be directly compared to the extents of the CFD domain boundaries. This means that care must be taken to ensure that it represents accurately the flow characteristics which want to be simulated.

In that sense, Phillips et al. (2007) recommend placing the boundaries of the CFD domain at the same location of the tank walls in case the blockage effects want to be modelled. Contrarily, to replicate the open ocean conditions they suggest performing a sensitivity analysis of the boundary locations to analyse their effect on the predicted resistance. The final choice for the domain size is driven by a compromise between mesh sizes and level of flow constrainment.

### 2.3.3 Turbulence modelling

As mentioned in section 2.2.6, no turbulence model is valid to handle any type of flow and therefore validation is required. Phillips et al. (2007) state that the use of k-ε and SST k-ω led to very similar results for the total drag resistance of the Autosub AUV and in good agreement with experimental data. Moreover, they observed high correlation between the skin friction predictions from ITTC 57 curve and from CFD.

### 2.3.4 Validation using ITTC 57

Several studies (Phillips et al. (2007); Allmendinger et al. (1990); Alvarez et al. (2009)) have made use of ITTC 57 curve as an empirical tool to estimate the viscous drag of a UAV and to contrast the CFD results with. However, care should be taken to determine to which extent the characteristics of the flow around the body analysed satisfy the hypothesis used to derive the empirical ITTC curve.

For the particular case of UAV, a study by Alvarez et al. (2009) shows that for hull shapes similar to a torpedo (Figure 2-12 (a)) where flow separation is likely to occur the predictions of resistance using ITTC 57 are in clear disagreement with experimental results. Contrarily, for streamlined hull shapes (Figure 2-12 (b)) the estimations of resistance nicely reproduce experimental measurements.

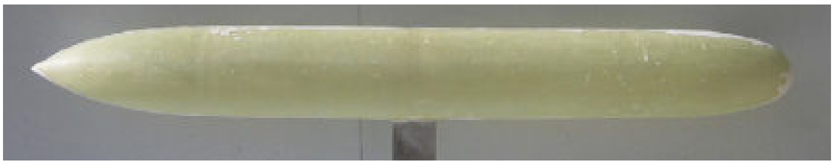

a) Torpedo-like hull shape

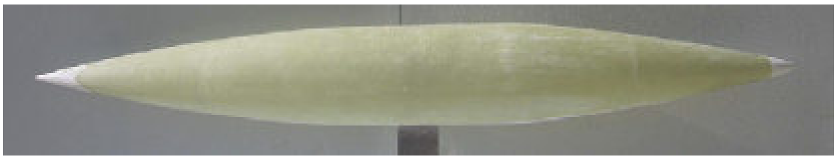

b) Streamlined hull shape

**Figure 2-12 – AUV hull shapes. Source: Alvarez et al. (2009)**

### 2.3.5 Results

Phillips et al. (2007) found very good agreement between the CFD drag calculations on two different AUV hulls (Autosub and C-Scout) and the towing tank tests experimental results. The calculations were performed using ANSYS CFX software with RANS modelling and k-ε turbulence models. However, the CFD calculations under predicted the total resistance of SOTON AUV. The reasons are deemed to be both the simplifications on the geometry simulated and the effect of the free surface which was not modelled in CFD.

The velocity contours and the pressure coefficient distribution around Autosub AUV obtained by Phillips et al. (2007) are represented in Figure 2-13.

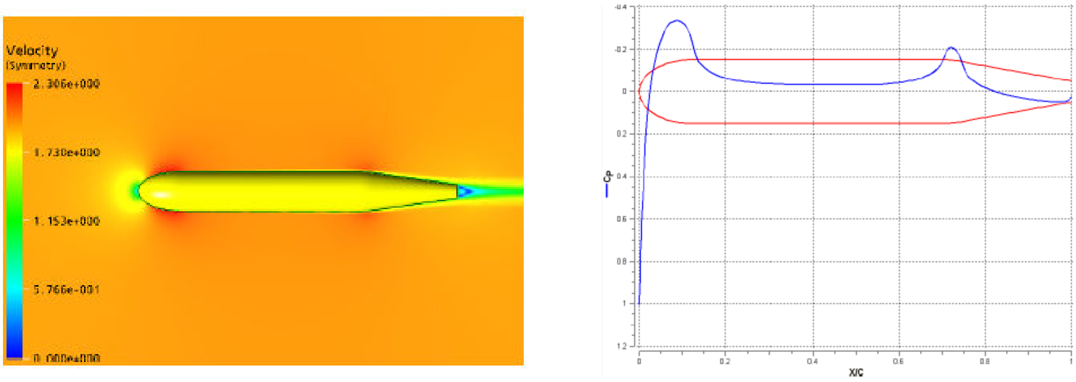

a) Velocity contours b) Pressure coefficient distribution

**Figure 2-13 – Autosub AUV CFD results. Source: Phillips et al. (2007)**

## 2.4 CYLINDRICAL STRUTS

The PLAT-O prototype space frame is composed of both elliptical and cylindrical struts (Figure 2-14 (a)). The latter are a common structural element employed, for example, in many offshore platforms and truss spars (Figure 2-14 (b);(c)). The unsteady vortices shed behind a circular cylinder give birth to interactions between the fluid and the structure which need to be assessed in the design. Therefore, it is not surprising that several studies (Constantinides et al. (2011); Atluri et al. (2006)) have been conducted to address the capabilities of CFD to model the dynamic response of the structures mentioned above.

a) PLAT-O prototype b) Offshore platform c) Truss spar

**Figure 2-14 – Space frame similar geometries. Source: (b) 2b1$^{st}$Consulting, (c) Atluri et al. (2006)**

In the context of the present study, the focus is not on the fluid structure interaction problem. Contrarily, it is on the important engineering parameters used to characterize the flow around a cylinder, such as drag, and the capabilities of CFD to predict them.

A good understanding of the most relevant features of the flow enables to better address the modelling limitations of the present CFD codes. Because of that, the first part of this section has been devoted to a general description of the flow around a cylinder and the important parameters used to describe it. The second and third parts have been focused on previous relevant CFD simulations performed on isolated cylinders and on cylinder arrays similar to PLAT-O space frame respectively.

### 2.4.1 Flow characterization

A vast number of different steady and unsteady flow patterns have been observed around circular cylinders over a wide range of Reynolds numbers. Some examples are shown in Figure 2-15.

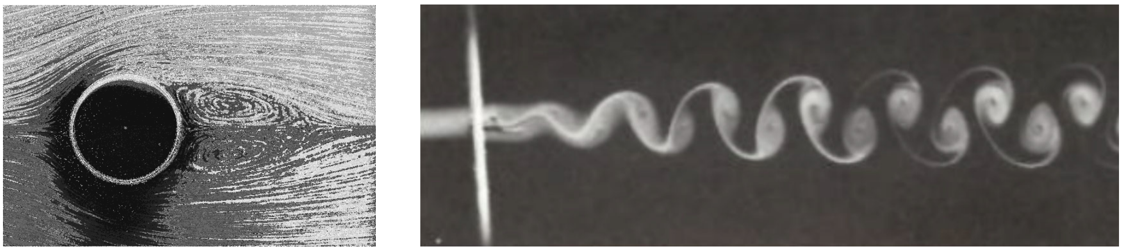

a) Twin circulation at Re=24 b) Fully developed Kármán street at Re=100

**Figure 2-15 – Different flow patterns of the flow around a circular cylinder. Source: COMSOL (a); Zdravkovich (1997) (b)**

Zdravkovich (1990) relates this behaviour to the mechanism by which the laminar flow around a circular cylinder becomes fully turbulent. He highlights that it is caused by different transitions which take place in several disturbed regions of the flow. In the first state, the laminar vortices in the wake become turbulent. The next transition occurs in the free-shear layers. It gradually moves toward the separation point and triggers the third transition around it. The last transition occurs in the boundary layer and moves to the stagnation point with increasing Reynolds number. Eventually, all the regions of the flow become fully turbulent.

Zdravkovich (1997) underlines the effect on the drag force that the transition around separation produces. Because of the change of the separated flow from laminar to turbulent, it reattaches to the wall and delays separation. Therefore, the width of the wake is decreased and so is the drag. This phenomenon is usually called ‘drag crisis’ and can be appreciated in Figure 2-17 (a) on an approximate Reynolds of $2 \cdot 10^5$.

Because of this behaviour, some authors (Roshko, 1960; Hallam et al., 1977) classify the different flow regimes into subcritical, super critical and critical as appreciated in Figure 2-17. Zdravkovich (1997) proposed an alternative classification based on transitions. For engineering purposes, the former classification has been more widely extended and is incorporated in many standards such as DNV-RP-C205 (2010).

The unsteadiness of the vortices shed behind the cylinder produce fluctuating forces both in the direction and transverse to the flow (drag and lift respectively). In their book, Hallam et al. (1977) define a *pair* as “the sequence of a vortex shed form one side followed by a vortex shed from the other side [of the cylinder]” (Hallam et al., 1977, p. 347). Based on the *pair* concept, the frequency of vortex shedding is defined as “equal to that at which pair of vortices are shed” (Hallam et al., 1977, p. 347). Therefore, from the definition above it can be derived that the vortex shedding frequency can be obtained from the oscillation of the lift force and that it is half the oscillation frequency of the drag force (Figure 2-16).

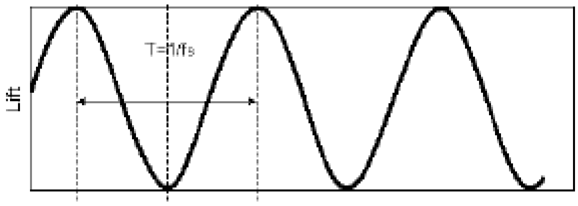

a) Lift fluctuation

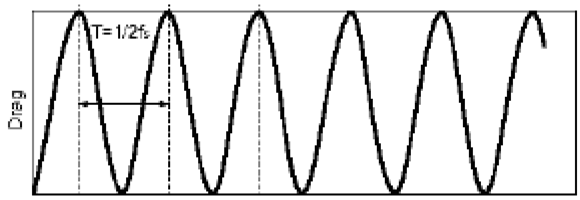

b) Drag fluctuation

**Figure 2-16 – Drag and lift fluctuations. Source: Liaw (2005)**

The vortex shedding frequency is normally expressed by means of the Strouhal number defined as:

$$St = \frac{f \cdot u}{D}$$

*where $f$ is the frequency of vortex shedding, $u$ is the free-stream velocity and $D$ is the diameter of the cylinder.*

From experiments both Reynolds and Strouhal numbers can be related (Figure 2-17 (b)). The lack of experimental data for Reynolds slightly above $1 \cdot 10^5$ is due to the fact that, at this range, either the vortex shedding ceases or the Strouhal number rises dramatically (Cox et al., 1997).

Zdravkovich (1990) studied the influence of disturbances such as surface roughness and free shear turbulence to the flow around a circular cylinder and concluded that they have an important effect as “they can initiate transition at a lower Reynolds number and can inhibit some flow structures” (Zdravkovich, 1990, p. 61). With respect to the latter, Cox et al. (1997) state that experimental data has shown that higher levels of turbulence lead to lower lift amplitudes.

This fact is important in understanding the wide scatter of data from experiments. Some authors (Cox et al. (1997); Hallam et al. (1977)) have used a band which comprises the range of experimental data as can be appreciated in Figure 2-17.

With respect to the pressure coefficient, Zdravkovich (1997) states that there exist significant scatter at a Reynolds number close to the critical region because of the different conditions at which experiments were performed.

Contrarily, at the laminar region there is little scatter of data and no variation of $C_p$ with respect to the Reynolds number can be appreciated between 36<Re<107.

It has to be underlined that the study by Zdravkovich (1997) has focused on cylinders oriented perpendicular to the flow. As can be appreciated from Figure 2-14, the majority of PLAT-O cylindrical struts are inclined. Hoftyzer et al. (2010) state that extensive studies focused on the flow around inclined cylinders have been performed to analyse their flow characteristics which differ from the ones oriented perpendicular to the flow. Due to the time constraints of the present study, the subject of inclined cylinders has not been addressed in depth.

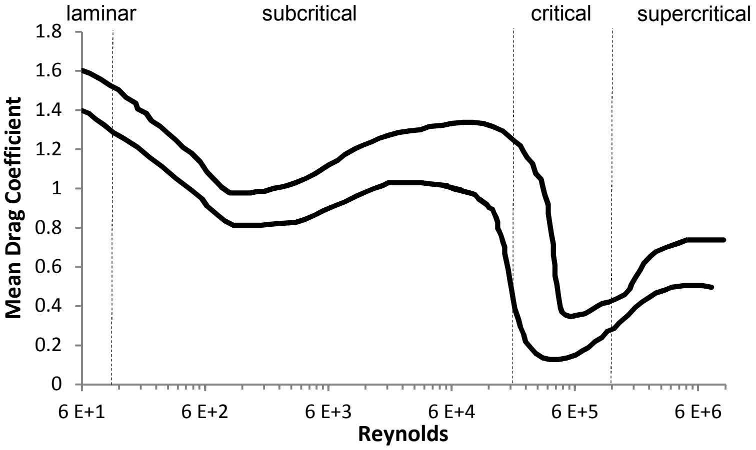

a) Drag coefficient experimental data

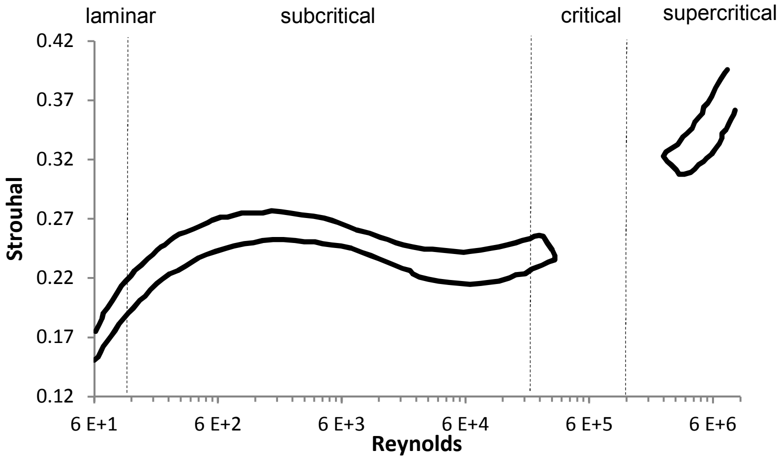

b) Strouhal number experimental data

**Figure 2-17 – Experimental data. Source: adapted from Cox et al. (1997)**

## 2.4.2 Isolated cylinders

### 2.4.2.1 Geometry

Above a Reynolds number of approximately 180, Mittal et al. (1995) state that the flow around a circular cylinder becomes three-dimensional. Because of that, Cox et al. (1997) mention that CFD simulations on 2D geometries have raised doubts about their capability to represent important engineering quantities such as drag, lift and vortex shedding frequency.

In the study of Mittal et al. (1995) the discrepancy of results derived from two-dimensional and three-dimensional CFD simulations was assessed. The three-dimensional results showed agreement with experimental data but contrarily, two-dimensional results presented significant differences. Mainly, the drag was over predicted by 2D simulations and the lift peak-to-valley values were found to be greater than for 3D simulations.

In spite of these differences, the study of Cox et al. (1997) showed that 2D CFD simulations can capture some of the mechanism responsible for the existence of different flow regimes from subcritical to supercritical.

### 2.4.2.2 Domain boundaries

Several studies (Rumsey et al., 1987, quoted in Cox et al., 1997, p. 3; Mittal et al. (1995)) have addressed the influence of the computational domain boundaries on the results obtained from the CFD simulations of flow around a cylinder.

With respect to the outlet boundary location, the study by Rumsey et al. (1987, quoted in Cox et al., 1997, p. 3) indicated that for a 20 diameter grid extent the discrepancy of the Strouhal number when compared to the extrapolation of an infinite grid was relatively small.

This result is in accordance with a study by Mittal et al. (1995) in which they further demonstrated that the quantities such as lift, drag and Strouhal are independent of the size of the computational domain.

Notwithstanding, Liaw (2005) obtained pressure coefficient values higher than one at the stagnation point in disagreement with experimental data. He points at the inlet boundary distance from the cylinder as the cause of discrepancy.

#### 2.4.2.3 Time discretization

In section 2.4.1, the unsteady vortical structures representative of the flow around a cylinder have been addressed. In order to capture such patterns with a CFD simulation the time step needs to be carefully chosen.

Several studies (Rumsey, 1996, Anderson, 1988 quoted in Cox et al., 1997, p. 3) have indicated that a good temporal resolution can be achieved with 500 time steps per shedding cycle. In their CFD study on 2D flow around a circular cylinder, Cox et al. (1997) used between 300 and 600 time steps per cycle and they maintain that further time refinement resulted in no appreciable changes of the results.

#### 2.4.2.4 Turbulence and transition modelling

As has been mentioned in section 2.4.1, transition plays an important role on the flow over a circular cylinder. In section 2.2.5.2.2, several aspects of transition modelling have been addressed. The conclusion that relative simple models can capture the transition effects has been derived based on the assumption that it takes place in a narrow area of the flow.

For the flow over a cylinder, this assumption does not hold below the supercritical regime and Reynolds numbers above 200. For such cases, Cox et al. (1997) suggest that only DNS can capture the important effects of transition. Similarly, Liaw (2005) suggests using LES to simulate the flow at a Reynolds number of $1 \cdot 10^4$.

For Reynolds numbers at and above the supercritical regime, Cox et al (1997) hold the view that RANS approach in conjunction with turbulence and transition model can simulate the important effects of turbulence. However, the use of an accurate transition model is highlighted as the only way to predict important flow features particularly for the cases where it occurs on or near the body.

With regard to the turbulence models used to simulate the flow over a circular cylinder, several studies (Majundar et al., 1985, Franke et al., 1990, quoted in Liaw, 2005, p. 37-38) have tested k-ε for subcritical Reynolds numbers. Cox et al. (1997) used k-ε for both supercritical and subcritical regimes, as well as Spalart-Allmaras and SST k-ω.

### 2.4.2.5 Results

The use of k-ε for subcritical regimes (Majundar et al., 1985, Franke et al. 1990, quoted in Liaw, 2005, p.37-38) has led to the conclusion that the model is not capable of representing the flow accurately. Neither the drag coefficient nor the point of separation have shown agreement with experimental data.

Liaw (2005) obtained drag values in disagreement with experimental data using SST k- ω turbulence model for a Reynolds number of $1 \cdot 10^4$. Contrarily, the use of LES led to a significant improvement of results. Liaw (2005) also proved that the lower order advection scheme produced pressure coefficient values more negative than the experimental ones for angles between 60 and 110 degrees at Reynolds numbers of $1 \cdot 10^3$ and $1 \cdot 10^4$ (see section E.4.2 for angle reference).

For a Reynolds number of $9 \cdot 10^4$, close to the critical regime, Cox et al. (1997) obtained large differences between the drag derived from experiments and the one obtained from the three low Reynolds number turbulence models S-A, k-ε and SST k-ω. However, all of them exhibited “an early drag crisis consistent with experiments for increased free stream turbulence” (Cox et al., 1997, p. 5). Contrarily, for the Reynolds $5 \cdot 10^6$ all the models gave similar results in agreement with experimental data.

All the computations by Cox et al. (1997) led to Strouhal values higher than experimental results but both presented a similar trend. For the specific case of $9 \cdot 10^4$ Reynolds number, the use of wall functions led to Strouhal values similar to those found at supercritical regime in which the boundary layer is fully turbulent. With respect to the lift, the calculations by Cox et al. (1997) found agreement with experimental observation in that “higher levels of turbulence yield lower lift amplitudes” (Cox et al., 1997, p.5).

With regard to the laminar regime, Cox et al. (1997) found good agreement between the results obtained from the simulations at a Reynolds number of 100 and the experimental data. They highlight the fact that, in this regime, the flow is deemed to be two-dimensional.

## 2.4.3 Cylinder arrays

The studies by Constantinides et al. (2011) and Atluri et al. (2006) have modelled the flow through the complex array of cylinders on the truss section of a truss spar (Figure 2-14 (c)) using CFD.

### 2.4.3.1 Mesh

Both studies prioritized the use of wall functions and made use primarily of tetrahedral elements outside the boundary layer region where wedge elements were used. As can be appreciated from Figure 2-18 (b), Constantinides et al. (2011) employed wedge elements also in the outer domain region.

Constantinides et al. (2011) used a cylindrical mesh domain (Figure 2-18 (b)) with the aim of performing simulations with different directions of current without the necessity to change the domain for each particular case. Moreover, for the same reason they kept the refinement levels around the truss elements very high. Contrarily, Atluri et al. (2006) used a rectangular domain to simulate only one current direction (Figure 2-18 (a)).

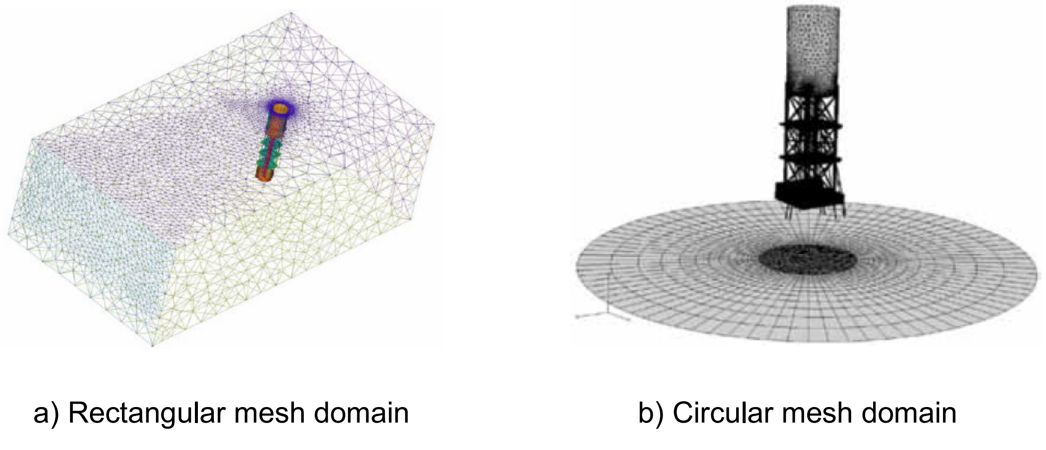

a) Rectangular mesh domain

b) Circular mesh domain

**Figure 2-18 – Computational domains. Source: Atluri et al. (2006) (a); Constantinides et al. (2011) (b)**

### 2.4.3.2 Turbulence model

Both studies made use of the DES (Detached eddy Simulation) technique. It consists of a "hybrid model that combines the accuracy and economy of Spalart-Allmaras (S-A) model for attached boundary layers with the accuracy of LES for separated eddies" (Atluri et al., 2006, p. 3).

### 2.4.3.3 Simplifications

In their study, Constantinides et al. (2011) state that the boundary layer of both the tanks above and below the truss structure was not modelled in an attempt to reduce the problem size.

Atluri et al. (2006), in order to economize the mesh, did not model the truss section of the spar explicitly but used Morison equation to estimate the truss forces.

### 2.4.3.4 Results

The velocity contours around the cylinder array at a plane section for different current directions obtained by Constantinides et al. (2011) are shown in Figure 2-19. The effect of the current direction can be clearly appreciated.

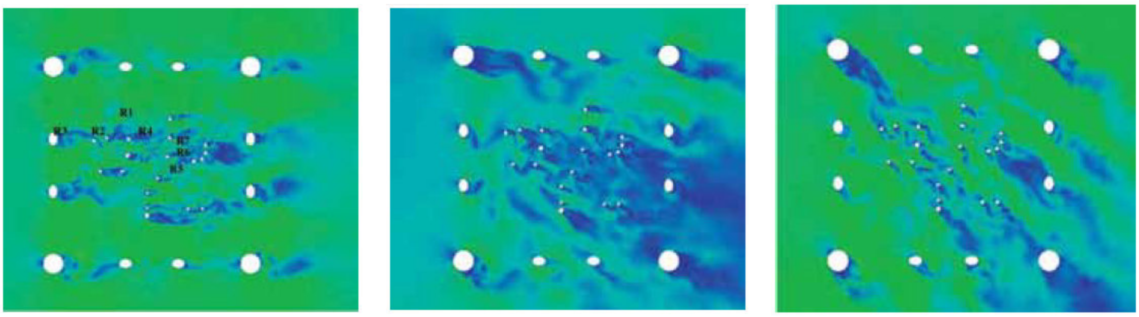

a) 0 degrees

b) 25 degrees

c) 45 degrees

**Figure 2-19 – Velocity contours for different flow directions. Source: Constantinides et al. (2011)**

# 3 CFD SIMULATIONS

## 3.1 PONTOONS

### 3.1.1 Towing tank tests

In order to validate the numerical drag predictions obtained from CFD, several towing tank tests have been performed on the PLAT-O pontoons at the Cranfield University Ocean Systems Test Laboratory. A representation of the experimental set up has been shown in Figure 3-1 (a).

From previous testing campaigns, the laboratory disposed of a metallic cylindrical beam conceived specifically as support structure for turbines. The time and budgetary constraints of the present study have precluded building a new streamlined carbon fibre test rig for the pontoon and the already existing mast has been used. In order to connect both bodies, the interface represented in Figure C-1 has been designed.

To ensure that the pontoon was positioned with zero angle of attack, the distance from a reference point to the extremes of the body was measured as schematically represented in Figure 3-1 (b). The pressure exerted by the jubilee clips used to link the interface and the pontoons was adjusted so that both measurements were the same.

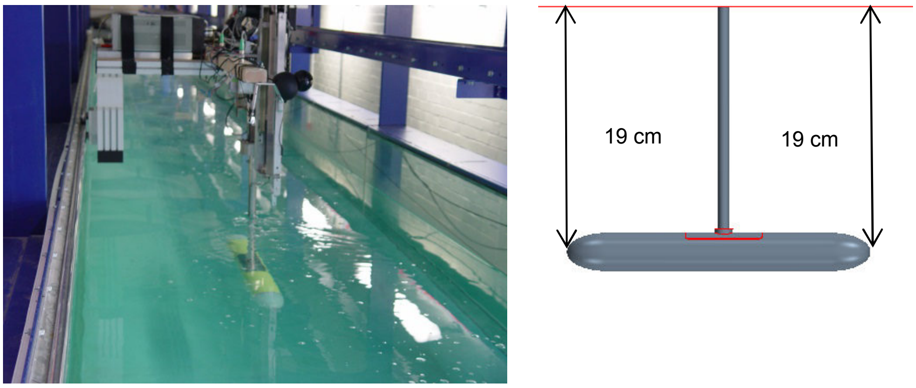

a) Experimental set up

b) Alignment checking

**Figure 3-1 – Experiments on the PLAT-O pontoon**

A procedure is required to eliminate the additional source of drag caused by the support structure and interface. It consists of performing two distinct tests: one with the pontoon installed and another one with only the support structure. Eventually the drag values of the second tests are subtracted from the initial ones and the drag of the pontoon is obtained.

Because of some VIV (vortex induced vibration) issues encountered during the tests with the support structure and plate, which can be observed as a characteristic eight pattern in Figure 3-2 (b), another set of measurements was undertaken only with the cylindrical support structure in an attempt to smooth them. Although the oscillations were reduced, they were still too high for a save operation of the carriage at velocities higher than 1.7 m/s. The three data sets obtained have been represented in Figure 3-2 (a).

Because of the fact that the drag values of the support structure are much higher than the pontoon's, any attempt to subtract them from the whole configuration drag has led to inconsistent results regarding the pontoon's resistance as can be derived from the proximity of the curves in Figure 3-2 (a).

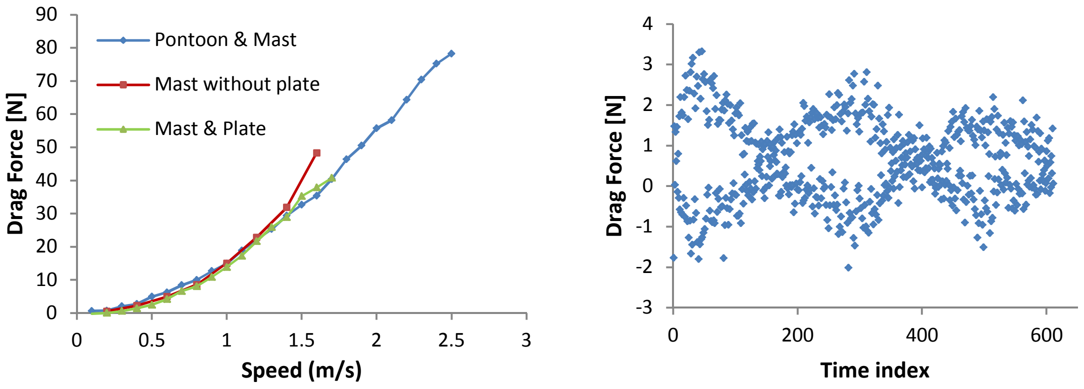

a) Drag experimental data

b) Drag force for 0.3 m/s (beam & plate)

**Figure 3-2 – Experimental drag force values**

### 3.1.2 Model description

The PLAT-O prototype pontoons (Figure 2-11) are composed of a centre cylindrical body and of a 2:1 elliptical bow and aft. As the body is symmetrical, the former will refer to the front part of the pontoon where the flow is coming from and the latter the opposite edge. The detailed dimensions of the geometry are represented in Figure 3-3 (b).

a) CAD model b) Dimensions (mm)

**Figure 3-3 – Geometry of PLAT-O pontoons**

The PLAT-O tag lines are linked to both ends of the pontoons by means of a metallic piece a detail of which is represented in Figure 3-4 (a). The pontoons are connected to PLAT-O space frame by means of jubilee clips[4] as represented in Figure 3-4 (b). None of the geometrical features mentioned above has been included in the CAD geometry used in the CFD simulations as can be derived from comparing Figure 3-3 and Figure 3-4.

a) Pontoon/Tag line connection detail b) Jubilee clips around pontoon body

**Figure 3-4 – PLAT-O prototype geometry details**

### 3.1.3 Mesh

The trimmer module of Star CCM+ has been used to generate the grid as the pontoon geometry is rather simple (section 2.2.3).

---

[4] The fittings of the PLAT-O prototype are not optimum as their choice was driven by the necessity to start an experimental campaign to secure funding from several investors which involved building the model in a very tight time frame.

### 3.1.3.1 Domain boundaries

The domain boundaries have been positioned far enough from the pontoon in order to represent an open sea condition. The sensitivity of the location of the outlet boundary to the computed value of the drag has been analysed leading to the results shown in Figure 3-5. From the graph it can be derived that the drag variation with respect to the wake size is very small.

The simulations have taken advantage of the symmetry of the pontoon as can be appreciated in Figure D-1.

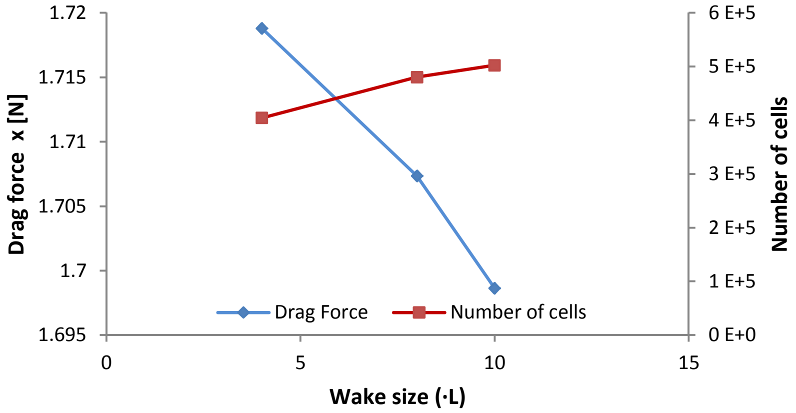

Figure 3-5 – Outlet boundary sensitivity

### 3.1.3.2 Near wall region

Two different meshes have been generated to accommodate both the use of wall functions and the SST k-ω low Reynolds turbulence model. The distance of the nodes closer to the pontoon surface has been appropriately tuned to achieve values of y+ in agreement with the recommendations explained in section 2.2.5.2.1. A summary of the two near wall treatment approaches used has been represented in Figure 3-6.

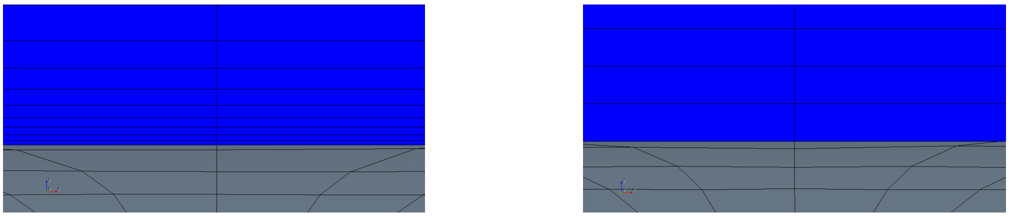

a1) Grid for SST k-ω use

b1) Grid for standard k-ε use

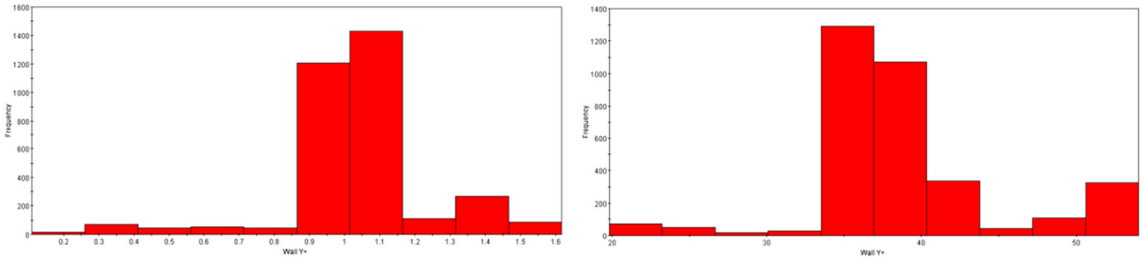

a2) y+ distribution SST k-ω

b2) y+ distribution standard k-ε

**Figure 3-6 – y+ distribution comparison between near-wall treatments**

From Figure 3-6 (a2) and (b2) it can be appreciated that the y+ values are within the recommended ranges. However, for a good boundary layer resolution it is necessary to ensure that enough number of points is placed within it (section 2.2.5.2.1).

A closer inspection of the wall function approach mesh revealed that it contained a maximum of 6 nodes inside the boundary layer. The recommended guidelines suggest that the mesh should have between 8-10 points inside it. Because of that, the mesh was tuned again to satisfy the requirements. In order to achieve it, the y+ values were reduced to allow for a higher clustering of cells next to the wall. This fact is in agreement with the ERCOFTAC (2000) recommendation of having y+ values close to 20 for boundary layers with Reynolds number lower than $10^5$ (section 2.2.5.2.1.1). The new resolution contained a maximum of 10 points which is considered acceptable. Figure 3-7 shows a plot of the new y+ values distribution.

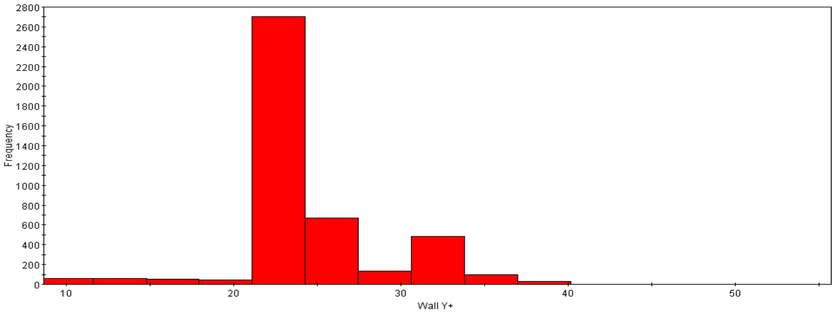

**Figure 3-7 – Grid y+ distribution for wall functions use**

It has to be underlined that the number of nodes inside the boundary layer mentioned above corresponds to the thicker parts of it. Therefore, it means that the regions where the boundary layer develops contain fewer nodes and may not be represented accurately enough.

With respect to the low Reynolds number approach, an inspection of the boundary layer revealed that a maximum of 33 points were placed inside it. This value is in accordance with the recommended guidelines. However, similarly to the case explained above, for regions where the boundary layer is much thinner the resolution is reduced to 10 points. The constraints imposed by the software parameters have not enabled a further improvement of the results.

### 3.1.3.3 Mesh refinement

A higher density of nodes has been placed at regions with higher flow gradients such as the wake and a smooth transition to the coarsest parts of the mesh has been established. The Star CCM+ mesh tool *volumetric controls* has been used in order to have a better command on the size of the cells at important regions of the flow. Figure D-2 shows a view of the grid.

The size of the pontoon surface elements has been tuned to guarantee a good representation of the geometry. Figure 3-8 shows a comparison of coarse and fine resolutions for surface mesh (the bold black line represents the original geometry).

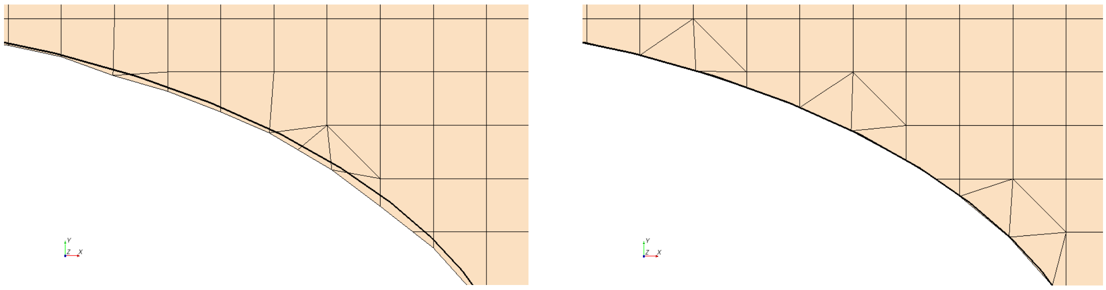

a) Poor surface resolution

b) Adequate surface resolution

Figure 3-8 – Surface mesh resolution comparison

#### 3.1.3.4 Verification

A mesh independence study for both meshes has been performed. The results have been represented in Figure D-3 and, similarly to the outlet boundary sensitivity, there is little variation of the drag with respect to the mesh size. The second finest mesh has been used for the calculations.

It can be appreciated from Figure D-3 that the number of elements in k-ε mesh is much lower than for SST k-ω. The reason is that a mesh of 10L wake size was used for SST k-ω and, after the boundary sensitivity analysis, a 7L mesh size was employed for k-ε simulations.

### 3.1.4 Boundary conditions

The top of the flow domain which represents the free surface has been assigned a symmetry condition.

With respect to the turbulence model boundary conditions, both a turbulence intensity and a turbulence length scale have been specified at the inlet and outlet boundaries. The latter has been established as a 5% of the diameter of the pontoon as suggested by the Star CCM+ user-guide (2013). The former has been assigned a value of 1% to represent the low value of turbulence intensity present in the towing tank.

This fact may seem in contradiction with the setting of the boundaries at a location far enough the body to simulate open water conditions. The aim of using low values of turbulence intensity is to allow the possibility to compare the results of this study with a potential further study investigating the tank blockage effects without the uncertainty of using different values of turbulence intensity for the tank and open water conditions.

### 3.1.5 Features of the simulation

The fluid flow has been modelled with the incompressible, viscid, isothermal and steady Reynolds-Averaged Navier-Stokes equations. The Star CCM+ properties of water by default have been used.

The simulation has been performed with a Gauss-Seidel iterative algorithm, a second order upwind interpolation scheme and the SIMPLE pressure-velocity coupling. Both SST k-ω and k-ε turbulence models have been used.

The simulations have been performed for different current velocities in order to obtain the characteristic drag curve of the pontoons.

### 3.1.6 Results and discussion

#### 3.1.6.1 Convergence

Both the residuals and the drag force have been monitored to ensure that a converged solution was achieved. As can be appreciated in Figure D-4, the residuals fall below the threshold of 0.001 and no changes can be observed in the drag force with respect to the number of iterations. Therefore, the solution is deemed to be converged. The plots of Figure D-4 correspond to a current speed of 1 m/s and the SST k-ω turbulence model. However, for the rest of speeds simulated and turbulence model the trends obtained have been the same.

#### 3.1.6.2 Drag calculations

The results obtained regarding the drag force at different current speeds have been represented in Figure 3-9.

A significant difference between the CFD results and the empirical calculations can be observed. The latter should not be regarded as reliable validation data as can be derived from the study by Alvarez et al. (2009) mentioned in section 2.3.4. It states that, for cases where the flow separation is important, the drag calculations using ITTC 57 curve lead to inaccurate results.

A high correlation between the skin friction drag calculated using k-ε turbulence model and the estimation using ITTC 57 curve can be appreciated. The reason is thought to be the coincidence of hypothesis used to derive both the wall functions and the ITTC 57 skin friction curve (sections 2.2.5.2.1 and Appendix A). The k-ε turbulence model with wall functions represents exactly the same type of boundary layer structure found in the experiments used to derive ITTC

57. Such a high level of correlation is in agreement with the results obtained by Phillips et al. (2007) from the CFD simulations on Autosub AUV (section 2.3.5).

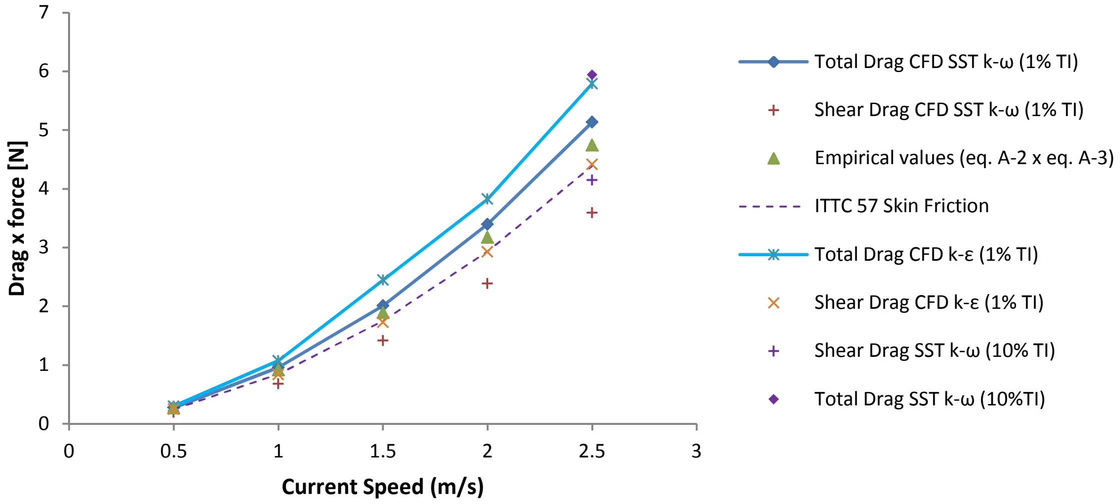

**Figure 3-9 – CFD drag calculations on the pontoons**

Notwithstanding, a significant difference between the total drag calculated using k-ε and SST k-ω turbulence models can be appreciated. For instance, the discrepancy at a current speed of 2.5 m/s is of 12.8%. This result is in disagreement with the high level of correlation obtained by Phillips et al. (2007) between the drag values computed with k-ε and SST k-ω. Several hypotheses have been investigated in order to address the cause of the difference.

### 3.1.6.3 Effect of turbulence modelling

One of the sources of discrepancy could be related to the geometrical differences between the cases analysed in this study and in the simulation by Phillips et al. (2007).

As can be appreciated from the comparison of PLAT-O pontoons (Figure 2-11 (a)) and Autosub (Figure 2-11 (b)), the aft curvature of the former is much higher than the latter therefore leading to higher adverse pressure gradients. Because of that, the amount of separation in PLAT-O pontoons is expected to be more important.

From the velocity contours of Figure 3-10 and Figure 2-13 it can be appreciated that, effectively, the wake region of Autosub is restricted to a very narrow part at the end of the aft whereas in PLAT-O the separated region is wider.

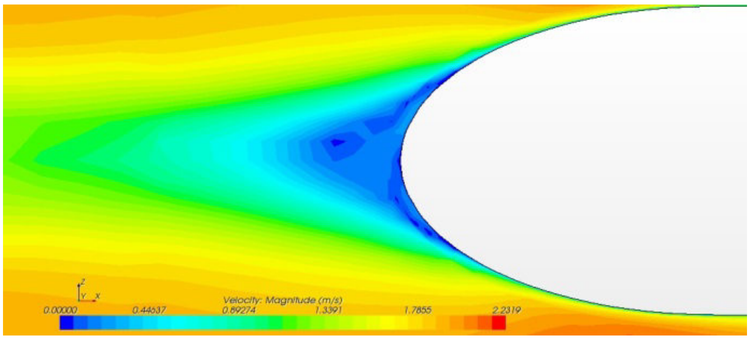

a) k-ε turbulence model

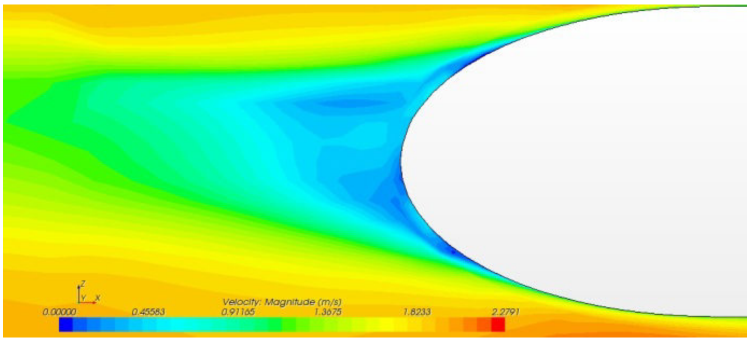

b) SST k-ω turbulence model

**Figure 3-10 – Detail of the velocity contours in the wake**

In section 2.2.5.1.1, it has been explained that k-ε is less capable of accurately representing separation than SST k-ω. Moreover, it has been mentioned that the flow tends to be more separated than k-ε model predicts. The results obtained are in agreement with these statements.

It can be appreciated from Figure 3-11 that the distribution of pressure coefficient derived from the use of k-ε and k-ω is highly correlated on the majority of the length of the pontoons except at the end of the aft. In this region there is a change on the trend of $C_p$ due to separation which can be appreciated as a flat succession of points.

The flat region of dashed lines (SST K-ω) occurs before the dotted (k-ε) meaning that the flow is more separated or separates before when the SST k-ω model is used. This feature can also be observed by comparing the wake of the pontoon represented in Figure 3-10. This leads to the fact that higher values of pressure drag are obtained when SST k-ω is used as can be appreciated in Figure 3-12.

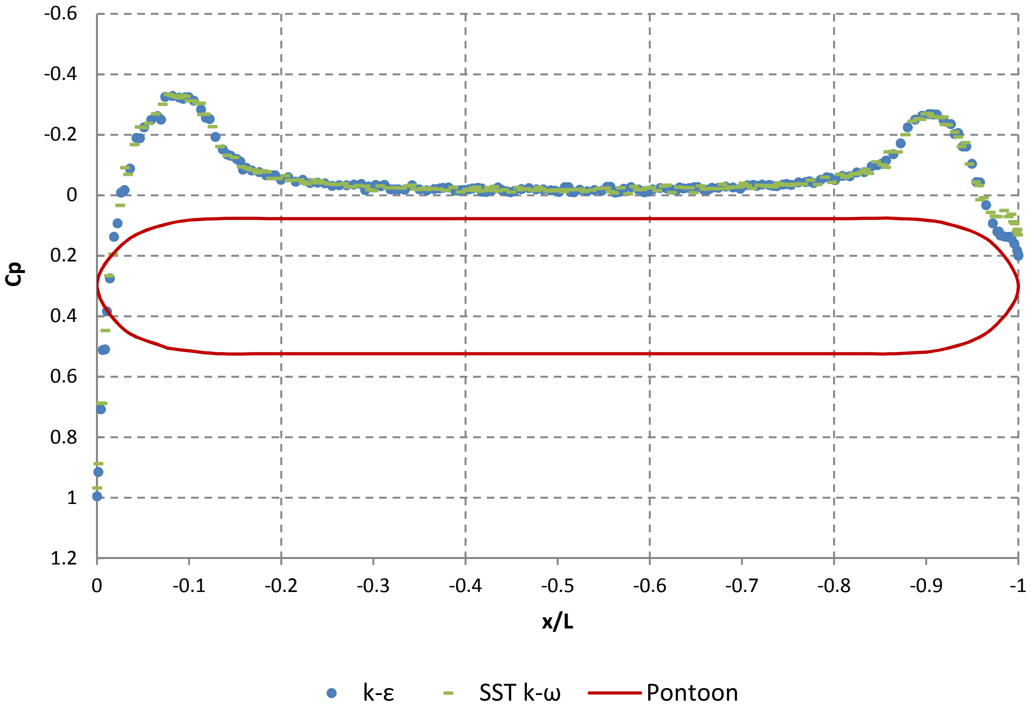

**Figure 3-11 – Pressure coefficient distribution**

Therefore, it could be hypothesized that the source of difference is a higher importance of separation at the pontoons aft than in Autosub UAV which is not equally modelled by k-ε and SST k-ω.

However, if analysed numerically, the difference between the pressure drag obtained with SST k-ω and k-ε at 2.5 m/s is 0.163 N whereas the difference of total drag is 0.658 N. From these values it can be derived that the highest contribution to the total difference is due to the skin friction drag and not to the pressure drag.

The differences between the skin friction drag obtained from SST k-ω and k-ε cannot be attributed to the geometry of the pontoon because the separated region of the aft is very small in comparison to the total length of the pontoon. Therefore, the hypothesis that the source of discrepancy with Phillips et al. (2007) comes from the geometry differences between pontoons and Autosub cannot be accepted.

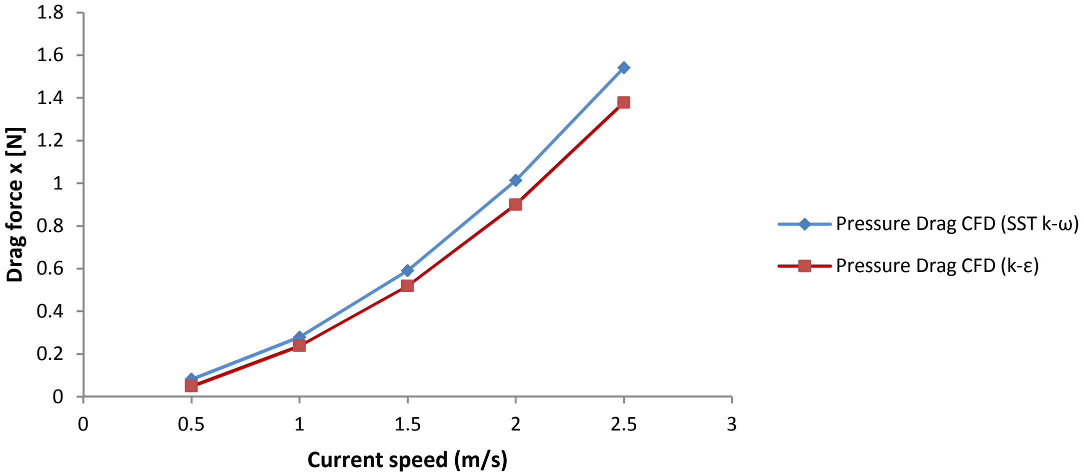

**Figure 3-12 – Pressure drag comparison beetween SST k-ω and k-ε**

### 3.1.6.4 Effect of boundary conditions

The differences in the boundary layer modelling between k-ε and k-ω are expected to be the cause of inconsistency of results. As has been explained in section 2.2.5.2.1, wall functions are derived based on turbulent boundary layer data. Turbulent velocity profiles generate higher shear stresses on the surface than a laminar as has been explained in section 2.1. The fact that SST gives lower values of shear drag than k-ε suggests that the former predicts velocity profiles in the shear layer more representative of laminar than turbulent boundary layer.

The study of Stevenson et al. (2009) mentioned in section 2.3.1 referred to AUV with bulbous hull shapes which maintained laminar flow in the majority of body length. The PLAT-O pontoons have a similar form and therefore it could be possible that the results from SST k-ω corresponded to a laminar boundary layer.

In order to verify the hypothesis, a simulation with higher turbulence intensity has been performed. As has been mentioned in section 2.2.5.2.2, the capabilities of SST k-ω to predict transition are limited to the effect of free-stream turbulence. Thus, applying higher levels of turbulence intensity can provoke transition to a turbulent boundary layer.

Effectively, as can be appreciated in Figure 3-9, the value of shear drag from SST k-ω with a turbulence intensity of 10% at 2.5 m/s has increased and is closer to both ITTC 57 and k-ε. Moreover, the total drag difference has been reduced from 12.8% to a 2.5%. Therefore, it can be concluded that the simulations of Phillips et al. (2007), which did not specify the level of turbulence intensity, were performed with values of free-stream turbulence higher than the ones of the present study.

The transition prediction capabilities of SST k-ω may not be suitable to accurately represent the flow around streamlined body shapes in which laminar boundary layers extend to a certain proportion of body length. The sensitivity of the simulations to free stream turbulence in the PLAT-O pontoon geometry is a good example. Therefore, if an accurate description was intended, extra transition models such as Gamma ReTheta mentioned in section 2.2.5.2.2 should be used in conjunction with SST k-ω.

However, the geometry of the pontoons has been simplified as explained in section 2.3.1. In real operating conditions, the metallic piece in the bow would disturb the flow and force a turbulent boundary layer at the whole length of the pontoons. Because of that, the drag value obtained experimentally would be probably closer to the one obtained with k-ε turbulence model with wall functions or with the SST k-ω with 10% turbulence.

Because of the mesh savings of the wall functions approach it would be more desirable to use k-ε. Even if it does not model the separation accurately, it has been observed that the difference of pressure drag predicted with k-ε and SST k-ω is very small.

### 3.1.6.5 Velocity contours and pressure coefficient

Both the velocity contours around the pontoons (Figure 3-13) and the distribution of pressure coefficient (Figure 3-11) present the same trend as the results obtained by Phillips et al. (2007) commented in section 2.3.5 (Figure 2-13).

With respect to the velocity contours, four main features can be appreciated. In the bow of the pontoons, the flow stagnates leading to a region of low velocities and then accelerates locally until reaching the mid-body. Over the length of the pontoon, the boundary layer grows gradually and generates an effect of constrainment to the outer flow. Because of that, it accelerates locally at the beginning of the elliptical aft. Due to the adverse pressure gradients in it, the flow detaches and large vertical structures are formed in the wake.

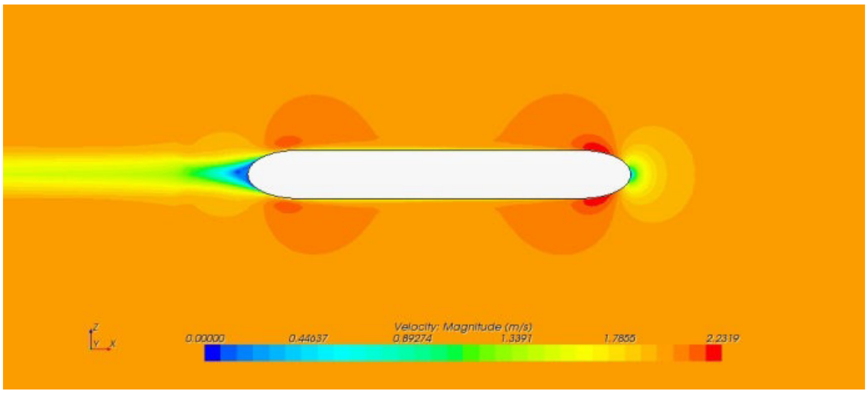

a) Standard k-ε turbulence model

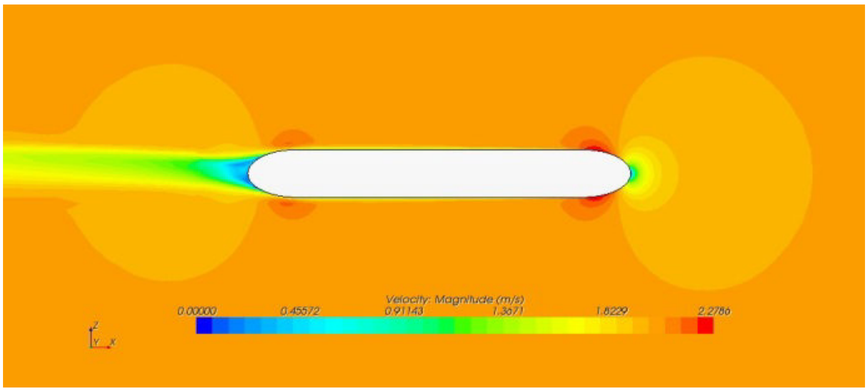

b) SST k-ω turbulence model

**Figure 3-13 – Detail of the velocity contours around the pontoon**

From the comparisons of Figure 3-13 (a) and (b) some differences between the velocity contours obtained can be observed.

Primarily, wider regions of accelerated flow are observed in Figure 3-13 (a). The reason is expected to be that a higher rate of growth of the boundary layer is predicted by k-ε in comparison with SST k-ω.

Another significant difference is the asymmetry of the wake observed in Figure 3-13 (b) compared to (a). The cause of this flow feature is thought to be some degree of unsteadiness in the separated region. The residual plots of Figure D-4 (a) start oscillating slightly when they stop decreasing and suggest that some unsteady phenomenon could be occurring. The difference can be further observed in the detailed velocity contours of the wake shown in Figure 3-10.

The flow features explained above can be interpreted alternatively using the pressure coefficient plot. As can be appreciated from the comparison of Figure 3-11 and Figure 2-13 (b), the trend of the pressure coefficient distributions around PLAT-O pontoon and Autosub AUV present a lot of similarities.

From a first general inspection, two peaks of negative pressure coefficient can be observed which correspond to the local accelerations of the flow. From the stagnation point at x/L=0 until x/L~0.6 the correlation of results between this study and Phillips et al. (2007) is high. One of the main reasons is the fact that both PLAT-O pontoon and Autosub have a 2:1 elliptical bow. However, from x/L~0.6 until x/L=1 the peak value of $C_p$ in PLAT-O pontoon occurs at a higher ratio of x/L than in Autosub and presents more negative values.

The length of the mid-body in the PLAT-O pontoons is higher and, therefore, the boundary layer has more space to grow and to create higher flow constrainment to the free-stream current. This is the reason why the $C_p$ distribution of the pontoon reaches more negative values and at a x/L ratio higher than in Autosub.

Eventually, another interesting feature is the difference of the rate at which $C_p$ reaches positive values after the negative peak at the aft. In Autosub the recuperation is slow in comparison with the pontoons where the trend is much steeper. Obviously, it is related to the decrease of velocity at the aft which is slower for Autosub due to its cone shape with smaller adverse pressure gradients.

### 3.1.7 Conclusions

A detailed CFD analysis of the flow around PLAT-O pontoon has been carried out. The drag has been calculated at different current speeds and good agreement has been found with the trends observed in previous studies focused on AUV’s. The problems experienced in obtaining the drag of the pontoon experimentally have precluded the validation of the results.

Both standard k-ε and SST k-ω turbulence models have been proven to yield similar results for high enough levels of free-stream turbulence. This enables to take advantage of the lower mesh sizes associated with the use of wall functions.

A high level of correlation between the skin friction drag predicted by CFD and ITTC 57 curve has been observed. In addition, the separation of the total resistance into pressure and shear drag has highlighted the importance of the latter. In view of these statements, the ITTC 57 curve in conjunction with form factors could be incorporated to the parametric design elaborated by SME to improve the initial estimates of the drag.

The difficulties experienced to achieve an adequate boundary layer resolution deserve special attention and should be investigated in future work. In addition, simulations on the experimental set up geometry on the towing tank should be performed to validate the code. A comparison with the results of the present study could provide an insight into the constrainment effects of the tank walls.

## 3.2 CIRCULAR CYLINDERS

The simulations have been performed on a two-dimensional circular cylinder of 0.04 meters diameter.

### 3.2.1 Mesh

The polyhedral mesh model of STAR CCM+ (section 2.2.3.2) has been used to generate the grid. Apart from having some advantages with respect to other meshing strategies, it has been employed to test its performance and to practice on a relatively small problem size.

#### 3.2.1.1 Domain boundaries

Following the recommendations by Rumsey et al. (1987, quoted in Cox et al., 1997, p. 3) explained in section 2.4.2.2, the outlet boundary has been placed at a distance from the cylinder equal to twenty times its diameter.

With respect to the inlet and lateral boundaries, they have been positioned five diameters far from the cylinder following Mittal et al. (1995) study conclusions.

A schematic of the boundaries can be appreciated in Figure E-1.

#### 3.2.1.2 Near wall region

Similarly to the pontoons' CFD simulation, two different meshes have been generated to accommodate the k-ε and SST k-ω turbulence models. In addition, a third mesh has been created to obtain a laminar solution.

With respect to the turbulent cases, both the wall y+ distance and the boundary layer resolution have been addressed. The former has been tuned in accordance with the guidelines (section 2.2.5.2). Figure 3-14 shows a comparison of both near-wall treatments.

As can be appreciated in Figure 3-14 (b), the stretching in the near wall clustering of cells is almost non-existent. This fact underlines the difficulties to place enough number of nodes inside the boundary layer and, at the same time, maintain a gradual increase of size until merging with the outer domain. In contrast with the mesh for the use of wall functions, a stretched near-wall full grid can be observed in Figure 3-14 (a).

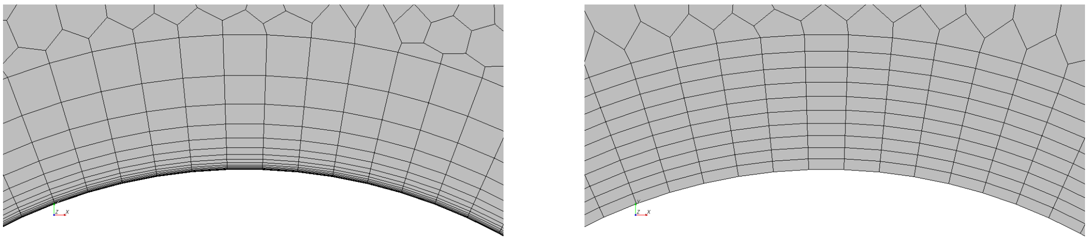

a) Full grid

b) Grid for use of wall functions

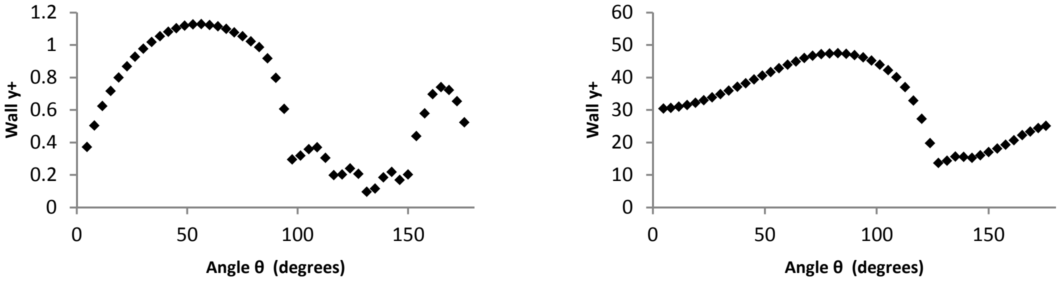

c) SST k-ω mesh y+ distribution

d) k-ε mesh y+ distribution

**Figure 3-14 – 2D cylinder near-wall region**

A closer inspection of the near wall region has revealed that a maximum of 10 points have been included in the thicker parts of the boundary layer at the wall functions approach mesh. However, with regard to the low Reynolds number grid near-wall region, only 15 have been found to fall inside the shear layer. Therefore, the number of cells clustered to the wall has been increased from the initial 15 to 35, leading to a resolution of up to 33 points inside it in agreement with guidelines (section 2.2.5.2.1). Figure 3-15 shows a comparison between the two different boundary layer resolutions.

For both cases the developing regions of the boundary layer have been found to contain fewer nodes than the recommended and therefore may not be accurately represented.

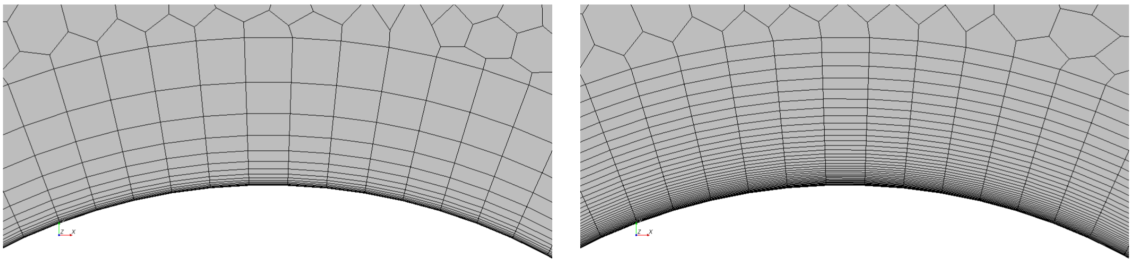

a) Low resolution

b) Higher resolution

**Figure 3-15 – Different mesh resolutions for the use of SST k-ω**

With respect to the laminar flow simulation, in this case obviously there is no turbulence model applied and the value of wall y+ distance is not worth monitoring. However, an adequate clustering of cells near the wall is still important to solve the high velocity gradients in the boundary layer. Following Star CCM+ user-guide (2013) recommendation, 15 prism layers have been allocated close to the wall.

### 3.2.1.3 Mesh refinement

Because of some difficulties experienced with local refinement for two-dimensional meshes and the polyhedral module, no specific size has been assigned to the wake region of the cylinder. Instead, a general small size of cells has been applied to the whole domain by using the refinement control parameters available in polyhedral Star CCM+ module. Figure 3-16 shows a comparison of mesh densities.

It can be appreciated that the transition from the smaller cell size in the boundary layer to the outer domain is not smooth enough for the mesh in Figure 3-16 (a). Contrarily, a better transition is achieved at the mesh in (b). The difference has been obtained by changing the growth factor rate parameter in Star CCM+ mesher module.

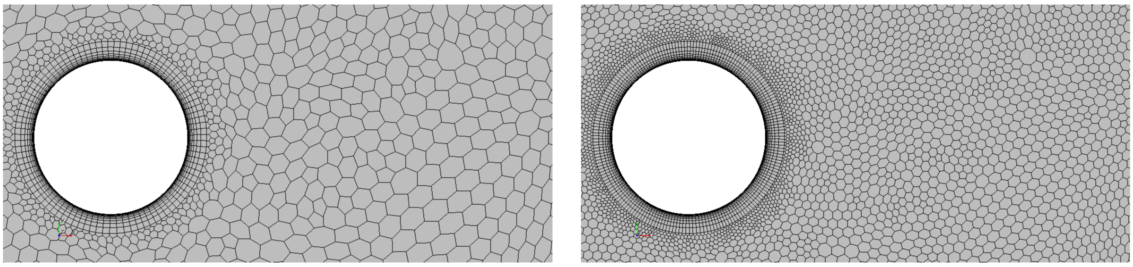

a) Coarse stretching b) Smooth stretching

**Figure 3-16 – Circular cylinder mesh detail**

### 3.2.2 Verification

Several sensitivity studies have been performed to assess the influence of the grid size, time step and turbulence intensity levels on the final results. The plots in Figure E-2, Figure E-3 and Figure E-4 summarize the information obtained.

With respect to the mesh size, the difference of drag and Strouhal number between the two finest meshes has been found to be around 3.5%. Therefore, it suggests that mesh independence has been achieved.

With regard to the time step, no effect has been found on the results when using 100, 200 or 500 time steps per vortex shedding cycle.

The greatest source of influence to the results has been found to be the free stream turbulence intensity levels. As can be appreciated in Figure E-5, the lift amplitude is higher for higher levels of free stream turbulence in agreement with the statement by Cox et al. (1997) mentioned in section 2.4.2.5.

### 3.2.3 Features of the simulation

The fluid flow has been modelled with the incompressible, viscid, isothermal and unsteady Reynolds-Averaged Navier-Stokes equations. The Star CCM+ properties of water by default have been used. The simulation has been performed with a Gauss-Seidel iterative algorithm, a second-order upwind interpolation scheme and the SIMPLE pressure-velocity coupling. Both SST k-ω and k-ε turbulence models have been used.

Several simulations have been performed at different Reynolds numbers (100, $9 \cdot 10^4$ and $5 \cdot 10^6$).

### 3.2.4 Results and discussion

#### 3.2.4.1 Convergence

Both the residuals and the lift and drag coefficients have been monitored to ensure that a converged solution was obtained. Figure E-6 (a) represents the whole history of residuals. The detailed plot in Figure E-6 (b) enables to distinguish their reduction with each time step. They all fall below the threshold of 0.001.

In comparison with a steady simulation, in a transient case the solution is deemed to be converged when the oscillation of the monitored quantities reaches a stable state. From Figure E-7 it can be appreciated that the lift and drag fluctuations are stable. Moreover, it can be appreciated that the drag frequency is two times higher than the lift in accordance with the explanation in section 2.4.1.

From both the residual plot and the monitored engineering quantities the conclusion that a converged solution has been achieved can be derived. The plots correspond to the specific case of a Reynolds number of $9 \cdot 10^4$ but for the rest of the cases they followed a similar trend.

#### 3.2.4.2 Drag and Strouhal number

The results obtained for both drag and Strouhal have been contrasted with the computations by Cox et al. (1997) on the same range of Reynolds numbers as can be appreciated in Figure 3-17.

Although the lift has not been mentioned directly, it has been implicitly used to derive the frequency of the vortex shedding and, therefore, the Strouhal number.

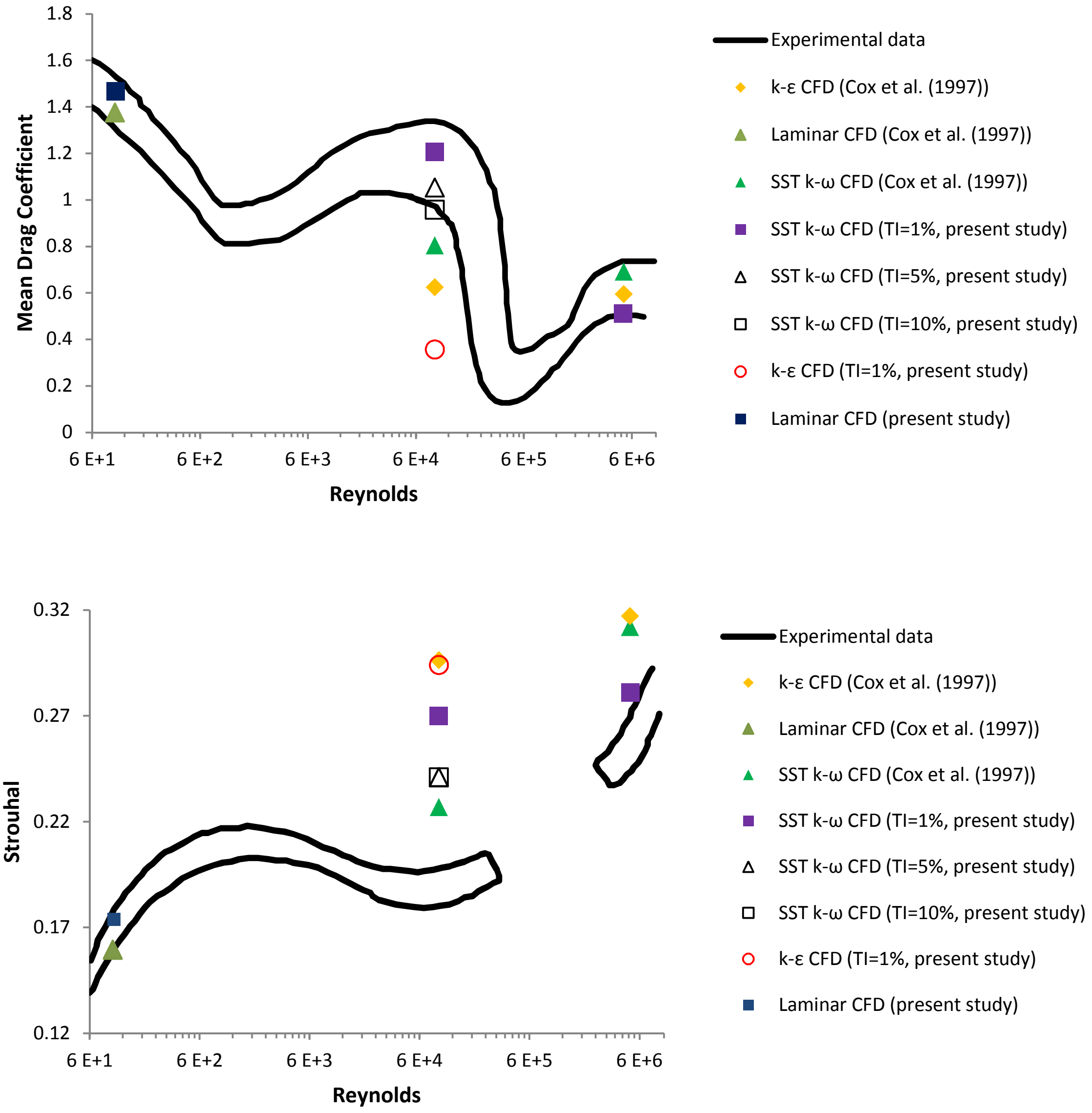

**Figure 3-17 – Comparison of results against experimental data**

With respect to the laminar region, for a Reynolds number of 100 the CFD simulation results have fallen within the range of experimental data for both drag and Strouhal. The high level of correlation between two dimensional CFD simulation results with experimental data is in agreement with the statement by Cox et al. (1997) that at this region the flow is deemed to be inherently two-dimensional.

With regard to the simulations at a Reynolds number of $9 \cdot 10^4$, in addition to the dispersion of experimental data a wide scatter of computed data can be appreciated. The present study calculations with SST k-ω and 1% turbulence intensity fall within the mean drag experimental data but are in clear disagreement with respect to the Strouhal number. Moreover, the results obtained by Cox et al. (1997) for this particular turbulence model are very far from matching the present work calculations.

The boundary conditions sensitivity analysis has shown that both results become closer when higher levels of turbulence intensity are used. This suggests that the study by Cox et al. (1997), which did not specify the turbulence intensity levels employed, used higher values of it than in the present work.

A massive reduction of the mean drag coefficient and a huge increase in the Strouhal number has been obtained with the use of k-ε turbulence model with wall functions. This trend is in agreement with the results obtained by Cox et al. (1997).

The cause of this behaviour is hypothesised to be related to the modelling of the boundary layer. At a Reynolds number of $9 \cdot 10^4$, below the critical regime, the transition in the boundary layer has not started and, therefore, it is supposed to be laminar. As has been mentioned in section 2.2.5.2.1, wall functions are derived based on turbulent boundary layer flow. As a consequence, when used at a Reynolds number of $9 \cdot 10^4$, the modelled flow resemble those found at higher Reynolds numbers such as $5 \cdot 10^6$ where the boundary layer is fully turbulent.

Although the Strouhal computations of the present study and of Cox et al. (1997) show very good agreement at Reynolds $9 \cdot 10^4$, the difference of mean drag obtained is very high. It has to be taken into account that the standard k-ε model is not capable of accurately predict separation which is of fundamental importance in the flow around a cylinder. Cox et al. (1997) used a modified version of k-ε by Abid (1993, quoted in Cox et al., 1997, p. 2) which may be the cause of the discrepancy of results.

As far as the supercritical region is concerned, at a Reynolds number of $5 \cdot 10^6$ the CFD results of this study concerning the drag calculation fall within the range of experimental data. Moreover, the differences with respect to the work by Cox et al. (1997) have been reduced in comparison with the simulations at Reynolds $9 \cdot 10^4$. The reason for that behaviour is thought to be the fully turbulent characteristic of the boundary layer which decreases the sensitivity of results to the free-stream turbulence levels.

The Strouhal number is slightly higher than the experiments but much lower than the value computed by Cox et al. (1997).

#### 3.2.4.3 Velocity contours

The information of the flow features obtained from the CFD simulations has been summarized in Figure E-8.

A different pattern of the vortex shedding for each Reynolds number can be appreciated in Figure 3-18 (a, c, e). Moreover, from (d) and (f) the delay of the separation point can be clearly observed. The amount of momentum in the boundary layer at the Reynolds number $5 \cdot 10^6$ (f) is higher and, therefore, it is capable of resisting the adverse pressure gradients longer than the one represented in (d).

The different boundary layer velocity profiles between the laminar case (b) and the turbulent (d, f) can be observed.

These results sustain the view of Cox et al. (1997) that the two-dimensional simulations can capture some of the important flow features characteristic of different regimes (section 2.4.2.5).

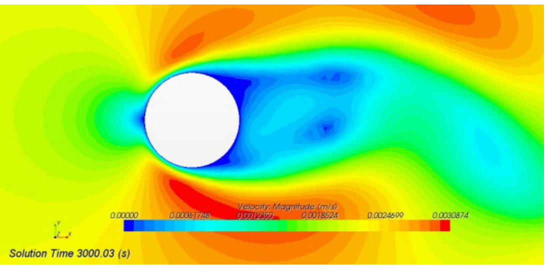

a) Detail velocity contours Re=100

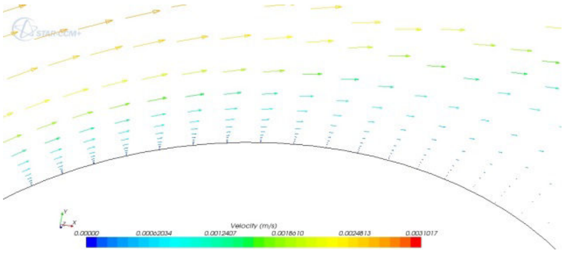

b) Detail boundary layer profile Re=100

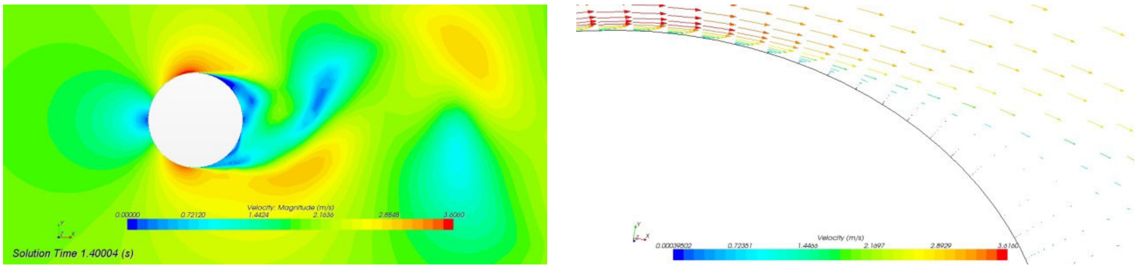

c) Detail velocity contours Re=$9 \cdot 10^4$ d) Detail boundary layer profile Re=$9 \cdot 10^4$

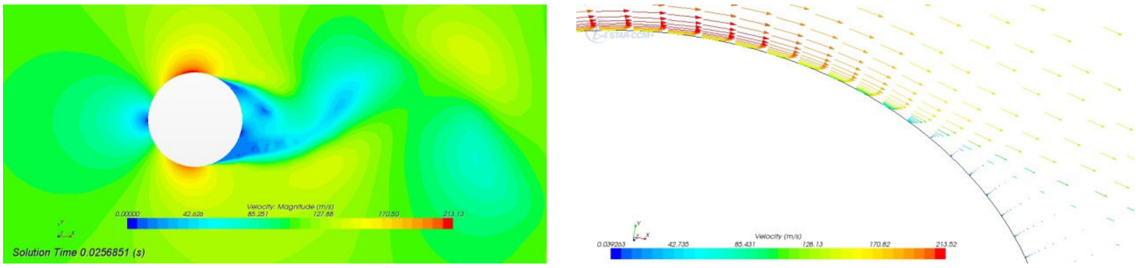

e) Detail velocity contours Re=$5 \cdot 10^6$ f) Detail boundary layer profile Re=$5 \cdot 10^6$

**Figure 3-18 – Detailed views of the flow around a 2D circular cylinder**

### 3.2.4.4 Pressure coefficient

The mean pressure distribution on half of the cylinder surface ($0^o<\theta<180^o$) has been calculated. In addition, it has been contrasted with experimental data as can be appreciated in Figure E-9.

Several common features can be observed from the comparison of the pressure coefficient distributions for the three different Reynolds numbers.

All the plots in Figure E-9 present pressure coefficient values higher than 1 at the stagnation point ($\theta = 0^o$). This result is in accordance with the calculations by Liaw (2005) and the reason is attributed to the influence of the inlet boundary location.

Moreover, all the graphs present higher negative values of $C_p$ than experimental data at the range of angles approximately between 60 and 110 degrees. As has been explained in section 2.4.2.5, Liaw (2005) obtained a similar trend for simulations at Reynolds numbers of $1 \cdot 10^3$ and $1 \cdot 10^4$ but attributed it to the use of a first-order advection scheme. In the present study a second-order upwind scheme has been used and, therefore, it cannot be considered the cause of discrepancy.

The CFD calculations have been based on two-dimensional cases. Thus, the difference of results could be related to the three-dimensional effects which are not captured by the simulations as has been argued in section 2.4.2.1. However, the lower $C_p$ values affect all the Reynolds numbers, even the lowest (Re=100). At this regime the flow is deemed to be two-dimensional.

The fact that even the lowest Reynolds number at the laminar regime presents the feature precludes any attribution of the difference to the effects of boundary conditions such as turbulence intensity.

The cause of the discrepancy of results is hypothesized to be the low boundary layer resolution at the region comprised between the angles 60 and 110. As has been mentioned in section 3.2.1.2, the thicker regions of it contain the recommended number of points. However, in the areas were the boundary layer is still developing the resolution may be very low. From Figure E-9 (b) the change of the pressure distribution with respect to the boundary layer resolution can be observed.

Finally, it can be appreciated that the Reynolds number of the experimental data does not match exactly the one used in the simulations. This fact may be more important for higher Reynolds number as has been mentioned in section 2.4.1. For instance, at Reynolds $5 \cdot 10^6$, a later separation is predicted by the simulations when compared to the experiments at $5.5 \cdot 10^6$. The difference may be due to the fact that at higher Reynolds the wake becomes wider as the separation occurs at lower angles on the surface of the cylinder.

#### 3.2.4.5 Simplified case

An additional simulation on a two-dimensional cylinder has been performed to estimate the error obtained when the boundary layer is not modelled and when the no-slip condition on the cylinders surface is not applied.

A steady simulation has been performed and, using the simplifications mentioned previously, a drag coefficient of 0.07 has been obtained for a Reynolds number of $9 \cdot 10^4$. This value is in clear disagreement with the results of the low Reynolds number approach computation which have led to a 1.2 drag coefficient value. The difference can be visualized by comparing Figure 3-19 (a) and Figure 3-18 (c).

The results obtained when applying the simplification resemble the potential flow as can be derived from Figure 3-19 (b). Only a slight difference can be appreciated at the rear side of the cylinder where the flow is slightly more separated.

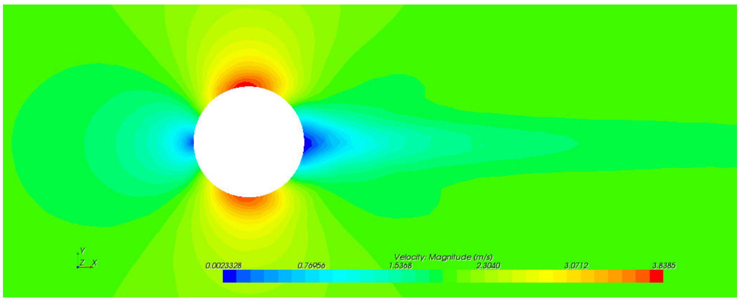

a) Velocity contours of the simplified case

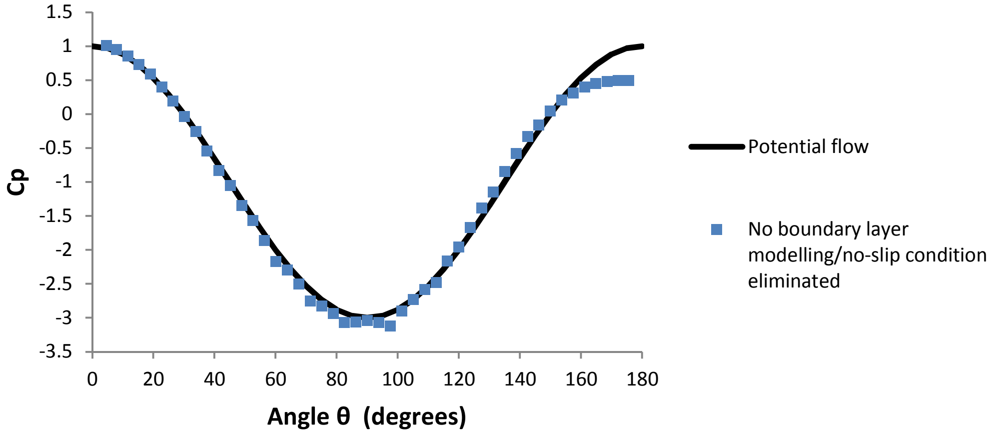

b) Pressure coefficient distribution of the simplified case

**Figure 3-19 – Results of the 2D cylinder simplified simulations**

### 3.2.5 Conclusions

The flow around two-dimensional circular cylinders has been simulated at three different Reynolds numbers (100, $9 \cdot 10^4$ and $5 \cdot 10^6$) and the results have been compared with previous studies calculations. In addition, a special simulation has been performed to derive the effects of dispensing with both the boundary layer and the no-slip condition.

The use of standard k-ε turbulence model with wall functions has been shown to be inadequate to represent the flow for Reynolds numbers where the boundary layer is not fully turbulent. For these cases, other approaches such as low Reynolds number turbulence models are required to be used. This implies dealing with higher mesh sizes and increasing the computational times.

The simplifications introduced to the special simulation (no boundary layer modelling and no-slip condition eliminated) have been shown to underestimate the drag coefficient very remarkably. Thus, the introduction of similar approximations to more complex geometries such as PLAT-O could lead to high inaccuracies.

The difficulties experienced to achieve a good boundary layer resolution in all the regions of the circular cylinder should be taken into consideration and further investigated. Moreover, if a future work was undertaken to validate the experimental results obtained for the pontoon drag, a comparison of the vortex shedding generated behind the support structure (three-dimensional cylinder) and the flow patterns of the two-dimensional simulations of this work could be performed.

## 3.3 PLAT-O

### 3.3.1 Model description

The PLAT-O prototype (Figure F-1) is composed of three pontoons and two turbines which are fitted between them. The ensemble is supported by a space frame which contains cylindrical and elliptical shaped struts. The power generated by the turbines is transported by means of two export lines.

The connections between the pontoons and the tag lines by a metallic piece have not been modelled similarly to the simulations on the isolated pontoon (section 3.1.2). In addition, the linking structure between both the pontoons and nacelles to the space frame has been simplified as can be appreciated in Figure 3-20.

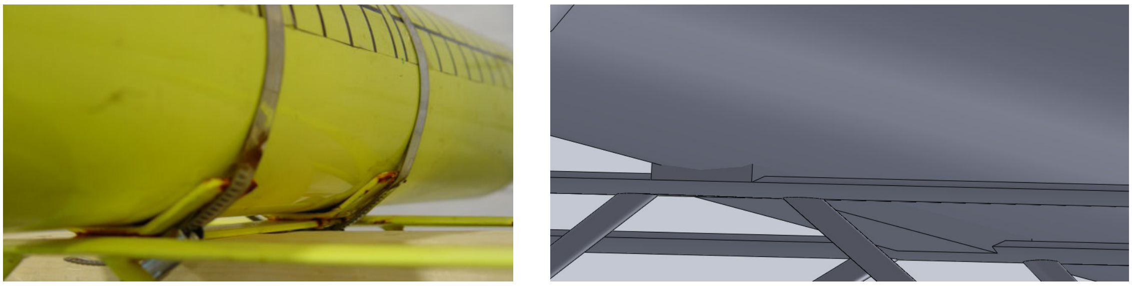

a) PLAT-O prototype detail

b) CAD model detail

**Figure 3-20 – Pontoon/Space frame connection**

Each power export line is composed of a bunch of three cables linked together with adhesive tape (Figure 3-21 (a)). The modelling of this geometrical feature has been performed by grouping the three original circumferential bases of the cables and by linking them with tangent lines to simulate the effect of the tape envelope as can be appreciated by comparing Figure 3-21 (c) and (d).

The final result represents an idealization of the real export lines as the cables position is not maintained with this shape throughout the whole length of the line. Instead, one of the cables is spiralled around the other two. Moreover, the real surface is much rougher than the idealized smooth finish as can be appreciated in Figure 3-21 (a).

In an attempt to reduce the complexity and the size of the simulations, the turbine's blades have not been incorporated in the geometry (Figure F-2).

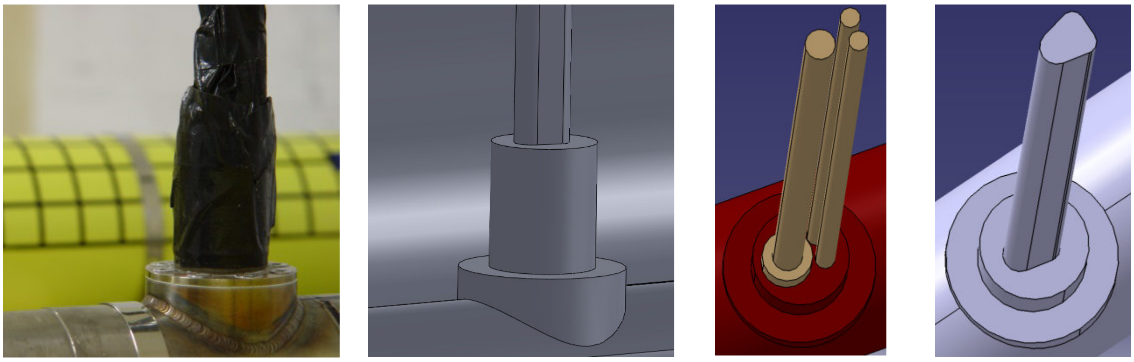

a) Detail power export cable (prototype)

b) Detail power export cable (CAD model)

c) Inner cables (CAD model)

d) Cables envelope (CAD)

**Figure 3-21 – Detailed views of the real and modelled power export line**

### 3.3.2 Experimental set up

Several testing campaigns have been conducted to assess the performance of PLAT-O technology during the years 2012 and 2013. In this study the focus will be on the tests carried out in Ifremer[5] on March and May 2013. The former were performed on the isolated PLAT-O turbines as can be derived from the experimental set up shown in Figure 3-22 (c). The latter were devoted to the entire PLAT-O prototype and made use of an hexapod to position it in the desired configuration (Figure 3-22 (a)). It is important to highlight that neither the mooring nor the tag lines were used in May tests.

From all the configurations analysed in the May 2013 tests, the present study focuses on the case with the current aligned to the prototype, parked turbines and without wave interaction effects. The monitored quantity of interest is the drag force.

---

[5] "Created in 1984, Ifremer is a public institute of an industrial and commercial nature. It is supervised jointly by the Ministry of Higher Education and Research and the Ministry of Ecology, Sustainable Development and Energy of France" (Ifremer, 2013).

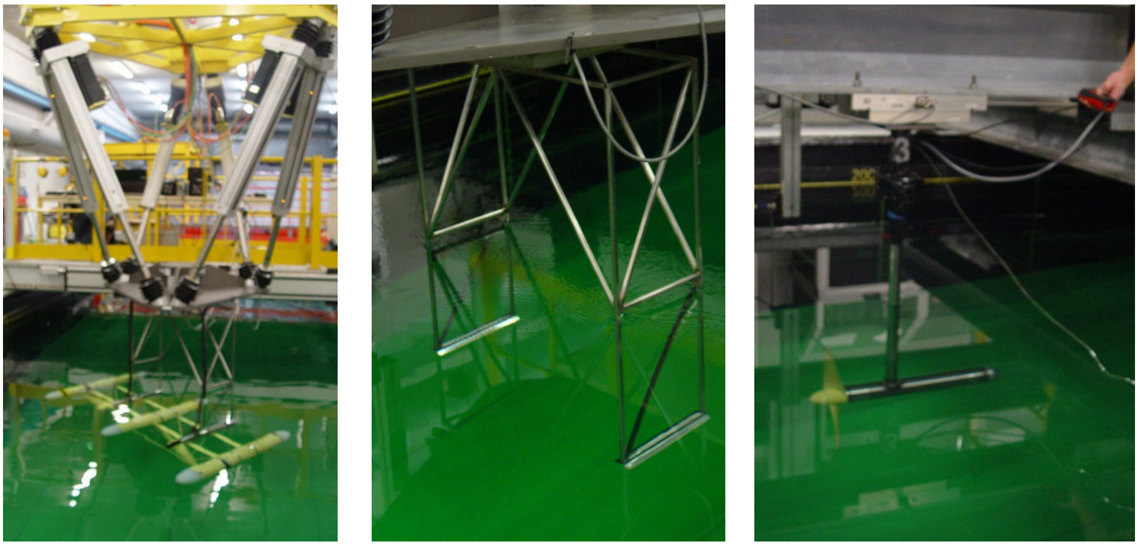

a) Ifremer May 2013 tests set up

b) May 2013 tests (structure only)

c) Ifremer March 2013 tests set up

**Figure 3-22 – Experimental set up of the Ifremer May and March tests**

As can be appreciated in Figure 3-22 (a), the structure used to hold PLAT-O and link it with the hexapod is also subjected to the current. In order to eliminate this undesired source of drag, the tests were performed on the structure isolated (Figure 3-22 (b)) and the values of resistance force were subtracted form the first tests. The same was done for the tests on the isolated turbine.

As has been mentioned in the previous section (3.3.1), the turbine blades have not been incorporated in the simulated geometry. In order to validate the CFD results, the values of the turbine's thrust obtained from the March tests have been subtracted from the total drag values of PLAT-O derived from May tests as can be appreciated in Figure 3-23.

This action adds some uncertainties to the results with which the CFD calculations have to be compared.

On the one hand, the thrust force derived from the March tests is representative of the turbine blades. However it is also caused by the nose of the nacelle and, to a less extent, to the skin friction along its body. For the parked condition, the flow is expected to be separated behind the blades preventing the formation of a boundary layer which generates skin friction drag on the surface of the nacelle. That is why the main contribution to the total thrust force, apart from the blades, is considered to be the front part. Because of that, the subtraction may not only eliminate the thrust of the blades but also the pressure drag in the nose of the nacelle from the total PLAT-O drag.

On the other hand, the March and May tests were performed using different levels of turbulence intensity. The former were performed at 25% and the latter at 5%. This constitutes another source of uncertainty.

In addition, the remaining drag after subtraction of the turbine's thrust may not be exactly the resistance of the simulated geometry because of interaction effects between the turbine and the structure.

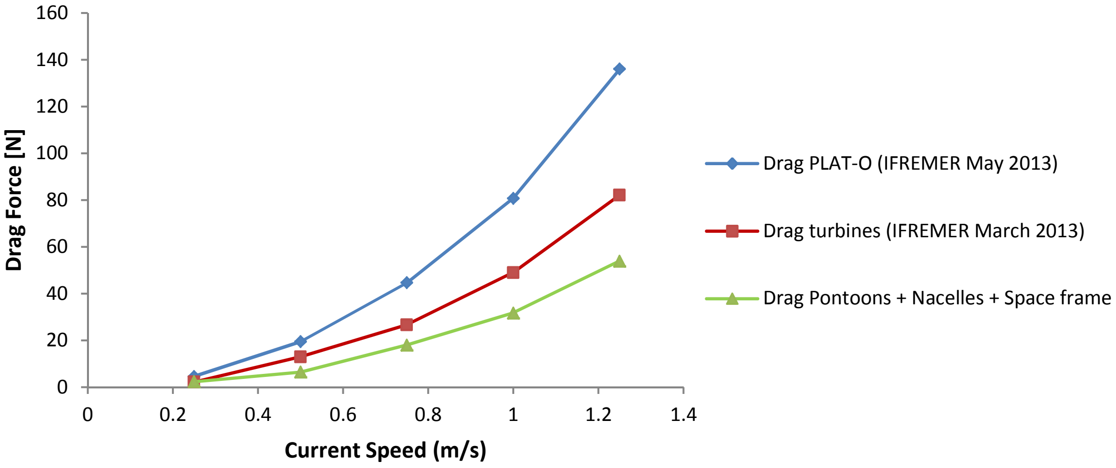

**Figure 3-23 – Experimental data**

### 3.3.3 Mesh

Both the trimmer and tetrahedral mesher modules have been employed in the mesh generation process. The difficulties experienced with the polyhedral refinement operations (section 3.2.1.3) have led to the use of a tetrahedral grid.

It has been observed that smoother transitions from the finest elements to the largest ones can be more efficiently achieved with the trimmer module. A gradual increase of elements size in the tetrahedral mesh leads to a much higher number of cells in the final grid. Figure 3-24 shows a comparison of the behaviour of the two mesh modules on a plane section across the nacelle.

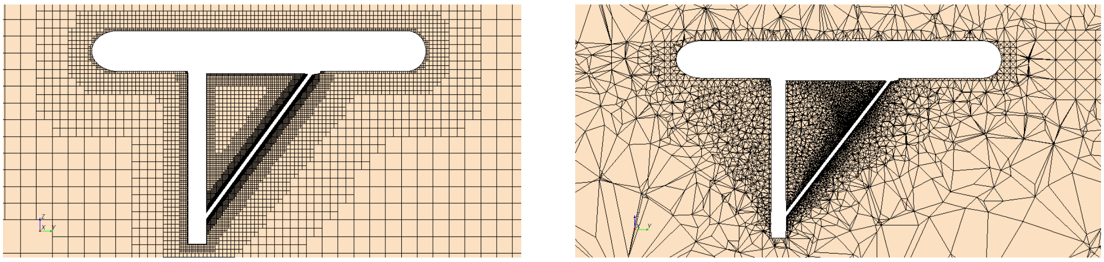

a) Trimmer mesh

b) Tetrahedral mesh

**Figure 3-24 – Detailed view of the PLAT-O mesh**

From Figure 3-24 (b) it can be observed that the density of elements is very high at the structure region but away from it becomes very coarse. A clearly different pattern can be observed in Figure 3-24 (a).

The mesh size of (b) is 5.5 million cells whereas the size of mesh (a) is 5 million. It can be clearly deduced that a lower growth rate of elements in (b) would result in a much higher element count. Therefore, the final mesh has been generated using the trimmer module.

### 3.3.3.1 Domain boundaries

A rectangular domain has been used to simulate only one current direction similarly to the one used by Atluri et al. (2006) showed in Figure 2-18 (section 2.4.3).

The outlet boundary has been positioned based on the results obtained from the sensitivity analysis performed on the isolated pontoons simulation (section 3.1.3.1). A distance of eight body lengths has been established between the prototype and the outlet plane.

The inlet and lateral boundaries have been positioned one and a half body lengths from the prototype exactly as in the isolated pontoon’s domain.

With regard to the boundaries representing the free-surface and the floor they have been situated at the same locations as in Ifremer water channel. Even if it has been mentioned that no free-surface effect is expected, keeping the same distance from the prototype to the surface as in the experimental set up is important if the power export cables drag wants to be simulated. Obviously, the higher the lines length submerged the higher the resistance obtained.

A schematic of the size of the computational domain has been represented in Figure F-3.

The turbulence intensity on the inlet and outlet boundaries has been established as 5% to reproduce the experimental conditions.

#### 3.3.3.2 Near-wall region

Two meshes for the use of wall functions with and without the power export lines have been generated. Similarly to the strategy followed by Constantinides et al. (2011), the boundary layer of both the cylindrical and elliptical struts has not been modelled in order to reduce the problem size. The present study has introduced a further simplification and has supressed the no slip condition on the struts by assigning a symmetry condition to them.

The boundary layer on the pontoons and nacelles has been modelled in accordance with the guidelines for the use of wall functions. The parameters of the near wall grid used in the isolated pontoons simulation have been employed as guidance. The distribution of wall y+ distance as well as a detail of the mesh on the nacelle and the pontoon can be observed in Figure 3-25.

The simplification of not modelling the boundary layer and of applying a symmetry boundary condition has also been applied to the power export lines. The implications of such considerations will be discussed in section 3.3.5.

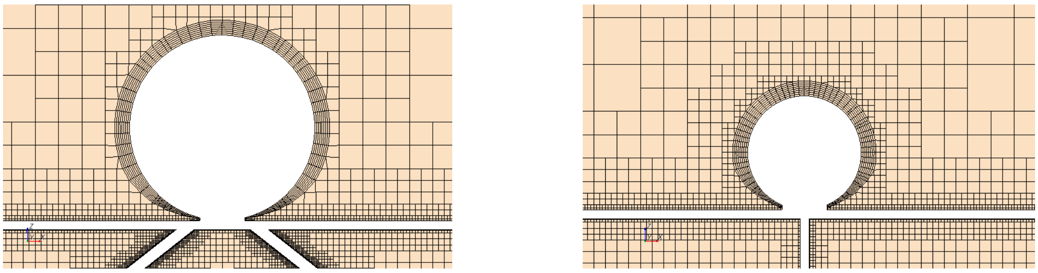

a) Detail of the pontoon’s mesh

b) Detail of the nacelle’s mesh

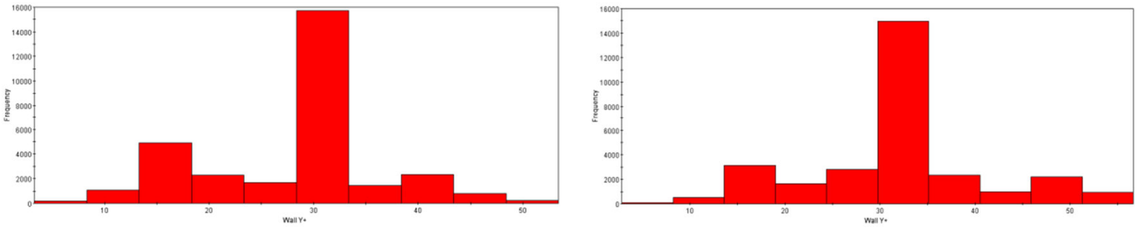

c) y+ distribution for the pontoon

d) y+ distribution for the nacelle

**Figure 3-25 – Details of the pontoons' and nacelles' near wall region mesh**

### 3.3.3.3 Mesh refinement

The size of the surface mesh elements has been tuned to accurately represent the geometrical features of PLAT-O prototype. Figure 3-26 shows, as an example, the comparison between different resolution accuracy of the cylindrical struts (the bold black line represents the original geometry).

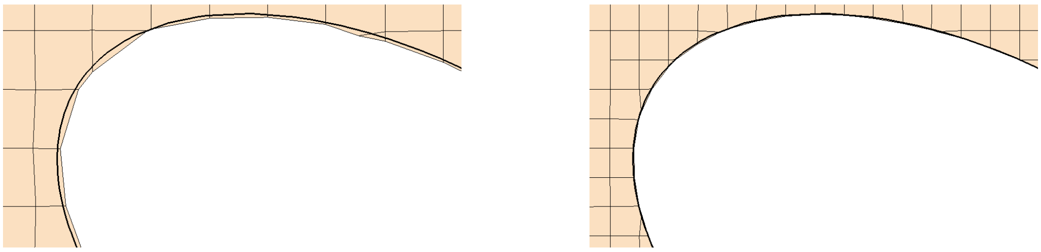

a) Poor surface resolution

b) Adequate surface resolution

**Figure 3-26 – Comparison of surface mesh resolutions**

A higher density of cells has been allocated to the wake region behind the pontoons and the nacelles by means of the Star CCM+ *volumetric control* tool as can be appreciated in Figure F-4.

A smooth transition between the smallest elements and the largest has automatically allocated more density of cells in the space frame area than in the outer regions where little flow action is expected. However, it can be observed from Figure 3-25 (a) that the cell size change between the boundary layer region of the pontoons and the outer domain is rather abrupt. A smoother transition would have led to a much bigger grid size.

In Figure F-5 and Figure 2-1 some views of the mesh can be appreciated.

#### 3.3.3.4 Quality

The Star CCM+ tool *mesh diagnostics* mentioned in section 2.2.3.1 has been used to assess the quality of the mesh.

From the results obtained it has been derived that the maximum skewness angles fall below the threshold of 85º as recommended by the Star CCM+ user-guide (2013). In addition, it has been checked that the majority of cells (97%) fall within the range of highest quality with respect to volume change and face validity metrics. No cells have been found below the minimum tolerable quality threshold.

#### 3.3.3.5 Verification

A mesh sensitivity study has been conducted to ensure independence of results with respect to the grid size. The outcome has been shown in Figure F-7. A difference of 2.85% with respect to the total drag value has been obtained between the medium and fine meshes. It can be concluded that mesh independence has been achieved and, for the sake of efficiency, the medium grid has been used for the simulations.

### 3.3.4 Features of the simulation

The fluid flow has been modelled with the incompressible, viscid, isothermal and steady Reynolds-Averaged Navier-Stokes equations. The Star CCM+ properties of water by default have been used.

The simulation has been performed with a Gauss-Seidel iterative algorithm, a second-order upwind interpolation scheme and the SIMPLE pressure-velocity coupling. The k-ε turbulence model has been used.

Several simulations have been undertaken for different current velocities in order to obtain the characteristic drag curve of PLAT-O 1:12 scale prototype. In addition, two geometrical configurations (with and without power export lines) have been analysed as shown in Figure F-2.

### 3.3.5 Results and discussion

#### 3.3.5.1 Convergence

Similarly to the previous cases, both the residuals and the drag force have been monitored to ensure that a converged solution was obtained. From Figure F-8 it can be appreciated that the residuals fall below the threshold of 0.001 and that the drag force undergoes no changes with further iterations. The plot of Figure F-8 corresponds to a velocity of 1.3 m/s and to the configuration without the power export cables. The trend obtained has been very similar for the other current speeds and configuration analysed.

#### 3.3.5.2 Drag calculation

The computed values of the total PLAT-O resistance for different current velocities and for the two configurations analysed (with and without power export lines) have been summarized in Figure 3-27. Moreover, in Figure 3-28 the separate contributions of the different PLAT-O components to the total drag have been shown for the configuration with power export lines.

It can be appreciated that the CFD calculations have underestimated the total value of the PLAT-O drag in comparison with the experimental data. The cause of discrepancy has been attributed to several factors.

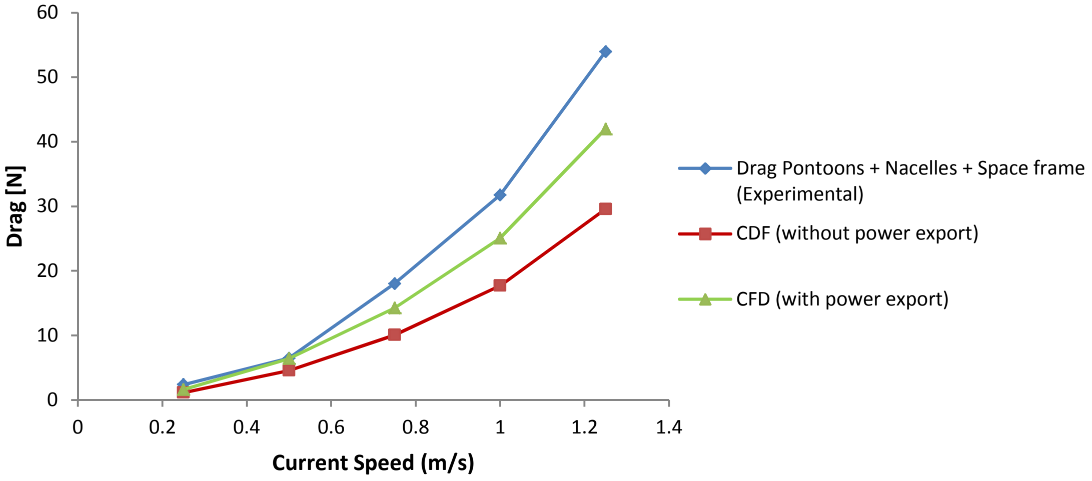

**Figure 3-27 –CFD calculations and experimental drag**

The simplifications on the geometry have eliminated from the simulations some elements which contribute to an increase of the total resistance, similarly to the study of Phillips et al. (2007) in which the total drag of SOTON AUV was underestimated.

Contrarily to the connections between the space frame/pontoons and space frame/nacelles, the power export cables have a big size and the idealization of its shape may lead to significant errors. From Figure 3-28 it can be appreciated that the contribution of the power lines to the total drag is relevant, only overtaken by the resistance of the space frame.

In spite of the potential effect of the geometry simplifications, the most important cause of discrepancy is hypothesized to be the inexistent modelling of the boundary layer on the power export lines and space frame elements, particularly the cylindrical struts.

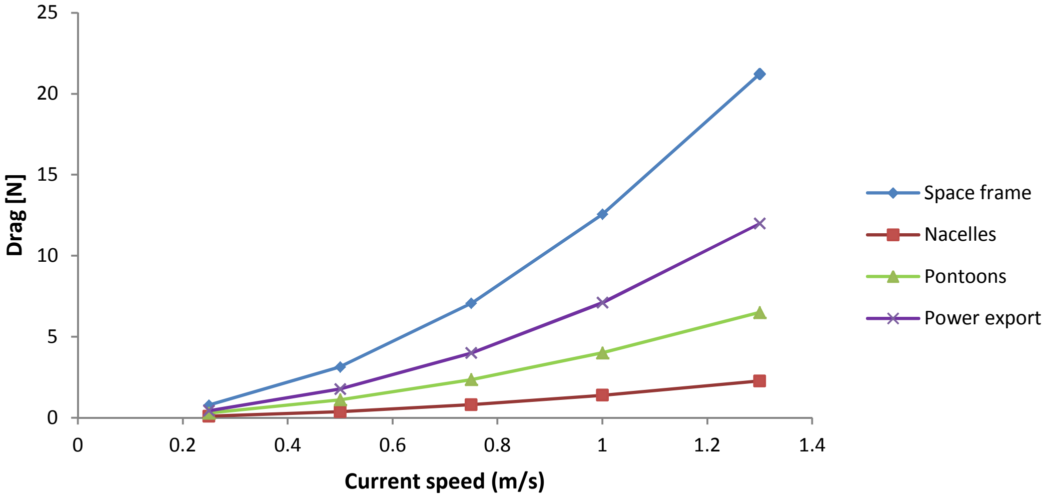

**Figure 3-28 – PLAT-O drag contributions (CFD with power export)**

In section 3.2.4.5 it has been stated that, without modelling the boundary layer and the no-slip condition, for a Reynolds number of $9 \cdot 10^4$ the drag coefficient value of the flow around a two-dimensional circular cylinder is very low in comparison with the accurate simulations. Actually, it has been shown that a solution similar to potential flow is obtained.

It has to be taken into account, though, that the range of Reynolds numbers at which the PLAT-O cylindrical struts are operating in experimental conditions are much lower than $9 \cdot 10^4$. For instance, at the highest speed current of 1.3 m/s the Reynolds number is $1 \cdot 10^4$. Therefore, the difference with respect to drag observed at $9 \cdot 10^4$ should not be directly assumed as to be the same as for $1 \cdot 10^4$.

In order to overcome the deficiencies of the simplifications used, it could be suggested to model the near wall region of the cylindrical struts with wall functions as Constantinides et al. (2011) and Atluri et al. (2006) did in his study of the flow around the cylinder array in a truss spar (section 2.4.3). Both studies underlined that it reduced the problem size in comparison with the use of a low Reynolds number turbulence approach.

However, as has been concluded in section 3.2, the use of wall functions for Reynolds numbers where the boundary layer is not fully turbulent, such as those at which PLAT-O is operating, leads to results in clear disagreement with experimental data. Actually, the simulated flow is representative of the supercritical regime.

This may not be an issue for Constantinides et al. (2011) and Atluri et al. (2006) because of the higher current speeds simulated and dimension of the struts of the cylindrical array. They lead to much higher operational Reynolds numbers in comparison to the PLAT-O prototype. Therefore, in contrast to the present study, the characteristics of the boundary layer around the cylinders of the Spar truss structure fall within the validity of application of the wall functions.

The only alternative approach to accurately model the boundary layer of PLAT-O space frame struts is the use of a low Reynolds turbulence model. Its use is subjected to the clustering of enough cells near the body wall to fully resolve the region. Because of that, the size of the mesh is drastically increased and powerful computational resources become essential. The high costs associated with the calculations preclude the use of this low Reynolds number approach especially within the time and resources limitations of this study.

#### 3.3.5.3 Velocity contours

Apart from the computation of the PLAT-O drag, CFD enables to better understand the flow around the device.

One of the main regions of interest is the area swept by the turbine blades which has been represented as a dotted line in Figure 3-29. The local acceleration of the flow around the nose of the nacelles can be appreciated. Outside this region, slightly higher values of velocity than the free stream current speed can be observed.

From the several testing campaigns performed, it has been demonstrated that the power coefficient of the turbines is higher when they are operating linked to PLAT-O than when they are tested isolated (Fabre, 2013). This fact is hypothesised to be linked to the local increase of velocity at the turbine's area based on the predictions by CFD.

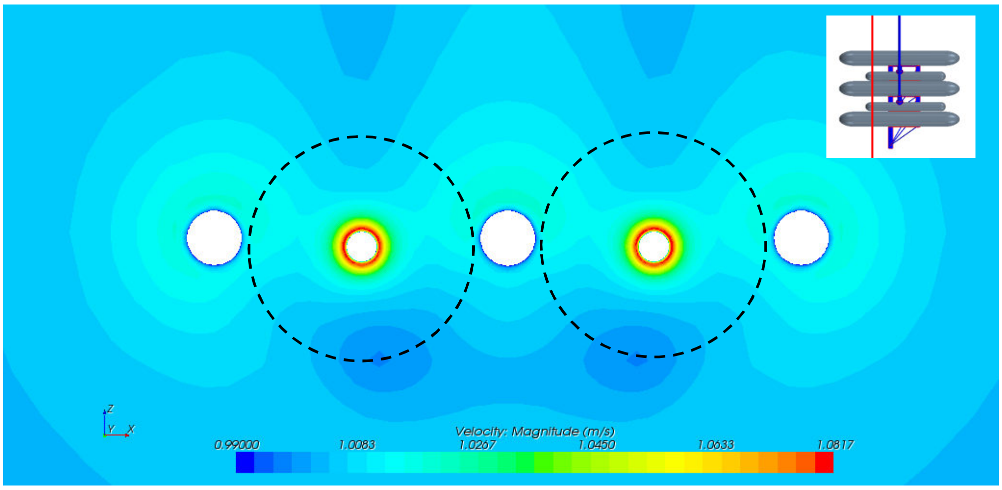

**Figure 3-29 – Velocity contours on the PLAT-O turbine's plane (*U=1m/s*)**

The underlying cause of the velocity increase is the effect of flow constrainment imposed by the pontoons and nacelles. From the conservation of mass flux, for incompressible flows a reduction of the sectional area through which the fluid is flowing is accompanied by an increase of velocity.

From Figure 3-30 the velocity contours around the different struts of PLAT-O on a horizontal plane section can be appreciated. The similarity with potential flow mentioned in section 3.2.4.5 can be visualized at the cylinders on the both sides of the elliptical shape where the flow separates at a relatively narrow area. In reality, the flow is expected to separate earlier and to produce a wider wake which would increase the predicted resistance. Some degree of interaction effect between the wake of the front cylindrical struts and the rear ones can be also appreciated.

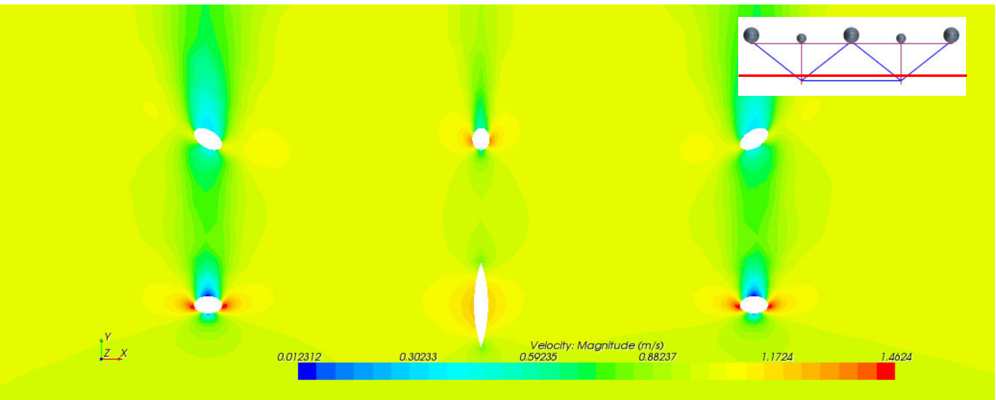

**Figure 3-30 –Velocity contours around the space frame struts (*U=1m/s*)**

The inclination of the cylinders suggests that, for parametric design, it may be not accurate enough to use the drag coefficient of a circular cylinder. It should be investigated whether the drag calculations are on the conservative side or not.

The extension of the wake is relevant specially when conceiving the distribution of PLAT-O devices in an array at more advanced development stages. From Figure F-9 it can be appreciated that at a downstream length of approximately 4 meters behind PLAT-O the velocity has recuperated the free-stream value. The results should be interpreted with care as they do not include the effect of the turbines.

### 3.3.6 Conclusions

Several CFD simulations at different current speeds have been performed on the PLAT-O prototype. The values of drag obtained have been contrasted against experimental data and significant differences have been observed. In addition, several features of the flow have been investigated.

The time constraints of the present study have influenced the level of complexity of the simulations. The modelling of the turbines and the effects of skewed flow has been precluded. Further work should be undertaken to address their effect.

The low range of Reynolds numbers at which PLAT-O has been tested does not allow modelling the boundary layer at the space frame elements using wall functions without obtaining spurious results. The use of a low Reynolds number turbulence model approach is prohibitive because of the huge mesh size that would be associated with it and the limited time and resources available for this study. In view of these statements, CFD may not be an efficient tool for the accurate drag estimation of the PLAT-O prototype at the scale analysed.

Notwithstanding, Sustainable Marine Energy (SME) plans to avoid the use of naked cylinders in the space frame because of the problems associated with vortex shedding vibrations and fatigue. The company has been studying the use of fairings around the struts to provide a more aerodynamic shape to the structure components.

Both the increase of the scale and the introduction of structural elements less prone to separation may make suitable the use of wall functions. Therefore, it can be predicted that, for future developments, CFD may become a useful tool to help in the design process predicting key parameters such as drag.

For low scale developments, the fact that CFD is not suitable enough to assess the design is relatively not important as the cost of prototypes at early stages is low and a high level of optimization is out of the scope. Contrarily, for larger scales the costs are increased and a certain extent of optimization is desirable. At such stages CFD could turn into a valuable design ally.

# REFERENCES

1 Allmendinger, E.E., De La Vergne, M., Jackson, H.A. (1990), ''Hydromechanical principles'', in: Almendinger, E.E. (editor), *Submersible Vehicle Systems Design*, The Society of Naval Architects and Marine Engineers, Jersey City, p. 191-269.

2 Alvarez, A., Bertram, V., Gualdesi, L. (2009). *Hull hydrodynamic optimization of autonomous underwater vehicles operating at snorkelling depth*. Ocean Engineering, 36 (1), p. 105-112.

3 Atluri, S., Halkyard, J., Sirnivas, S. (2006), C*FD simulation of truss spar vortex-induced motion*, in: 25th International Conference on Offshore Mechanics and Arctic engineering, Vol. 4, 4-9 June 2006, Hamburg, p. 787-793.

4 AUVAC (Autonomous Undersea Vehicle Applications Center), AUV System Spec Sheet, available at: http://auvac.org/configurations/view/86/ (accessed 6th August 2013).

5 Cantwell, B.J. (1976). *An experimental study of turbulent near-wake of a circular cylinder at Re=140,000*. PhD thesis, Caltec, Calif.

6 COMSOL, Flow across a cylinder, available at: http://www.rpi.edu/dept/chem-eng/WWW/faculty/plawsky/Comsol%20Modules/CylinderTransient/Ch13CylinderTime.html (accessed 1st August 2013).

7 Constantinides, Y., Holmes, S., Yu, W. (2011), *VIV Prediction of a Truss Spar Pull-Tube Array Using CFD*, in: 30th International Conference on Ocean, Offshore and Arctic Engineering, Vol. 7, 19-24 June 2011, Rotterdam, ASME, p. 637-643.

8 Cox, J.S., Rumsey, C.L., Brentner, K.S., and Younis, B.A. (1997) *Computation of Sound Generated by Viscous Flow Over A Circular Cylinder*, Proceedings of the ASME/JSME/IMechE/CSME/IAHR 4th International Symposium on Fluid-Structure Interactions, Aeroelasticity, Flow-Induced Vibration and noise.

9 ERCOFTAC Special Interest Group on ‘Quality and Trust in Industrial CFD’, (2000), *Best Practice Guidelines*, version 1.0, Sulzer Innotec.

10 Fabre, R. (2013), *An investigation of the influence of the support structure on the turbine performance of a moored tidal energy converter* (Master of Science thesis), Cranfield University, Cranfield.

11 Hallam, M. G., Heaf, N. J., Wootton, L. R. (1977), *Dynamics of marine structures: methods of calculating the dynamic response of fixed structures subject to wave and current* action, Underwater Engineering Group, London.

12 Hoerner, S. F. (1965), *Fluid-dynamic drag: practical information on aerodynamic drag and hydrodynamic resistance*, (3rd edition), Midland Park.

13 Homann, F. (1936). Influence of higher viscosity on flow around cylinder (in German). *Forschung aus dem Gebiete des Ingenieurwesen*, 17, 1-10, transl. 1952. NACA TM 1334.

14 Hoftyzer, M., Dragomirescu, E. (2010), *Numerical investigation of flow behaviour around inclined circular cylinders*, in: 5th International Symposium on Computational Wind Engineering, 23-27 May 2010, North Carolina.

15 Ifremer, (2013), available at: http://wwz.ifremer.fr/institut_eng/The-Institute (accessed 6th August).

16 James, W.D., Paris, S.W., and Malcolm, G.V. (1980). *Study of viscous cross flow effects on circular cylinders at high Reynolds numbers*. AIAA Journal, 18, 1066-72.

17 Liaw, K.F. (2005), *Simulation of Flow around Bluff Bodies and Bridge Deck Sections using CFD*, PhD thesis, University of Nottingham, Nottingham.

18 McDonough, J.M. (2007), *Introductory lectures on turbulence*, Departments of Mechanical Engineering and Mathematics, University of Kentucky.

19 Mittal, R., Balachandar, S. (1995), *Effect of Three-Dimensionality on the Lift and Drag of Nominally Two-Dimensional Cylinders*, Physics of Fluids, Vol. 7, No. 8, p. 1841-1865.

20 Pasquale, D., Rona, A., Garrett, S.J. (2009). *A selective review of CFD transition models*. In: 39th AIAA Fluid Dynamics Conference, San Antonio, Texas, June 22-25 2009.

21 Phillips, A., Furlong, M., Turnock, S.R. (2007). *The Use of Computational Fluid Dynamics to Assess the Hull Resistance of Concept Autonomous Underwater Vehicles*. In: OCEANS 2007, Aberdeen, Scotland, June 18-21 2007, p. 1-6.

22 Recommended Practice DNV-RP-C205, October 2010, p. 86-98.

23 Roshko, A. (1960), *Experiments on the Flow Past a Circular Cylinder at Very High Reynolds Number*, Journal of Fluid Mechanics, Vol. 10, No. 2, 1961, pp. 345-356.

24 Sanci, S. (2006), *Design of a torpedo: study of drag reduction using computational fluid dynamics* (Master of Science thesis), Bogaziçi University.

25 Schlichting, H (1968), *Boundary-Layer Theory*, (6th edition), McGraw-Hill, United States.

26 Star CCM+ user-guide (2013), CD-Adapco (Steve portal).

27 Stevenson, P., Furlong, M., Dormer, D. (2009), *AUV design – shape, drag and practical issues*. Sea Technology, 50, (1), p. 41-44.

28 Tu, J., Yeoh, G. H., and Liu, C. (2008), *Computational fluid dynamics: a practical approach [electronic resource],* (1st edition), Amsterdam, Boston, Butterworth-Heinemann.

29 White, F. M. (2007), *Fluid mechanics,* (5th edition), McGraw-Hill, Boston.

30 Wilcox, D. C. (2006), *Turbulence modeling for CFD,* (3rd edition), La Cãnada, DCW Industries.

31 Zdravkovich, M. M. (1990), *Conceptual overview of laminar and turbulent flows past smooth and rough circular cylinders*, Journal of Wind Engineeing and Industrial Aerodynamics, Vol. 33, p. 53-62.

32 Zdravkovich, M. M. (1997), *Flow around circular cylinders*, Vol. 1, Oxford University Press, New York.

33 2b1stConsulting, Jacket, available at: http://www.2b1stconsulting.com/jacket/ (accessed 6th August 2013).

# APPENDICES

## Appendix A Drag estimation using ITTC 57

The total drag coefficient is expressed as:

$$C_D = (1 + k) \cdot C_F \tag{A-1}$$

*where $C_D$ is the total drag coefficient, $k$ is the form factor and $C_F$ is the friction drag coefficient.*

One of the methods to estimate the skin friction drag widely used in the design of ship hulls is the ITTC 57 correlation line:

$$C_F = \frac{0.075}{(\log(R_N) - 2)^2} \tag{A-2}$$

*where the Reynolds number is based on the body length and $C_F$ defined based on wetted surface area.*

It should be underlined that the experiments from which the ITTC curve was obtained were performed with a turbulent boundary layer flow over flat plate.

There exist different form factors formulations for different body shapes. As an example, for a streamlined body Hoerner (1965) proposed:

$$(1 + k) = 1 + 1.5 \cdot \left(\frac{d}{l}\right)^{\frac{3}{2}} + 7 \cdot \left(\frac{d}{l}\right)^{3} \tag{A-3}$$

*where d is the diameter of the body and l the length.*

# Appendix B Wall distance estimation

As explained in section 2.2.3, the prism layer mesher module of STARCCM+ enables to specify the wall distance from the body surface to the mesh point adjacent to it. By using some empirical correlations for the skin friction coefficient and equation (2-26) the value of y can be estimated.

From equation (2-26) the value of y is isolated resulting in:

$$y = \frac{y + \cdot \mu}{\rho \cdot u_\tau} \tag{B-1}$$

The wall shear stress is expressed as:

$$\tau_w = c_f \cdot \frac{1}{2} \cdot \rho \cdot u_{free-stream}^2 \tag{B-2}$$

The skin friction coefficient $c_f$ is estimated using one of the following formulae (from STAR CCM+ user-guide (2013)):

$$c_f = 0.0576 \cdot Re_x^{\frac{-1}{5}} \quad for \quad 5 \cdot 10^5 < Re < 10^7 \tag{B-3}$$

$$c_f = 0.0592 \cdot Re_x^{\frac{-1}{5}} \quad for \quad 5 \cdot 10^5 < Re < 10^7 \tag{B-4}$$

The Reynolds number is calculated as:

$$Re_x = \frac{\rho \cdot u_{free-stream} \cdot L_{characteristic}}{\mu} \tag{B-5}$$

The frictional velocity can be calculated as:

$$u_\tau = \left( \frac{c_f \cdot \frac{1}{2} \cdot \rho \cdot u_{free-sream}^2}{\rho} \right)^{\frac{1}{2}} \tag{B-6}$$

Finally, the value of $u_\tau$ can be introduced into equation (B-1). By imposing the desired y+ value, an approximate distance of the first point of the mesh adjacent to the wall to it can be obtained.

# Appendix C Interface Design

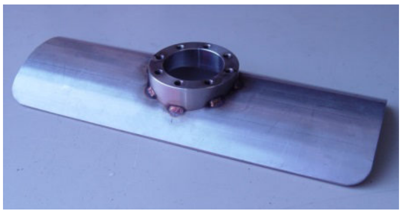

Figure C-1 – Pontoon interface

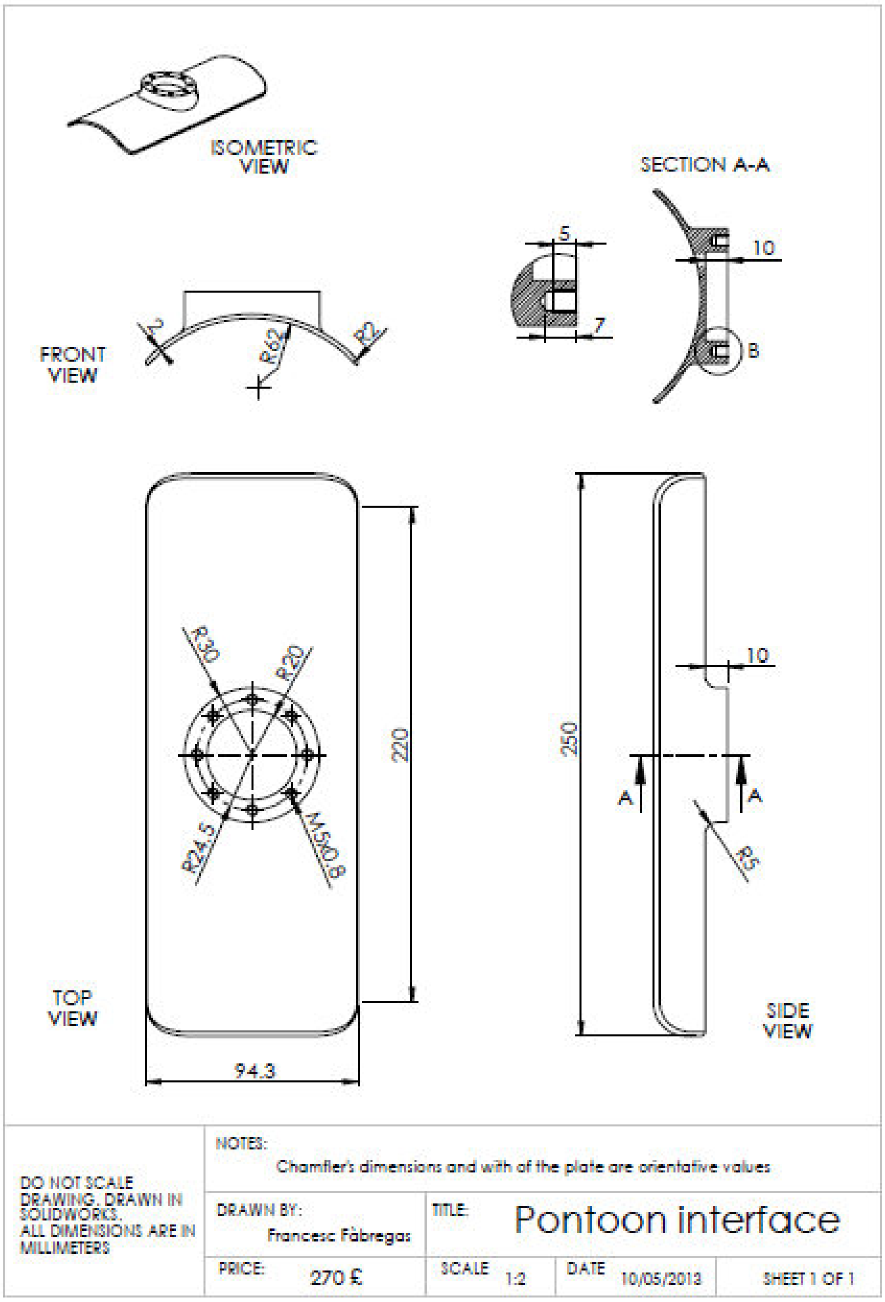

Figure C-2 – Pontoon interface drawing

# Appendix D PLAT-O pontoon

## D.1 Computational domain boundaries

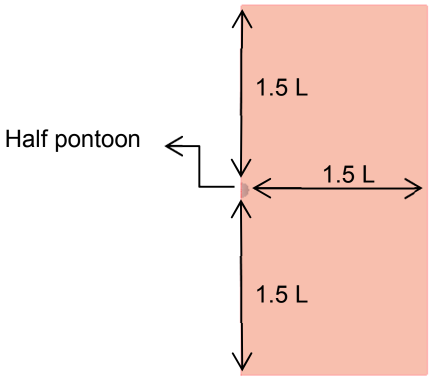

a) Front view

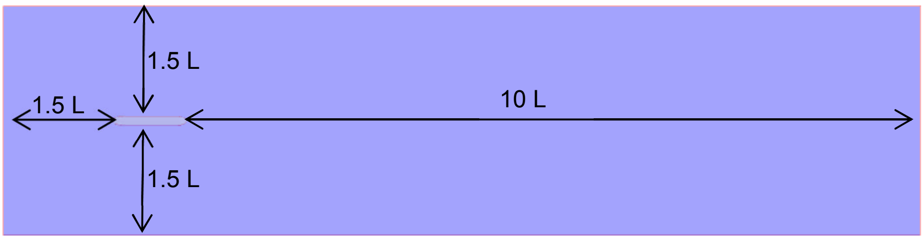

b) Side view

**Figure D-1 – Domain boundaries**

## D.2 Mesh

### D.2.1 Mesh images

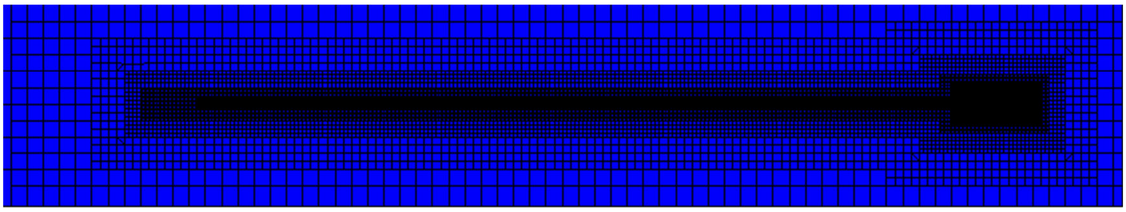

a) Whole grid domain

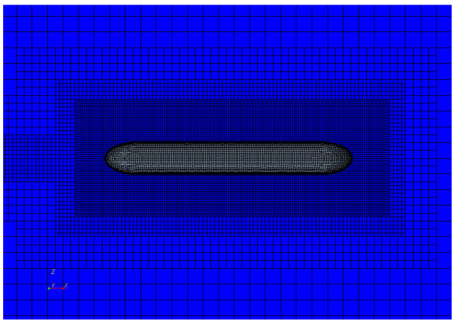

b) Detail of the grid at the pontoon region

**Figure D-2 – Pontoon grid views**

### D.2.2 Mesh independence study

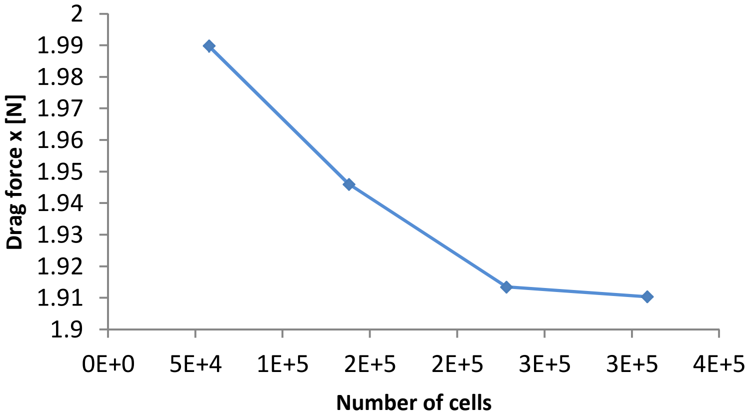

a) k-ε

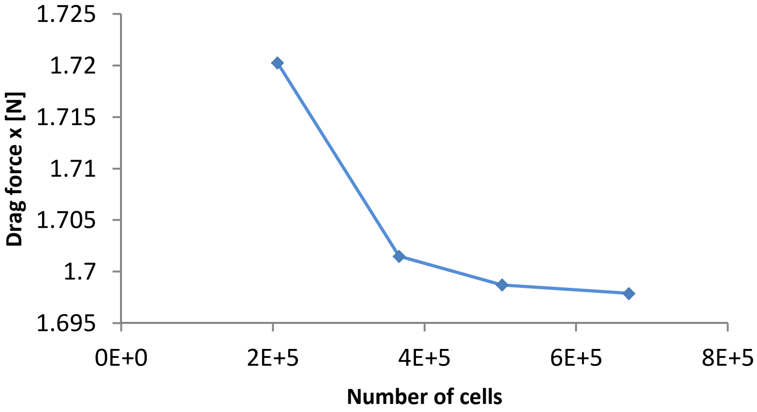

b) SST k-ω

**Figure D-3 – Mesh independence study**

## D.3 Monitored quantities

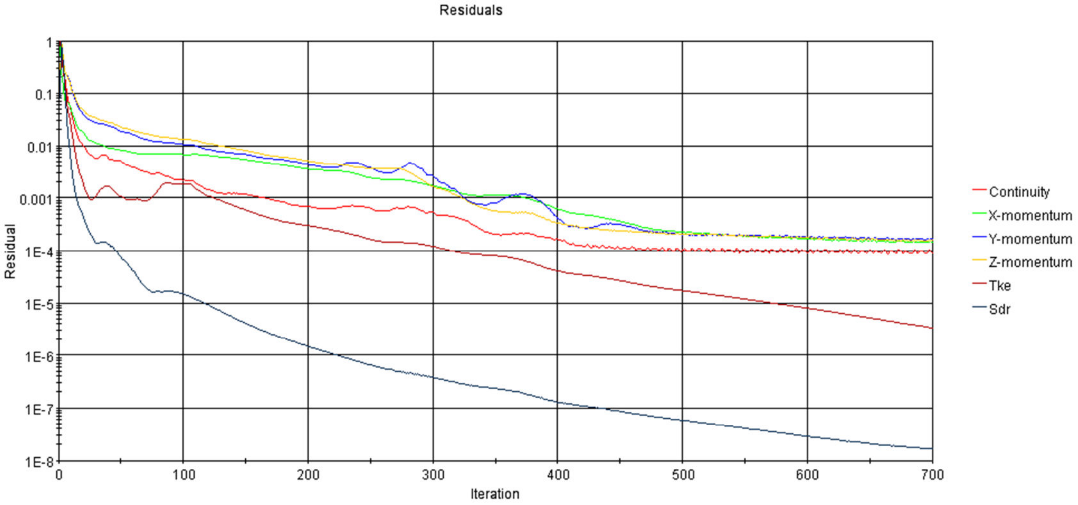

a) Residual plot

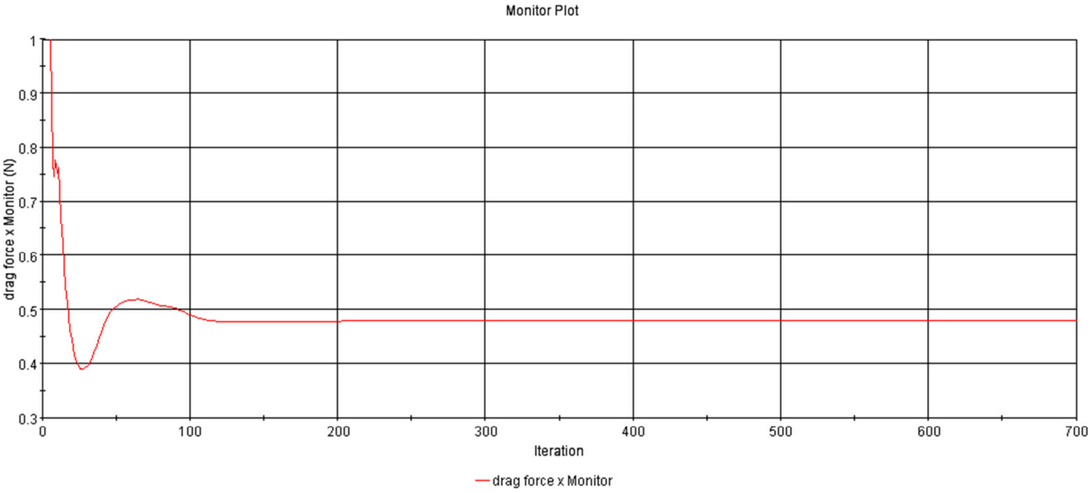

b) Drag coefficient plot

**Figure D-4 – Monitored quantities to assess convergence**

# Appendix E 2D Cylinders

## E.1 Computational domain boundaries

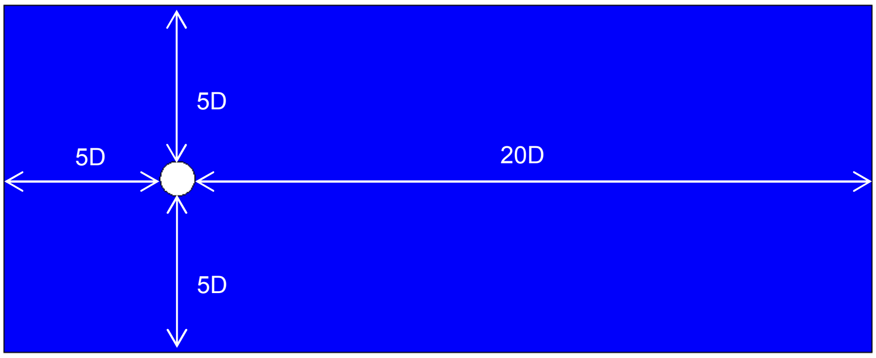

**Figure E-1 – Computational domain boundaries**

## E.2 Sensitivity studies

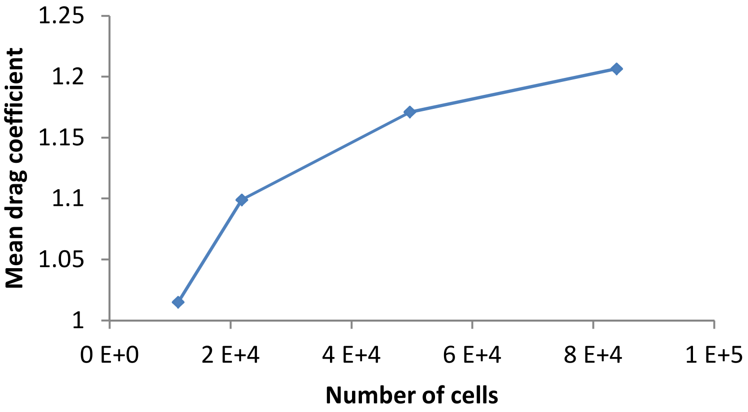

a) Mesh sensitivity (drag)

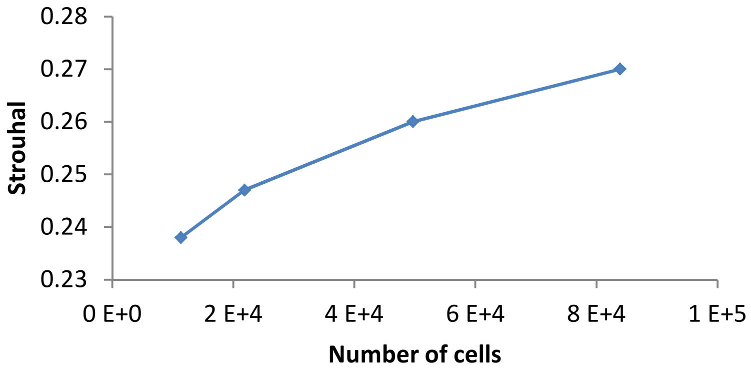

b) Mesh sensitivity (Strouhal)

**Figure E-2 – Mesh sensitivity on both the drag coefficient and Strouhal**

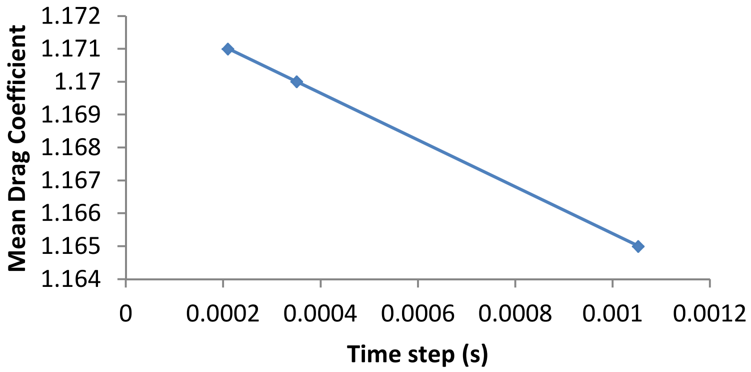

a) Time sensitivity (drag)

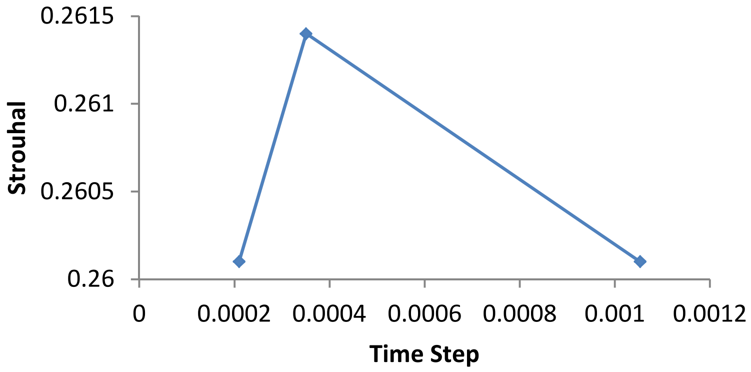

b) Time sensitivity (Strouhal)

**Figure E-3 – Time sensitivity on both drag coefficient and Strouhal**

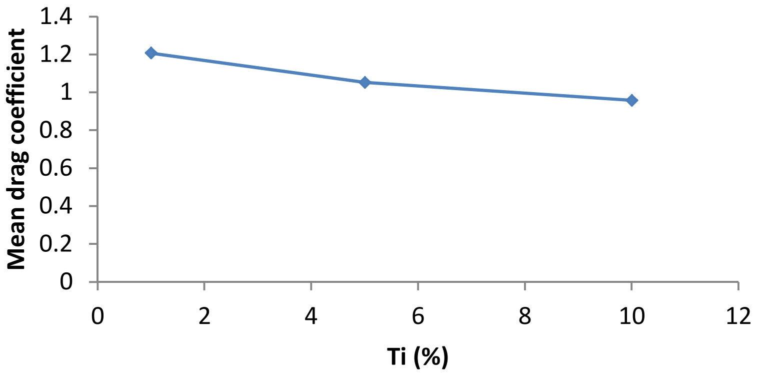

a) Turbulence intensity sensitivity (drag)

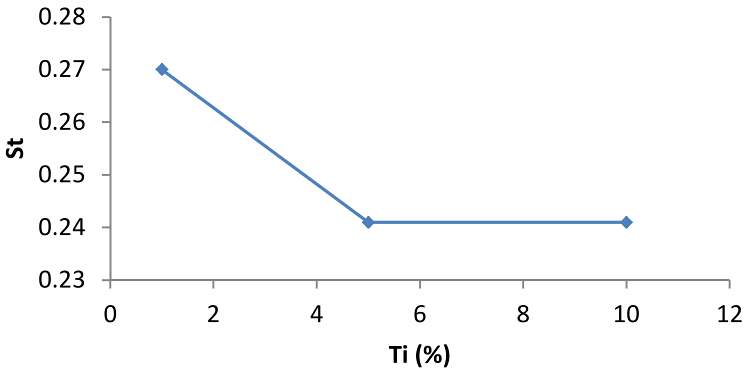

b) Turbulence intensity sensitivity (Strouhal)

**Figure E-4 – Turbulence sensitivity on both drag coefficient and Strouhal**

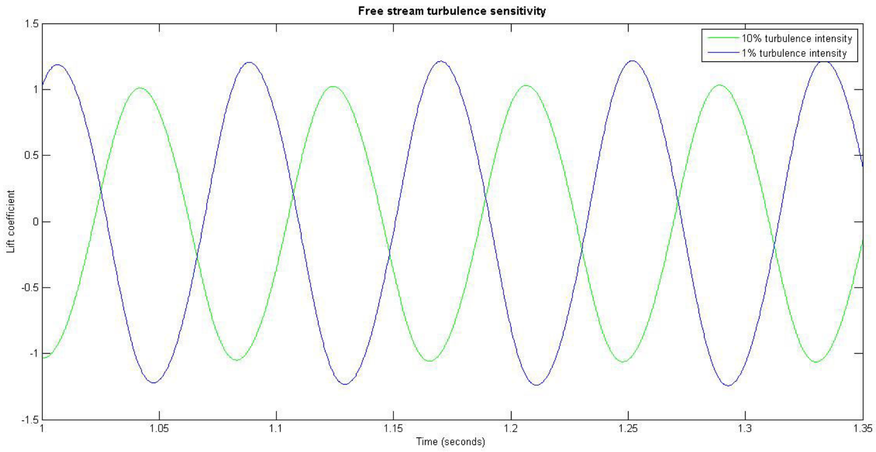

**Figure E-5 – Turbulence sensitivity on the lift coefficient**

## E.3 Monitored quantities

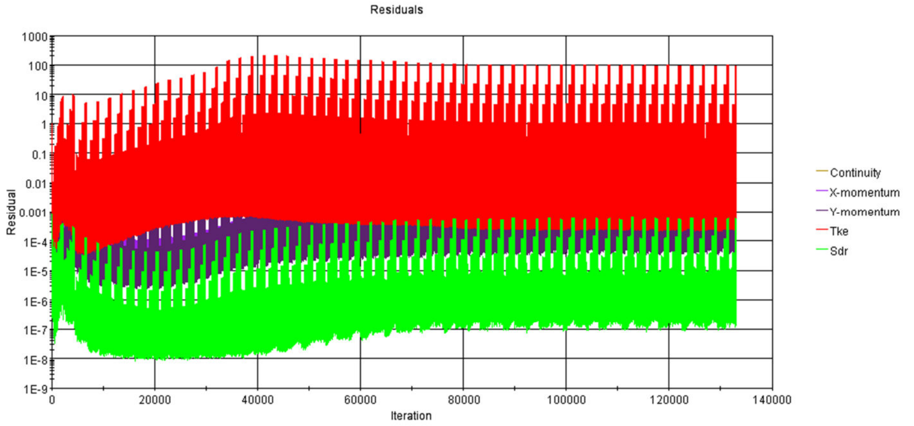

a) Whole history of residuals

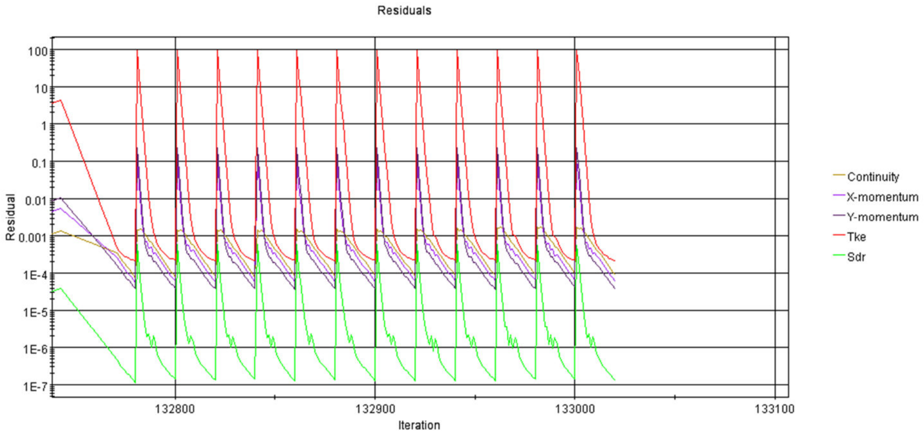

b) Detail of residuals

**Figure E-6 – Residuals history (Re=9·10$^4$)**

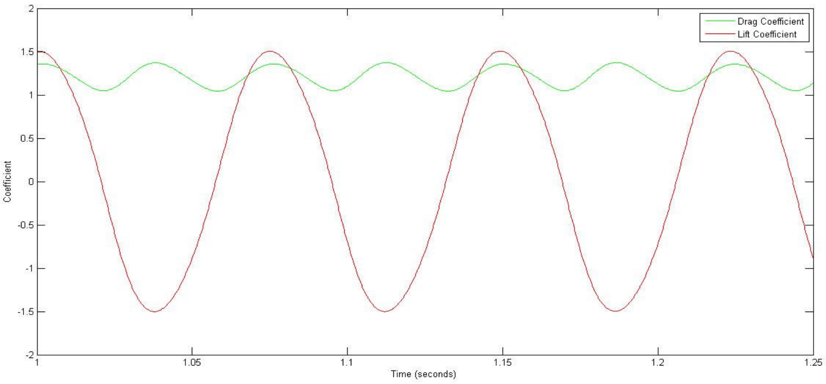

**Figure E-7 – Comparison between the drag and lift coefficients (Re=9·10$^4$)**

## E.4 Results

### E.4.1 Velocity contours

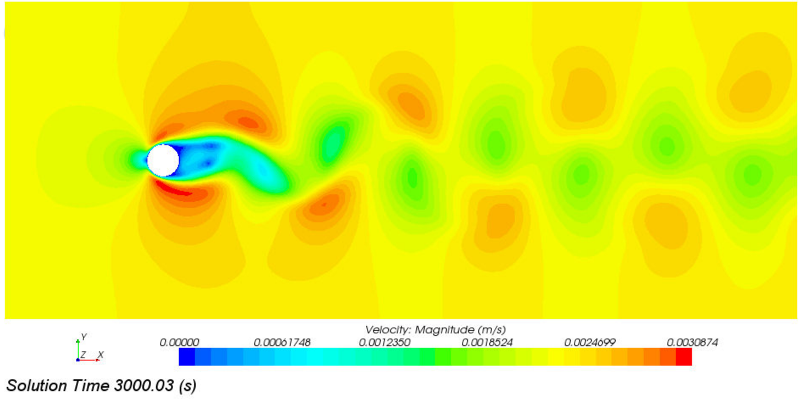

a) Re=100

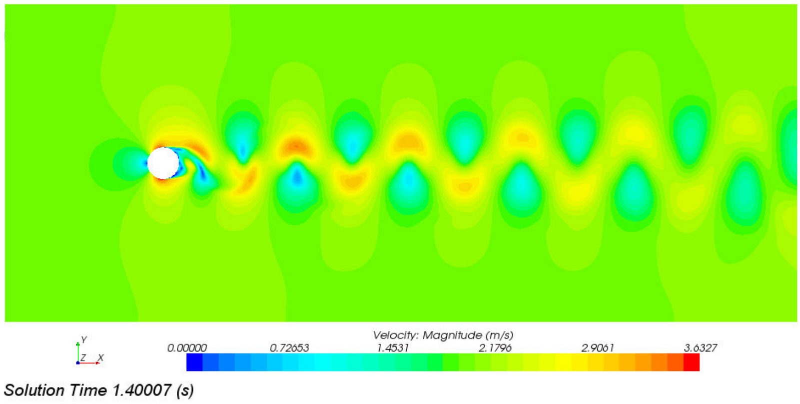

b) Re=$9 \cdot 10^4$

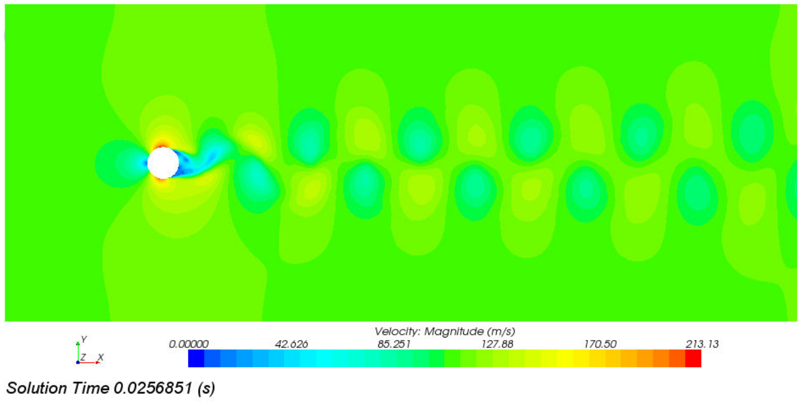

c) Re=$5 \cdot 10^6$

**Figure E-8 – Velocity contours of the flow around a 2D circular cylinder**

## E.4.2 Pressure coefficient

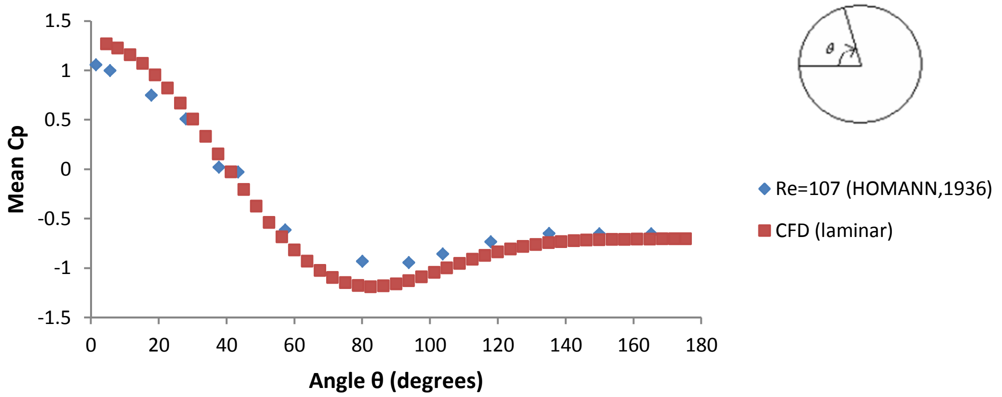

a) Re=100

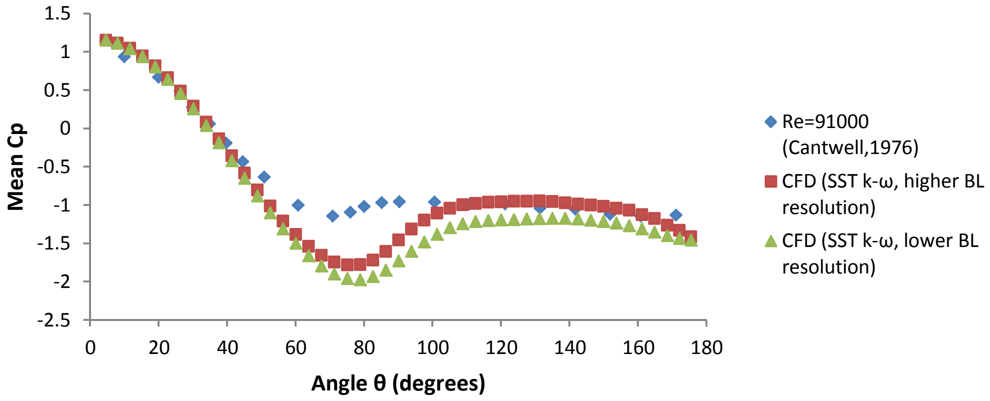

b) Re=9·10$^4$

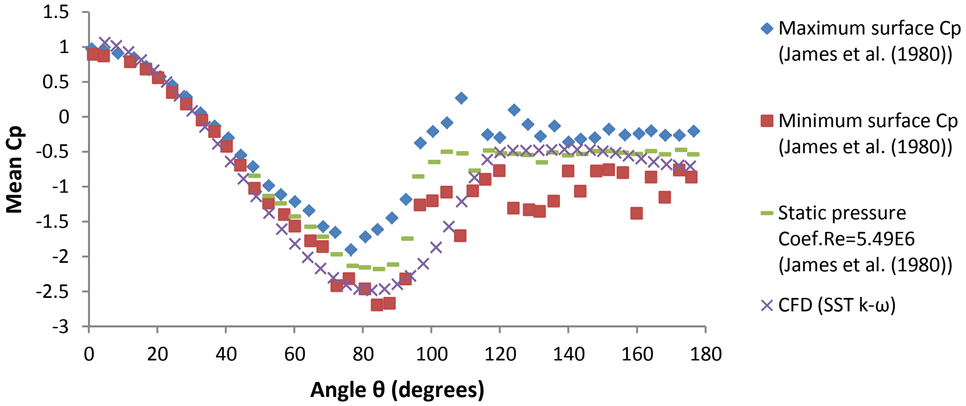

c) Re=5·10$^6$

**Figure E-9 – Pressure coefficient on the upper surface of the 2D cylinder**

# Appendix F PLAT-O

## F.1 Geometry

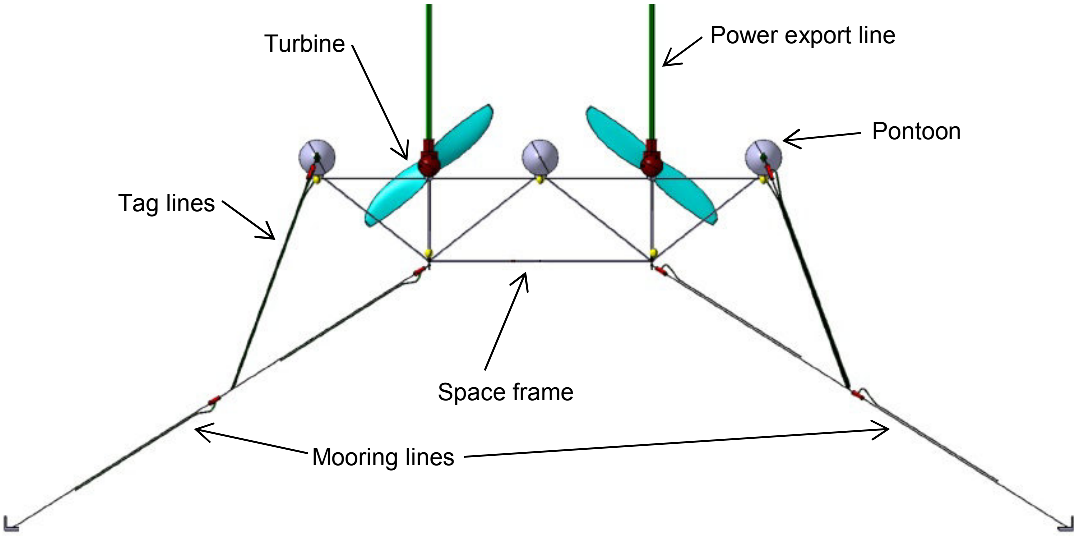

a) Front view

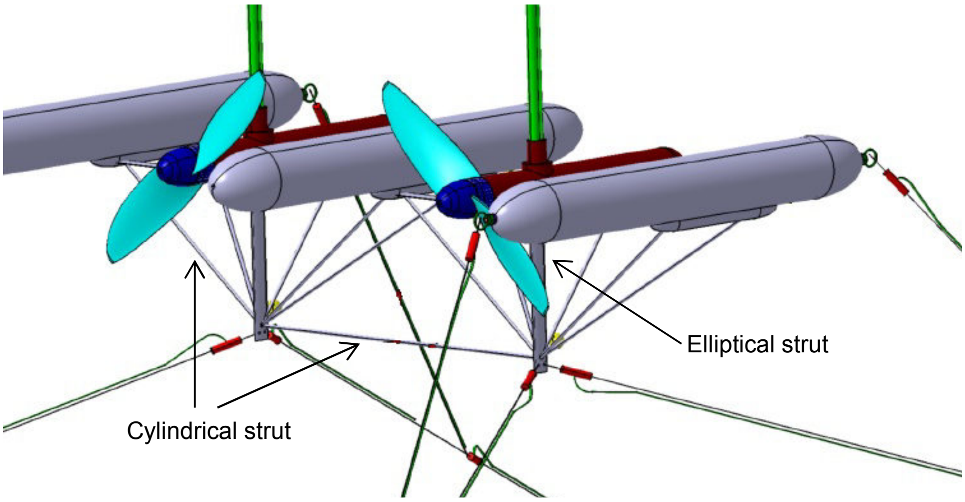

b) Detailed view

**Figure F-1 – 1:12 scale PLAT-O prototype**

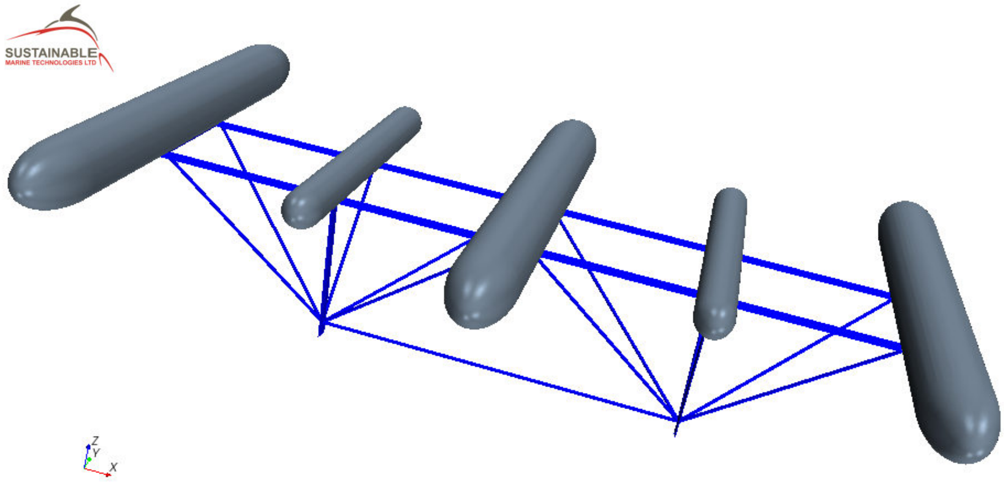

a) CAD model without power export lines

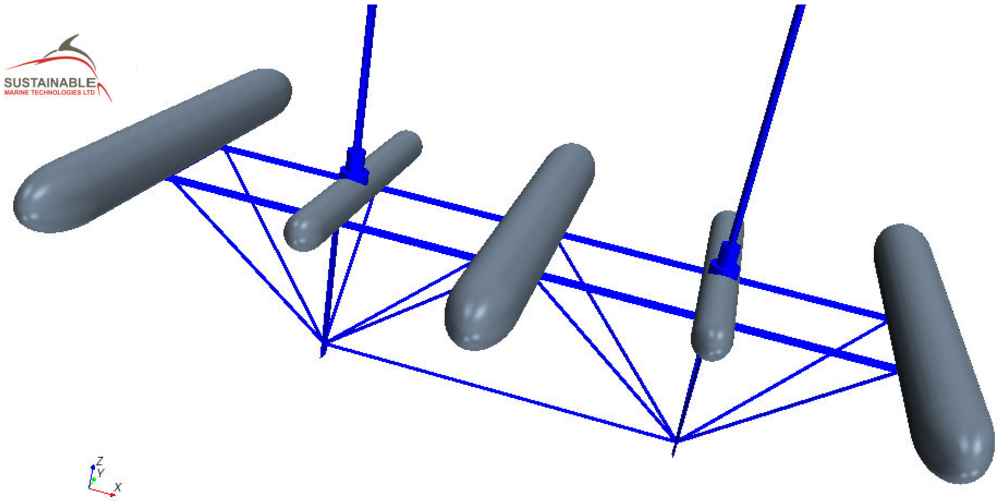

b) CAD model with power export lines

**Figure F-2 – Two different PLAT-O configurations analysed**

## F.2 Computational domain

a) Top view

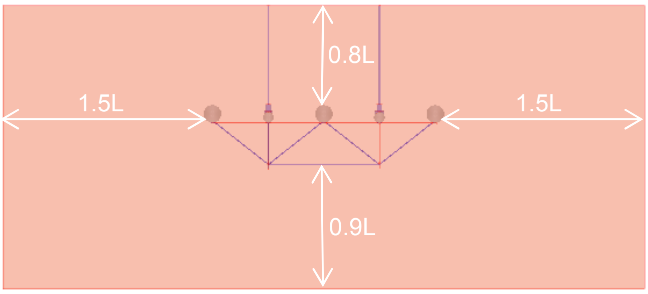

b) Front view

**Figure F-3 – PLAT-O computational domain**

## F.3 Mesh

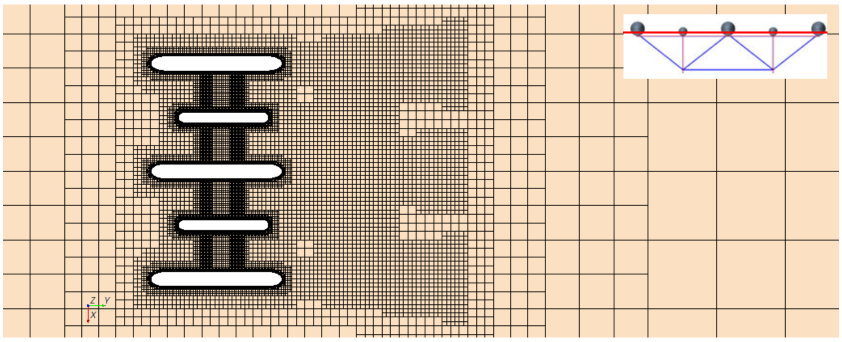

**Figure F-4 – Detail of the mesh**

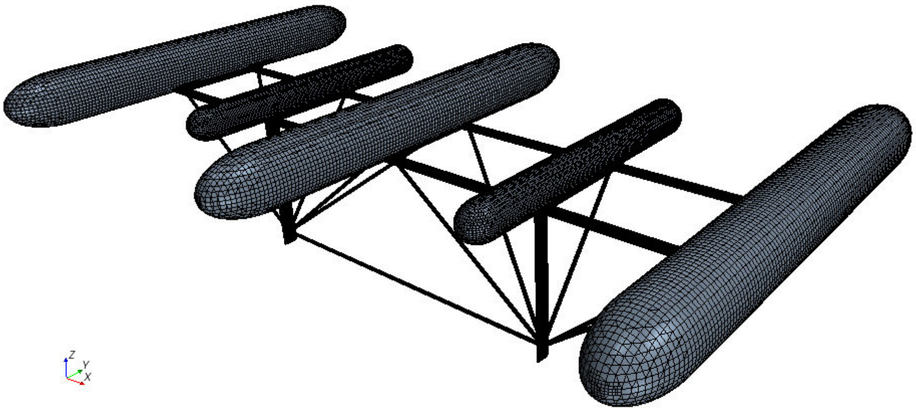

a) General view of PLAT-O surface mesh

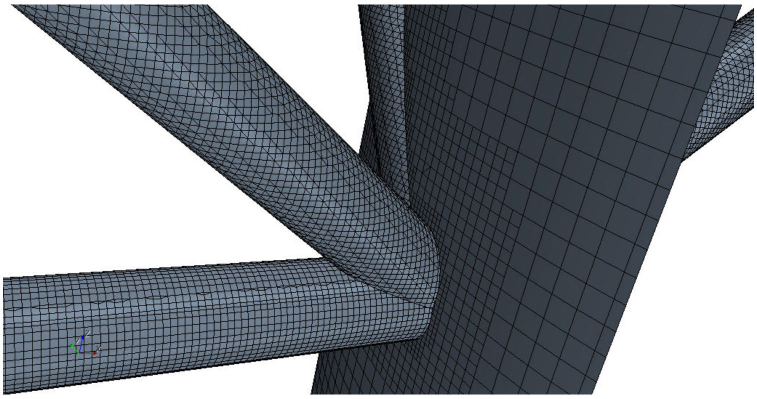

b) Detail of the mesh in the cylindrical/elliptical struts junction

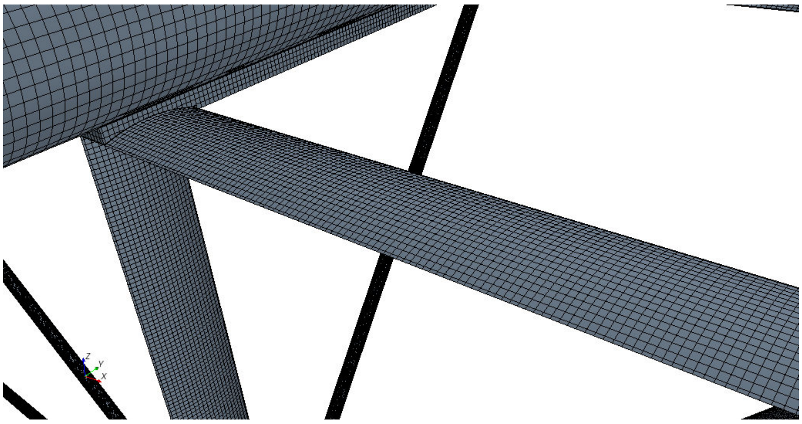

c) Detail of the mesh on the elliptical struts and pontoon/space frame connection

**Figure F-5 – PLAT-O surface mesh detailed views**

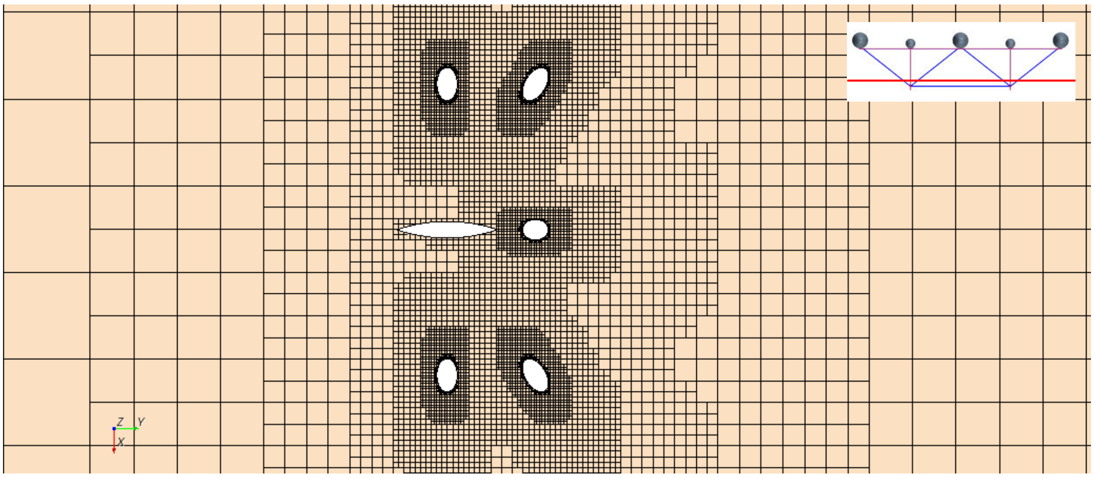

Figure F-6 – Detail of the mesh on the PLAT-O struts

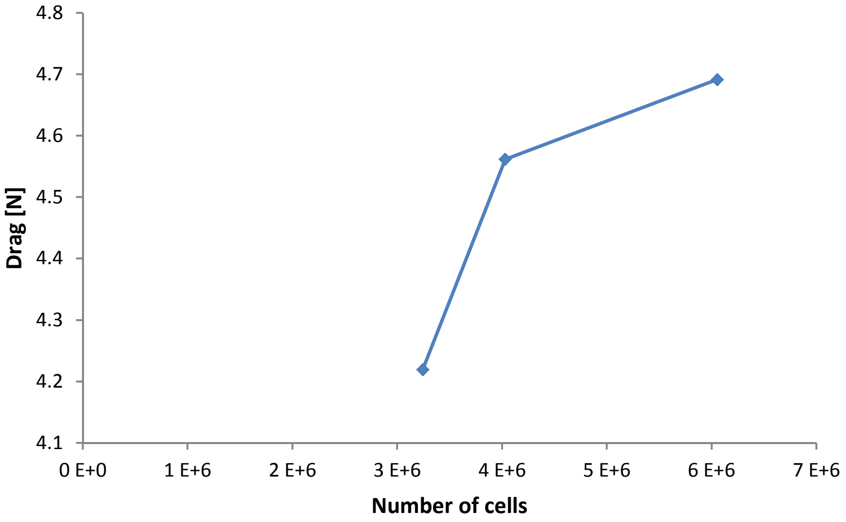

Figure F-7 – PLAT-O mesh independence study

## F.4 Residuals

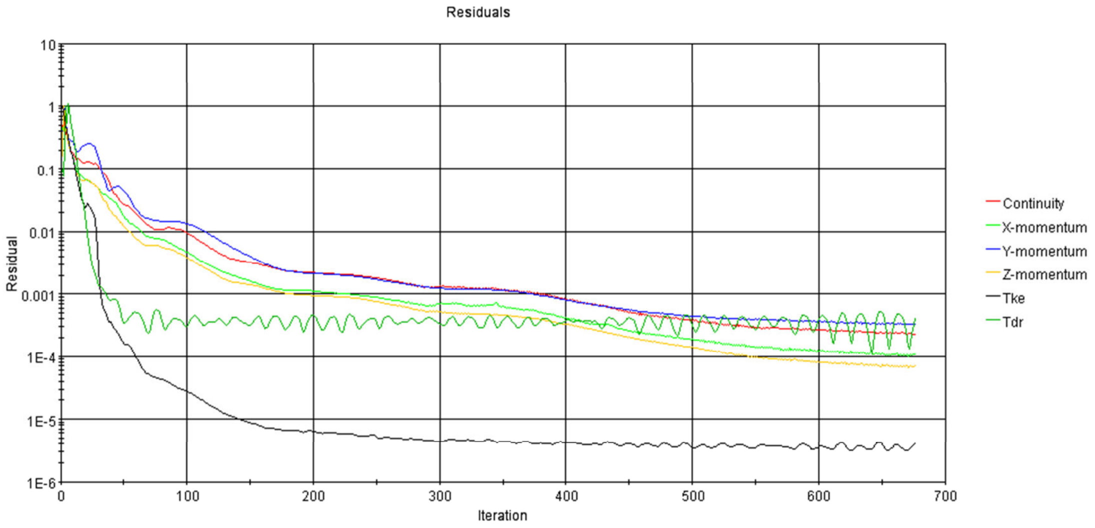

a) Residual history

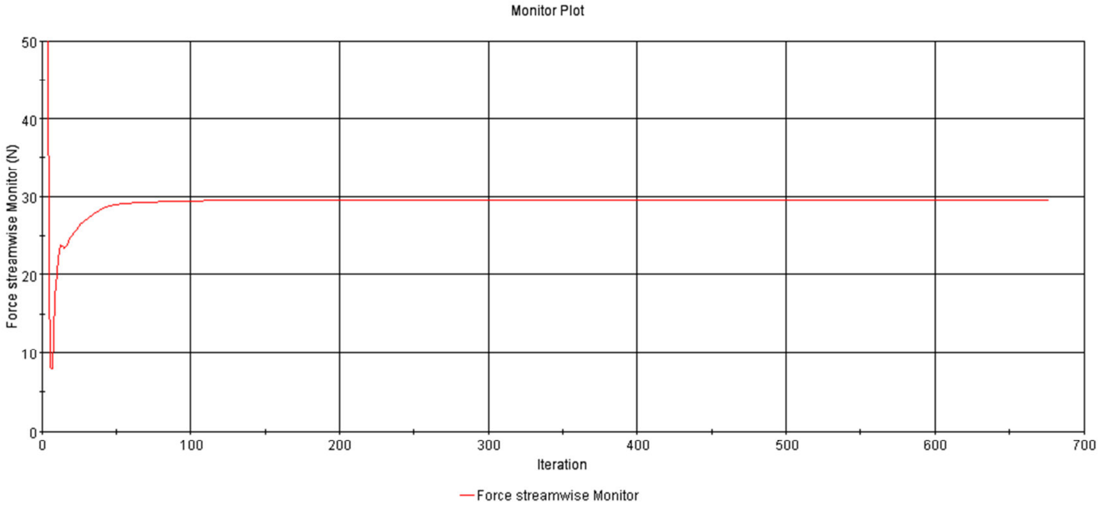

b) Drag coefficient versus number of iterations

**Figure F-8 – Monitored quantities to assess convergence**

## F.5 Velocity contours

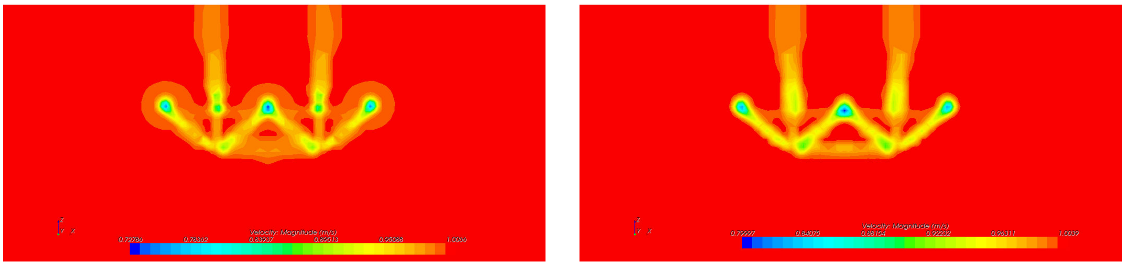

a) 0.8 meters

b) 1.5 meters

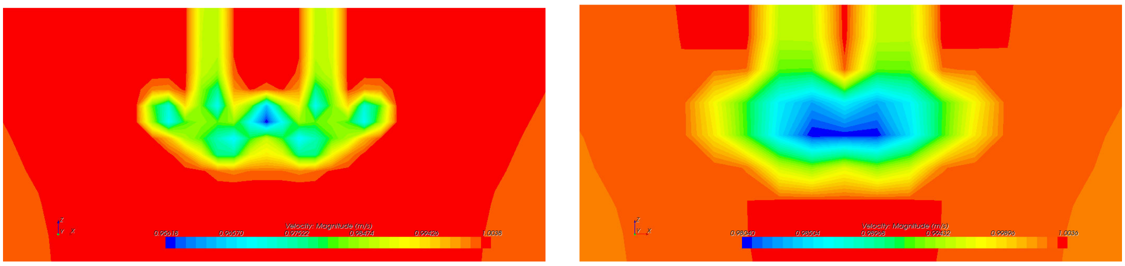

c) 2.2 meters

d) 2.9 meters

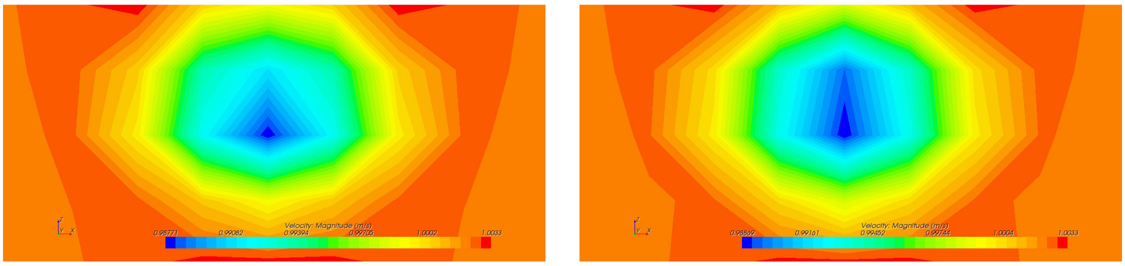

e) 3.6 meters

f) 4.3 meters

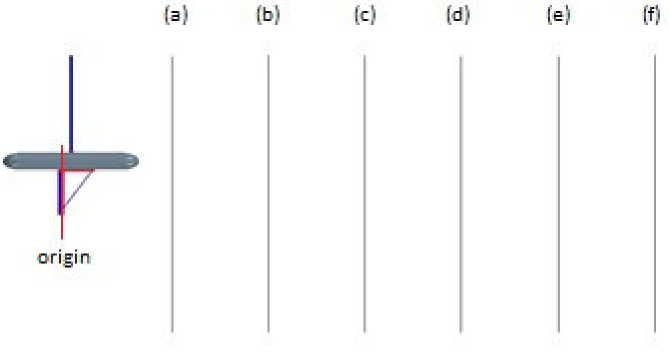

**Figure F-9 – Wake velocity contours *(U= 1m/s)***